Dissertation
submitted to the
Combined Faculties for the Natural Sciences and for Mathematics
of the Ruperto-Carola University of Heidelberg, Germany
for the degree of
Doctor of Natural Sciences

presented by
Diplom-Physiker: Stephan Kellner
born in: Bogen
oral examination: 14.12.2005

Novel Adaptive Optics Concepts: Wavefront Sensing with Sodium Laser Guide Stars at Extremely Large Telescopes and Simultaneous Differential Imaging

Referees: **Prof. Dr. Reinhardt Mundt**
Prof. Dr. Immo Appenzeller

Abstract

Since more than 15 years, Adaptive Optics (AO) is a proven concept to reach diffraction limited imaging at modern astronomical telescopes. In the case of next generation telescopes (Extremely Large Telescopes (ELTs)) with aperture diameters of up to 100m, sodium laser guide star based multi-conjugated-AO systems will be a basic requirement to exploit their full capability in terms of resolution and light concentration. A drawback of such an approach emerges in the finite distance and vertical extent of the sodium beacon in the mesosphere with respect to the telescope. This induces effects such as perspective elongation, where conventional wavefront sensing mechanisms will fail. Although several engineering concepts are under development to counteract these constraints at the cost of overall light efficiency and increased system complexity, this thesis proposes a novel kind of wavefront sensing technique to overcome the imposed limitations in a more natural way. The sensing technique is composed of two independently working sensors, a reflective rod and a mask with circular slits, each a representative of a novel wavefront sensor class, the so called z-invariant and Inverse Bessel Beam technique. Both are discussed in this thesis with a focus on the Inverse Bessel Beam technique. The latter is compared to alternative concepts such as temporal gating, with respect to the photon efficiency. Furthermore, the reflective rod was tested for its feasibility in laboratory conditions and in a more realistic environment at the William Herschel Telescope (WHT) at La Palma. With this test run its sensing principle has been verified. A novel technique already intensively used at 8m class telescopes is Simultaneous Differential Imaging. The direct detection of giant extra-solar planets is and will be a major science driver for galactic astronomy in the coming years. Modern telescope facilities such as the VLT reach, by means of adaptive optics, potentially the capability in terms of resolution and contrast required to detect planetary companions orbiting their host star. The recently implemented Simultaneous Differential Imaging upgrade for the near-infrared camera system NAOS-CONICA (NACO), is optimized in tracing the methane absorption feature of giant extra-solar planets. In the framework of this thesis a pipeline was developed to reduce NACO-SDI data. It was calibrated against the most promising candidate (Epsilon Eridani) hosting planetary companions by evaluating the deepest high contrast image data ever taken of this source.

Zusammenfassung

Durch den Einsatz Adaptiver Optik (AO) besitzt die astronomische Gemeinschaft seit fast 15 Jahren ein Werkzeug um mit modernen Großteleskopen beugungsbegrenzte Abbildungsqualität zu erreichen. Im Hinblick auf geplante Riesenteleskope wie das "Overwhelming Large Telescope" (OWL) der Europäischen Südsternwarte (ESO), mit Spiegeldurchmessern von bis zu 120m, wird der Einsatz von AO-Systemen der nächsten Generation, wie Natrium-Laser-Leitstern gestützte multi-konjugierte Adaptive Optik, unabdingbar sein, um das Leistungsvermögen (Auflösung und Lichtsammelvermögen) solcher Teleskope voll auszuschöpfen.
Künstliche Natrium-Laser-Leitsterne führen aufgrund ihrer endlichen Entfernung und nicht vernachlässigbaren Ausdehnung in der Atmosphäre unter anderem zu perspektivischen Effekten, die die Messgenauigkeit herkömmlicher Wellenfrontsensoren stark beeinträchtigen. Um solchen Effekten entgegenzuwirken, werden im Moment verschiedene Konzepte diskutiert. Diese sind jedoch mit hohem technischen Aufwand und/oder stark begrenzter Photonenausbeute verknüpft. Deshalb wird im Rahmen dieser Arbeit ein neuartiger Wellenfrontsensor vorgestellt, der sich der vorgegebenen Geometrie künstlicher Laserleitsterne in einer natürlichen Art und Weise anpasst. Der Sensor besteht aus zwei voneinander unabhängig arbeitenden Komponenten; einem reflektierenden Glasstab sowie einer Maske mit konzentrischen Spalten. Beide repräsentieren neuartige Sensortypen basierend auf dem z-invariant- und dem invertierten Bessel-Strahlkonzept. Die Grundlagen und Funktionsweise beider Techniken werden (mit einem Schwerpunkt auf dem invertierten Bessel-Strahlkonzept) diskutiert und mit mehr technisch orientierten Konzepten wie dem "temporal gating" im Hinblick auf deren Lichtsammeleffizienz verglichen. Des weiteren wurde das Messkonzept des reflektierenden Stabes mit Hilfe eines Laboraufbaus, und in einer mehr realistischen Umgebung am William Herschel Teleskop (WHT) unter Einsatz eines Rayleigh-Laser-Leitsterns getestet und verifiziert. Ebenfalls eine neue Methode in der Adaptiven Optik, die an modernen 8m-Teleskopen bereits zum Einsatz kommt, ist das so genannte "Simultaneous Differential Imaging (SDI)" (Simultane Differenzielle Abbildung). SDI bietet die Möglichkeit zum direkten Nachweis extrasolarer Planeten, einem der neuesten Forschungsschwerpunkte in der galaktischen Astronomie. Mit Hilfe moderner AO-Systeme erreicht man an Grossteleskopen im Prinzip die notwendige Auflösung sowie ausreichend Kontrast, um extrasolare Riesenplaneten abzubilden. Das SDI-Modul, eine Erweiterung der AO-nahinfrarot-Kamera NACO am Very Large Telescope (VLT), ist optimiert extrasolare Gasriesen mehrerer Jupitermassen aufgrund deren Methanatmosphäre zu detektieren. Deshalb wurde im Rahmen dieser Arbeit für zukünftig geplante SDI-Projekte am Max-Planck-Institut für Astronomie ein Datenreduktionspaket entwickelt. Dieses wurde an Epsilon Eridani des im Augenblick vielversprechendsten Kandidaten für den direkten Nachweis eines Exoplaneten getestet und geeicht. Dazu wurde ein Datensatz von Epsilon Eridani aufgenommen und ausgewertet, der die bisher tiefsten jemals aufgenommenen Hochkonstrastaufnahmen dieser Quelle beinhaltet.

to my father
in loving memory

Contents

Chapter 1

Introduction

1.1 Observing at the Diffraction Limit

At any times human beings were fascinated by the attraction conveyed by all the twinkling stars covering the entire night sky. For men in the ancient times it must have been impressive to observe the movement of all celestial bodies, in particular as they seemed to follow a well defined scheme when rotating around a fixed center. People figured out very early that certain directions, positions and orbits on the sky were exceptional and realized in this way the importance of these basic astronomical parameters. For instance, it is documented that people already in the Neolithic period (dated 6000 b.c.) buried their dead according to the four main directions on the sky. But to understand their real scope and meaning time was not ready, since imagination of humans and moreover technical enhancements were not developed far enough. Hence Sun, Moon and stars were surrounded by mythology and religious activities served as major stimulation for mankind to observe and understand the origin of the structural behavior of all celestial phenomenons. This lead to the appearance of the megalith culture and for the first time special locations for astronomical purposes have been built such as the megalith circle in Stonehenge (dated back to 3000-2000 b.c.). Besides fulfilling its purpose as a ritual site it was also used to perform astronomical observations, as has been verified and documented by Alexander Thom in the 1950s (Thom et al. (1951)). It is confirmed that astronomers in the megalith era had detailed knowledge about solary eclipses, since tall stones indicated positions of the Sun on the horizon at midsummer and midwinter. Moreover several other megalith circles were aligned with bright stars. The existence of these circles cannot only be explained with a religious intention and it is realistic to assume that they served as a kind of clock and calender, tracing the periodic movement of stars, Sun and moon. This was of a major interest, because human beings started to settle down and establish agriculture, which requires a detailed knowledge about seasons in order to optimize the sowing and harvest.

After the stone age and continuing throughout the ancient world, astronomy as science was mainly pursued by the Babylonian and the Greek. By means of relatively primitive equipment they were able to measure at a high precision many astronomical parameters. To mention one example: The time difference between two moon phases (synodic month) could be retrieved by Babylonian astronomers with an accuracy of 0.0001d.

This era was also marked by first attempts to create models explaining the structure of the solar system and even the entire universe, primarily triggered by philosophical interests. Aristarchos of Samos and Seleukos of Seleukia suggested a helocentric-heliostatic picture, based on known observational facts about the Earth's rotation, the circular shape of the

Earth's orbit, statical properties of the Sun, stars and the knowledge about the existence of planets. In contrast, Claudius Ptolemaeus (160 b.c. - 100 b.c), in an attempt to improve the geocentric theory of Hipparchos, proposed the Earth as the center of the movement of all bodies and therefore the universe. This approach prevailed for many centuries even up to the late medieval times, where further astronomical achievements were hampered by severe constraints due to Christian indoctrination. It took at least up to the 15th century until novel astronomical breakthroughs have been achieved and the era of modern astronomy began. Stimulated by the work of Aristarchos of Samos, Nikolaus Kopernikus in 1509 discharged the ideas of Ptolemaeus and established again the heliocentric view of the planetary motion. 82 years later Johannes Kepler was able to predict the orbital movements of planets by deducing simple equations. A further milestone was the publication of the "Philosophiae naturalis principia mathematica", an essay by Sir Isaac Newton about a formalism to describe the interaction between bodies by the gravitational force, giving scientists for the first time a set of equations to predict the movement of planets in time.

But the work carried out by Newton as well as all modern astrophysical perceptions would not have been possible without the invention of the astronomical telescope in 1608 by Galileo Galilei. Without any doubt this optical auxiliary tool had and still has the biggest impact for astronomy as a science. Increased collection power and higher resolution power make it possible for human beings to detect and separate celestial objects invisible for the eye. These two parameters characterize in principle the quality of a telescope and are only associated to the diameter D of the entrance pupil of focussing optics. To compare the collection power of a modern telescope with the unaided eye, one has to consider the number of photons N_{ph} focussed by the primary mirror, which is proportional to the available collection area: $N_{ph} \propto D^2$. Therefore a 10m telescope is able to collect 4000000 times more light than the eye. Diffraction optics considerations give an estimate of the increase in resolution. Fourier optics states that any optical system does not focus incoming parallel light rays in a single point. Instead the light beam is distributed over a finite region in the focal plane resulting in the Point Spread Function (PSF), which depends unexceptionally on the shape of the entrance pupil of the optical system. In the case of an aberration-free ideal circular aperture, the PSF is determined by the Airy-disk. Its Full Width Half Maximum (FWHM) - giving a measure of the resolving power - is $\propto \frac{\lambda}{D}$, with λ being the wavelength of the light. Hence a bigger telescope will be able to focus an incoming parallel beam in a smaller region. In the case of a modern 10m class telescope the FWHM of the Airy-disk at visible wavelength reaches 10 milliarcseconds (mas), which corresponds to a displacement of 25cm at a distance of 5000km. Combining both formulas, one gets an estimate of the maximum achievable Signal to Noise ratio (S/N), which is a measure of the entire gain achieved by a telescope. Assuming that the Signal to Noise is proportional to the amount of concentrated flux (= N_{ph} the number of photons) over the PSF area, one can write:

$$\frac{S}{N} \propto \frac{flux}{imagearea} \propto \frac{D^2}{4} \cdot \frac{D^2}{\lambda^2} \propto D^4 \tag{1.1}$$

Equation 1.1 shows that doubling the telescope diameter would lead to a gain in S/N of a factor of 16 for diffraction limited observations. However, all the computations and assumptions above are only valid for ideal conditions in the case when the optical system focusses an aberration-free, flat incoming wavefront. Light originating from astronomical objects accumulates phase and amplitude distortions while travelling through the turbulent Earth atmosphere. The shape of the incoming wavefront is now dominated by the spatial and temporal structure of the atmospheric turbulence and evolves randomly according to theses parameters. Assuming a short term exposure with an integration time below the dynamical evolution time of the turbulence (in the adaptive optics framework this is denoted by the

coherence time τ_0, which is in the order of milliseconds for optical wavelength), the distorted wavefront passing an optical system will - according to its induced phase error over the telescope pupil - lead to a PSF, which is dominated by a characteristic speckle pattern. Hence, due to the random nature of such speckle pattern, the PSF of a long term exposure becomes blurred generating a seeing disk. Obviously the FWHM of such a disk does not depend any longer on the telescope diameter but exclusively on atmospheric parameters, therefore limiting the resolution of the telescope. Even for the best astronomical sites, the size of the seeing disk in the visible does not drop below 0.4 arcseconds. This has a dramatic impact on the achievable S/N-ratio, since in equation 1.1 D^2/λ^2 has to be replaced by a constant term. In such a case the S/N-ratio is a function of the 2nd power of the telescope diameter D.

To utilize the full capabilities of a telescope and reach its diffraction limit, nevertheless, several ideas have been proposed in the past years as for instance:

1. **Space Missions:** A strategy to obtain sharp images in the optical or near-infrared bands to avoid the negative influence of turbulence is to position telescopes outside the atmosphere. Additional benefits are due to the elimination of further effects like the huge number of background photons caused by atmospheric radiation (which becomes a dominating effect in the mid- and far infrared) and wavelength depend transmissivity (extinction) of the atmosphere. In addition to the Hubble Space Telescope, which is equipped with instruments from the ultraviolet (UV) to the near-infrared, currently several space observatories such as SPITZER (covering the mid- to far infrared) are orbiting the Earth. Although space telescopes imply several advantages, one also has to consider the drawbacks. These are mainly the tremendous mission costs. While the costs to build a 10m class ground based telescope like W.M Keck amount to 100 MEuro (plus an annual budget of 11 MEuro), Hubble Space Telescopes mission development and mission costs already exceeds 6 GEuro. Space telescope missions moreover are subject to higher risk, since they have to be launched via a rocket and possibly have to be maintained and upgraded in space. This incorporates huge technical efforts and might require manned space missions, which are quite risky.

2. **Speckle Imaging:** Speckle imaging is a way to recover high resolution maps beyond the natural seeing limit (Labeyrie et al. (1970), Weigelt et al. (1991)). Images are taken at very short integration time well below the atmospheric coherence time τ_0. By correlating the speckle pattern of an unresolved calibrator and the science target over a sequence of frames, one can extract the hidden diffraction limited information. The short exposure time of the data results in a limited S/N. Hence this technique was mainly applied to the study of bright binary stars (Patience et al. (1998)) or other astronomical sources with simple geometries (Weigelt et al. (1998) or Leinert et al. (1993))

3. **Lucky Imaging:** Another approach to obtain results close to the diffraction limit is lucky imaging. As in the case of speckle interferometry, a series of short term exposures with integration times well below the atmospherical coherence time τ_0 are obtained. Due to the statistical behavior of wavefront phase errors, just by chance, a small amount of frames provide a wavefront almost free from high order aberrations. Since tip-tilt of a wavefront does not degrade the shape of the PSF, but simply translates into a shift in the focal plane, this can be corrected by using optimized shift and add algorithms. By analyzing the obtained Strehl-ratio of a reference star (see section 1.4.2) located within the images, one is able to select frames of sufficient quality. They are co-added thus providing diffraction limited imaging within the isoplanatic patch (see section 1.6). Beside the limited Field of View (FoV), obviously this concept is only suitable for small

to moderate sized telescopes and suffers also from an inefficient use of the light (Tubbs (2003))

4. **Adaptive Optics:** Adaptive Optics (AO) is until now the most promising idea to reach diffraction limited performance of ground based telescopes. An adaptive optics system is able to measure, reconstruct and correct in real time the atmospherically induced phase distortion of the incoming wavefront and provide continuously an almost flat wavefront for the science camera.

1.2 Adaptive Optics Systems

1.2.1 Principal Layout of an AO-system

Figure 1.1 depicts the working principle of a conventional AO system. In principle, it is composed of an analyzer, which samples the incoming wavefront for its aberrations, and a deformable mirror (DM) to apply the necessary corrections. To minimize the requirements on the dynamical range of the actuators of the DM, commonly a tip-tilt mirror is inserted into the optical path immediately before the DM, thus performing an a priori tip-tilt correction of the wavefront. By "closing the loop" the information of the Wavefront Sensor (WFS), which is processed in real time by the Wavefront Computer (WFC), is then relayed to all correction elements providing a feedback loop. The mirrors have to be inversely shaped with respect to the incoming wavefront to keep the wavefront flat. The shape of the DM is calculated by optimized control algorithms (van Dam et al. (2004), Dessenne et al. (1998), Egner (2003)). A beam-splitter or dichroic mirror divides the incoming beam of a science target in order to feed the WFS and Science camera with light simultaneously. It is advantageous to place the WFS behind the correction element to insure that only the differential wavefront error of the incoming wavefront and applied mirror shape has to be corrected between two measurement cycles. Typical loop frequencies range from several Hz (low order AO systems correcting in the K-band) up to kHz (high order extreme AO systems correcting in the V-band) and depend mainly on the corrected wavelength band.

1.2.2 AO - A Historical Overview

The first idea of a real time compensation of atmospherically induced phase perturbations occurred in the 1950s and has been published by Horace Babcock (Babcock et al. (1953)). He proposed to use a rotating knife edge serving as wavefront sensor, sampling in this way the incoming wavefront for distortions. The sensor pipelines signals directly to change the optical thickness of an electronically deformed oil film on an Eidophor mirror. This first draft of an AO-system already included all necessary components, but a practical realization failed due to the limited computational power available at this time. Mainly the latter was the reason that it took more than 20 years to realize and build such a system. The first running AO-system able to sharpen images was designed for military purposes at Star Fire Optical Range (SOR) in the late 1970s to image military satellites. Another 10 years passed until this technique was applied for astronomical purposes. Unlike in the case of imaging satellites, which are close and have an intrinsic brightness of (in the worst case) 9th magnitude, astronomical reference sources are much fainter. This restricts the number of available photons per sub-aperture and sets high requirements on the sensitivity of the WFS detector. Suitable detectors like CCDs, which also provide a fast enough readout, were commercially available in the 1980s. In 1989, the European Southern Observatory (ESO) built, in cooperation with the Observatoire de Paris-Meudon, ONERA and Laserdot, with

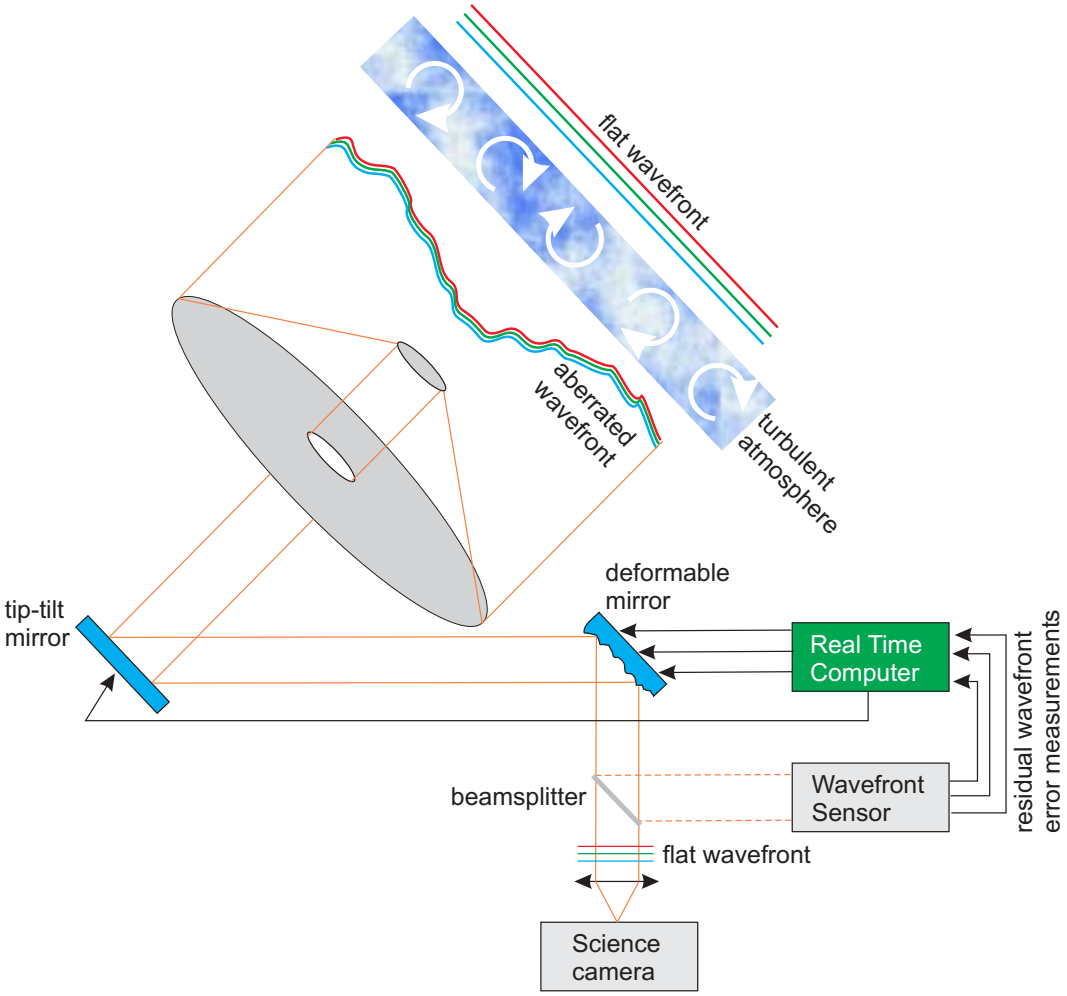

Figure 1.1: Principle layout of an adaptive optics system: Accumulated phase errors of the incoming wavefront are measured by a wavefront sensor unit and processed in real time. The real-time computer triggers the correction units (tip-tilt and deformable mirror) to be inversely shaped to the measured distortions providing a flat wavefront for the science instrument.

"COME-ON" the first astronomical AO system at the 1.52m telescope of the Observatoire de Haute Provence (Rousset et al. (1990)). It consisted of a 5x5 Shack-Hartmann-Sensor (SHS) and a 19 actuator continuous facesheet deformable mirror. The system operates at a sampling rate of 100Hz achieving a correction bandwidth of 10Hz for imaging between 2.5micron and 5micron. COME-ON was designed to explore the application of AO for the VLT and has been installed 1991 at the 3.6m telescope in La Silla (Rigaut et al. (1991)). By correcting at shorter wavelengths (1.2 - 5 micron) and using not a zonal but a modal Zernike correction for the wavefront reconstruction (Hardy (1998)), a big step towards modern AO-systems was done. In 1992 "COME-ON" was upgraded with a 52 actuator flexible silicon DM able to run at a higher correction bandwidth, and was operated at the 3.6m as "COME-ON-PLUS". After two years of further development (a new 64 actuator DM plus a separate tip-tilt correction unit), this system was renamed into "ADONIS" the first AO user instrument available to the astronomical community. Within the past 10 to 15 years Adaptive Optics have been a very fast growing field where new innovative ideas and also technical enhancements pushed and will further push the performance of adaptive optics system technology. Today most

8 . . . 10m class telescopes are equipped with AO-modules to support all kinds of instruments.

1.3 Atmosphere and Turbulence

To develop and build an optimized AO-instrument, one has to understand the properties and nature of the turbulent atmosphere in order to describe properly the expected phase distortions of an incoming wavefront. Turbulence originates from differential heating of the Earth's surface. Convection processes lead to hydrodynamical instabilities in the atmosphere constituted mainly of inhomogeneities in temperature T, pressure P and humidity. Since the index of refraction of air depends on these quantities and the observing wavelength one can write (von der Luehe (2001)):

$$n(P,T,\lambda) = 1 + 7.76 \cdot 10^{-5}(1 + 7.52 \cdot 10^{-3}\frac{1}{\lambda^2}) \cdot \frac{P}{T} \tag{1.2}$$

Permanent fluctuations of these physical quantities on timescales from milliseconds to years cause that the Earth's atmosphere is not in equilibrium but in continuous motion to overcome those differences. By treating the air as a viscous fluid one can determine whether the flow is laminar or turbulent. The Reynolds number - characterized by the ratio of inertial to viscous forces - is a criteria to determine the property of air:

$$Re = \frac{L_0 v_0}{\kappa_\nu} \tag{1.3}$$

Where v_0 is the average velocity of a viscous fluid of a characteristic size L_0, κ_ν describes the kinematic viscosity. When the dimensionless Reynolds number exceeds 10^3, the flow is expected to change from a laminar into a turbulent behavior. In the case of the atmosphere the Reynolds number is of the order of 10^6, implying therefore a turbulent characteristic. Kolmogorov introduced a simple analytical model to describe the statistics of atmospheric

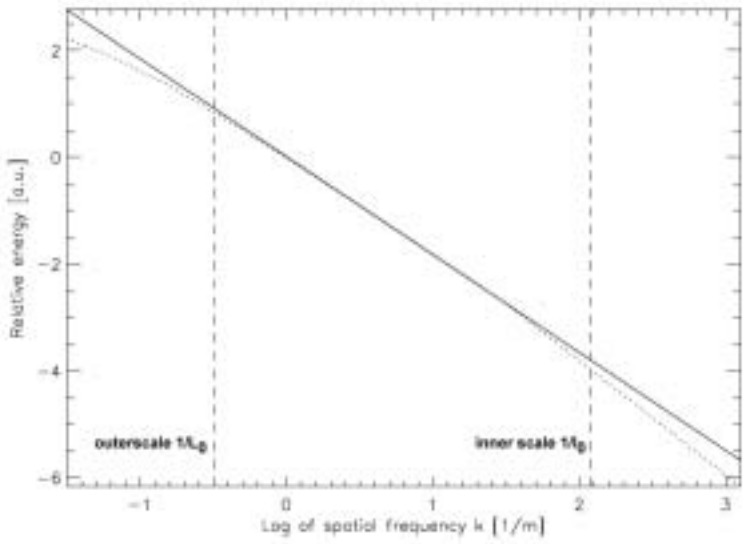

Figure 1.2: Kolmogorov (solid) and von Karman (dotted) turbulence energy spectra. The vertical dashed lines indicate the limits of inner and outer scale. In this plot the Kolmogorov spectrum is extrapolated outside the inner and outer scale.

turbulence (see for instance Pope (2000)). He stated that energy fed into the system at big

spatial scales is transported loss-less to smaller structures until the Reynolds number of the flow drops down to the laminar regime resulting in viscous heat dissipation. The size of large-scale fluctuations, referred to as large eddies, can be characterized by their outer scale length L_0. Typical values for the outer scale vary from several meters on the ground to up to several tens of meters in the free atmosphere. For instance, in the case of Cerro Paranal, measurements gave an outer scale value of 24m (Conan et al. (2000)). The typical size of the inner scale-eddies l_0 is of the order of mm near the ground and several centimeters in the free atmosphere. Kolomogorov's assumption showed that the energy distribution follows a power law in the spatial frequency space according to:

$$E(\kappa) = |\kappa|^{-11/3} \tag{1.4}$$

where κ denotes the spatial frequency. Since Kolmogorov's law is only valid within the borders of inner and outer scale, this leads to a quite unnatural sharp cut off at L_0 and l_0. To solve this problem several attempts have been made to expand the Kolmogorov spectrum to a more general basis, which resulted in the widely used von-Karman spectrum (see Figure 1.2). This is given by:

$$E(\kappa) = (|\kappa|^2 + \kappa_0^2)^{-11/6} \exp\left(-\frac{|\kappa|^2}{\kappa_i^2}\right) \tag{1.5}$$

Here the constants $\kappa_0 = \frac{2\pi}{L_0}$ and $\kappa_i = \frac{5.92}{l_0}$ define the inner and outer scale cut-off regions. Based on equation 1.4 and 1.5 one can deduce the impact on the index of refraction, which determines the temporal and spatial structure of an incoming wavefront in a statistical sense. The refractive index is a passive quantity and has no influence on the turbulence itself. It can be shown that it follows the same spatial frequency law as the energy distribution (Obukhov (1949)). Assuming Kolmogorov's law, the power spectrum of the refractive index fluctuations $\Phi_n(\kappa)$ can be written as

$$\Phi_n(\kappa) = 0.0033 C_n^2(z) |\kappa|^{-11/3} \tag{1.6}$$

where $C_n^2(z)$ is the refractive index structure constant describing the strength of the turbulence at altitude z. In the case of the von-Karman spectrum the refractive index fluctuation is determined by:

$$\Phi_n(\kappa) = 0.0033 C_n^2(z)(|\kappa|^2 + \kappa_0^2)^{-11/6} \exp\left(-\frac{|\kappa|^2}{\kappa_i^2}\right) \tag{1.7}$$

When one is interested primarily in the phase of a wavefront that has propagated through turbulence (the usual situation in adaptive optics), then the outer scale L_0 is usually of much greater significance than the inner scale l_0, in particular with respect to issues such as wavefront tilt.

1.3.1 Impact of Atmospherical Turbulence on Spatial Wavefront Phase Errors

An incoming wavefront, while travelling through the atmosphere, experiences the integrated fluctuations of the index of refraction. Therefore, the phase of the wavefront also varies randomly at the telescope pupil, according to the statistics defined above. Structure functions, as second statistical moment, provide a convenient way to describe the phase statistics of an incident wavefront (which normally fluctuates around 0). They are defined as

$$D_\Phi(\mathbf{r}) = \langle |\ \Phi(\mathbf{r}) - \Phi(\mathbf{r}+\mathbf{r'})\ |^2 \rangle \tag{1.8}$$

describing for a wavefront $\Phi(\mathbf{r})$ its averaged phase variance in a distance $\mathbf{r}$ with respect to a defined reference point $\mathbf{r'}$. The structure function of the phase fluctuations of an incoming

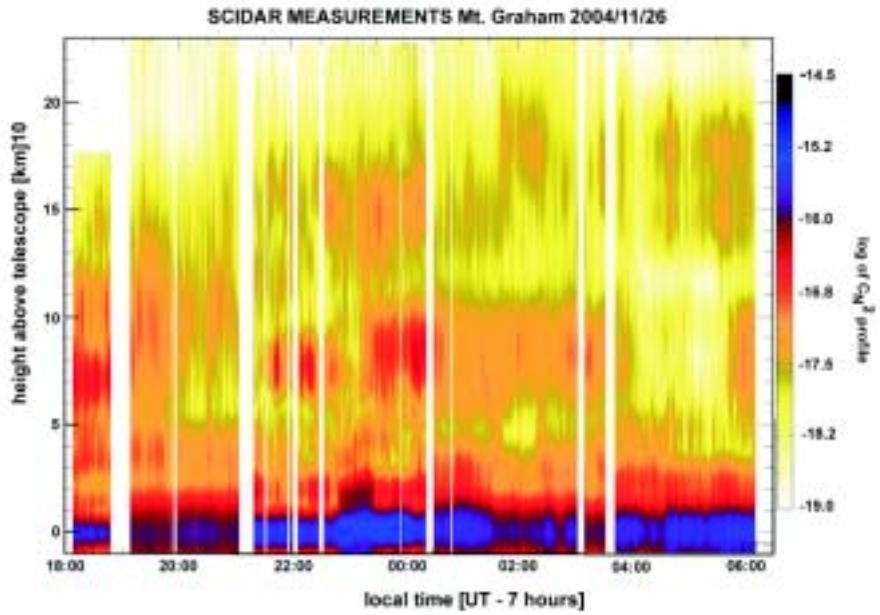

Figure 1.3: Results of SCIDAR measurements done in November 2004 to determine C_N^2-profiles at Mt. Graham. The data verify that the most turbulent part of the atmosphere is located close to the ground. This plot is kindly provided by Sebastian Egner.

wavefront obeying Kolmogorov statistics has been calculated by Fried (1965) and can be expressed as

$$D_\Phi(r) = 2.914k^2 \sec(\gamma) r^{5/3} \int_0^\infty C_n^2(z)dz = 6.88(\frac{r}{r_0})^{5/3} \tag{1.9}$$

where $r_0 = \left[0.423k^2 \sec(\gamma) \int_0^\infty C_n^2(z)dz\right]^{-3/5}$ defines the Fried parameter and γ the zenith distance. Equation 1.9 gives a measure of the average phase error between two parallel rays of wave number $k = 2\pi/\lambda$, located at a distance r when travelling through the turbulent atmosphere with a structure constant profile of $C_n^2(z)$. The Fried parameter is a physical quantity summarizing all statistical properties of the phase fluctuation of a wavefront. It defines the aperture diameter over which an incoming wavefront has a root mean square (RMS) phase error of one radian. As a result the resolution of a telescope is not limited by diffraction effects but by atmospheric turbulence. Hence r_0 gives ultimately the achievable resolution by defining the FWHM of the seeing disk via: $\frac{\lambda}{r_0}$. Obviously r_0 is proportional to the integral over the C_n^2-profile viewed at the zenith angle γ and proportional to the 6/5 power of the wavelength. In the visible, r_0 usually ranges from 5cm to 15cm. Table 1.1 shows typical values for r_0 at different wavelength and reveals why AO is preferably done at longer wavelengths, where a larger coherence length is achieved.

wavelength λ	0.5μm	1μm	1.6μm	2.2μm
r_0	10cm	24cm	42cm	60cm

Table 1.1: Typical values for r_0 at different wavelength. For each wavelength a seeing of 1" at 500nm is assumed.

Finally in order to calculate the power spectrum $\Phi(k)$ of the phase fluctuations of the wavefront at the telescope pupil, one may exploit its relation to the structure function $D_\Phi(r)$,

which is determined by the Fourier Transform. Hence, assuming isotropy, $\Phi(k)$ is given by:

$$D_\Phi(r) = 2 \int dk\ \Phi(k)[1 - cos(2\pi kr)] \tag{1.10}$$

Noll (1976) calculated the spatial energy spectrum of the phase fluctuations due to Kolmogorov turbulence:

$$\Phi(k) = (0.0023 r_0^{-5/3}) k^{-11/3} \tag{1.11}$$

1.3.2 Impact of Atmospherical Turbulence on Temporal Wavefront Phase Errors

In the previous section only the spatial characteristics of phase fluctuations obeying Kolmogorow statistics were discussed. It is also of major interest to understand their temporal behavior and thus the impact of the temporal frequency bandwidth on an optimized sensing and correction. To disentangle the complexity when studying a dynamical model of the turbulent atmosphere, in general two simplifications are made:

- The atmosphere is divided into well defined layers at different altitudes. Each layer can be treated as a single phase screen.
- The *Taylor hypothesis* (see section 4.7.1) is used, which states that each layer is moving at wind speed $\mathbf{V}$ while its overall shape remains unchanged ("frozen flow" approximation). The Taylor hypothesis in mathematical form can be written as:

$$\Phi(\mathbf{r}, t + \tau) = \Phi(\mathbf{r} - \tau \cdot \mathbf{V}, t) \tag{1.12}$$

In analogy to the spatial Power Spectral Density (PSD) given in equation 1.11 Conan determined the temporal PSD $\Phi(\nu)$ of the phase fluctuations using the above simplifications (Conan et al. (1995)):

$$\Phi(\nu) \propto C_n^2(z) dz \frac{1}{V} \left(\frac{\nu}{V}\right)^{-8/3} \tag{1.13}$$

Here ν defines the temporal frequency. Note that the temporal PSD is, unlike its spatial counterpart, characterized by a $-8/3$ power law. In this context Conan investigated the resulting temporal spectral behavior of a Zernike modal basis (see Figure 1.4). For low frequencies the power spectral density for each mode is constant and drops down at a certain cut-off frequency

$$\nu_c \sim 0.3(n + 1)V/D \tag{1.14}$$

by following a $\nu^{-17/3}$ power law. Equation 1.14 shows that the cut-off frequency is a function of the radial mode number n and increases for higher radial orders. In practice, it is only possible to correct wavefront distortions within a finite bandwidth. For this reason Greenwood (1977) calculated the residual error of a system correcting at a finite bandwidth assuming perfect spatial correction. He defined the *Greenwood frequency* ν_G as the bandwidth leading to a residual RMS wavefront error of 1 rad^2:

$$\nu_G = \left[0.102 k^2 (\cos\gamma)^{-1} \int_0^\infty C_n^2(z) V(z)^{5/3}\right]^{-3/5} \tag{1.15}$$

ν_G is determined by the turbulence and wind profiles of the atmosphere. The Greenwood frequency is the reciprocal of the coherence time τ_0 - the temporal analogon of Fried's parameter - defined by $1/\nu_G$. Assuming only a single turbulent layer one can write:

$$\tau_0 = \frac{r_0}{V} \tag{1.16}$$

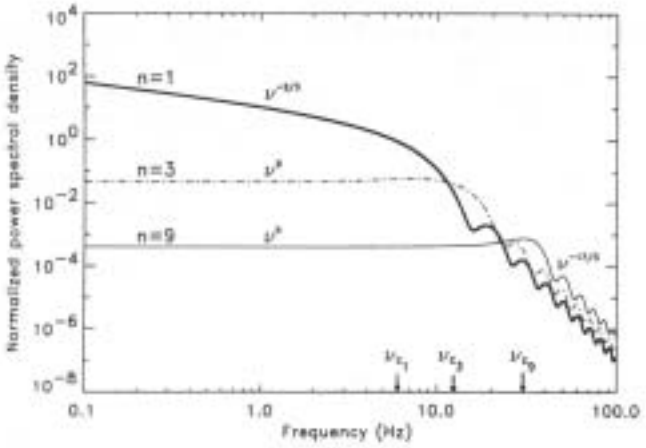

Figure 1.4: Zernike polynomial temporal power spectral density distribution of phase fluctuations for 3 different radial degrees (n= 1,3,9). The asymptotic power laws and cut-off frequencies are indicated. This plot has been taken from Conan et al. (1995).

Equation 1.16 connects the coherence time τ_0 and the Fried parameter r_0 via the wind speed V of each turbulent layer. τ_0 is indirectly proportional to the wavelength, which implies a correction requiring a smaller temporal bandwidth for longer wavelengths. For instance, in the V-band assuming a seeing of 1" the typical ν_G is 60Hz, while in the K-Band ν_G is 7Hz.

1.3.3 Modal Decomposition and Zernike Expansion of Kolmogorov Turbulence

Wavefront phase errors within the pupil can be quantified by means of two different approaches. One can describe the wavefront in a zonal approach where a grid of a specific sampling size is laid over the pupil. By determining the average amplitude of the phase aberration at each sub-aperture, the entire wavefront can be decomposed. Although this sounds straightforward, it leads to major drawbacks in the practical implementation of an AO-system, since the number of actuators of the DM has to match the number of sub-apertures of the WFS. This makes a setup less flexible for possible upgrades.

Another possibility to reconstruct the wavefront phase errors is by modal decomposition of the wavefront. In this case the wavefront is divided into a series of infinite orthogonal 2-d basis functions normalized either over a unit circle or an annular aperture with inner radius r_i according to:

$$\Phi(\mathbf{r},t) = \sum_{i=1}^{\infty} a_i(t) F_i(\mathbf{r}) \tag{1.17}$$

Here $\mathbf{r}$ is a vector in the pupil plane and $a_i(t)$ the amplitude of each basis function $F_i(\mathbf{r})$, which fulfills the orthonormality relation:

$$\int_{aperture} d^2\mathbf{r}\, W(\mathbf{r}) F_i(\mathbf{r}) F_j(\mathbf{r}) = \delta_{ij} \tag{1.18}$$

While δ_{ij} denotes the Kronecker delta symbol, $W(\mathbf{r})$ is a pupil weighting function and in the case of an annular aperture defined as:

$$W(\mathbf{r}) = \begin{cases} \frac{1}{\pi(1-r_i^2)} & (|\mathbf{r}| \leq 1) \\ 0 & (|\mathbf{r}| > 1) \end{cases} \tag{1.19}$$

$$\begin{pmatrix}
0.448 & 0 & 0 & 0 & 0 & 0 & -0.0141 & 0 & 0 & 0 & 0 \\
0 & 0.448 & 0 & 0 & 0 & -0.0141 & 0 & 0 & 0 & 0 & 0 \\
0 & 0 & 0.0232 & 0 & 0 & 0 & 0 & 0 & 0 & -0.0039 & 0 \\
0 & 0 & 0 & 0.0232 & 0 & 0 & 0 & 0 & 0 & 0 & 0 \\
0 & 0 & 0 & 0 & 0.0232 & 0 & 0 & 0 & 0 & 0 & -0.0039 \\
0 & -0.0141 & 0 & 0 & 0 & 0.0062 & 0 & 0 & 0 & 0 & 0 \\
-0.0141 & 0 & 0 & 0 & 0 & 0 & 0.0062 & 0 & 0 & 0 & 0 \\
0 & 0 & 0 & 0 & 0 & 0 & 0 & 0.0062 & 0 & 0 & 0 \\
0 & 0 & 0 & 0 & 0 & 0 & 0 & 0 & 0.0062 & 0 & 0 \\
0 & 0 & -0.0039 & 0 & 0 & 0 & 0 & 0 & 0 & 0.0024 & 0 \\
0 & 0 & 0 & 0 & -0.0039 & 0 & 0 & 0 & 0 & 0 & 0.0024
\end{pmatrix}$$

Table 1.2: Covariance matrix of the first 11 Zernike modes after Wang and Markey (1978). The covariance matrix is a measure of the contribution of each mode to the total variance of the phase fluctuation over the pupil. All values here are normalized to $(D/r_0)^{5/3}$.

Using the orthogonality relation, the weighting coefficients $a_i(t)$ can be derived via:

$$a_i = \int d^2\mathbf{r}\; W(\mathbf{r})\Phi(\mathbf{r})F_i(\mathbf{r}) \tag{1.20}$$

A further interesting relation can be deduced by evaluating:

$$\begin{aligned}\int d^2\mathbf{r}\; W(\mathbf{r}) < \Phi(\mathbf{r})^2 > \;&=\; \sum_{i,j} < a_i a_j > \int d^2\mathbf{r} W(\mathbf{r})F_i(\mathbf{r})F_j(\mathbf{r}) \\ &= \sum_i < a_i^2 > . \end{aligned} \tag{1.21}$$

Equation 1.21 verifies that the total variance of the wavefront error over the pupil can be composed by summing the variance of the weighting coefficients of each base function. The values $< a_i a_j >$ are known as the elements of the *modal covariance matrix*. The diagonal elements of this matrix correspond to the individual contributions of the variance of each mode.

1.3.4 Zernike Polynomials and Karhunen-Loeve Functions

Two-dimensional Zernike Polynomials (introduced 1934 by Fritz Zernike; see appendix B) define a set of orthogonal basis functions $F_i(\mathbf{r})$ and are widely used for opto-mathematical purposes. The lowest order Zernike polynomials correspond to the well known optical phase aberrations de-focus, astigmatism and coma. Noll (1976) investigated the statistical properties of Zernike polynomials as a basis set to compose wavefronts, which obey Kolmogorov statistics. He determined the diagonal elements of the modal covariance matrix by calculating analytically the residual phase variance Δ_J of a wavefront after correcting J Zernike modes:

$$\Delta_J =< \Phi(\mathbf{r})^2 - \sum_{j=1}^{J} < |a_j|^2 > \tag{1.22}$$

Furthermore he showed that the piston term carries an infinite amount of energy, and that after its subtraction the residual variance over the unit circle is given by $\Delta_1 = 1.0299(D/r_0)^{5/3}$. In the case when J is large ($J > 10$) the residual variance can be approximated via the formula:

$$\Delta_J \approx 0.2944 J^{-\sqrt{3}/2}(D/r_0)^{5/3}[rad^2] \tag{1.23}$$

Wang and Markey (1978) performed minor corrections on Nolls computations leading to the covariance matrix listed in Table 1.2. The matrix contains some off-diagonal elements and implies thus some redundancy. In practice this means that Zernike polynomials are a good

but not an ideal basis set of functions for wavefront decomposition of phase errors over a unit circle. An ideal set is defined by Karhunen-Loeve (K-L) (Wang and Markey (1978)) functions. If only a limited number of modes is used, the K-L functions carry more information about the statistical behavior of the fluctuations than any other set of functions (which states in a pure diagonal covariance matrix) e.g. Zernike modes. K-L functions are not a fixed basis set of functions but depend on the underlying statistical process. K-L functions can be calculated by solving an eigenvalue integral equation:

$$\int d^2\mathbf{r'}W(\mathbf{r'})F_i^*(\mathbf{r'}) < \Phi(\mathbf{r'})\Phi(\mathbf{r}) >= \Lambda_i^2 F_i(\mathbf{r}) \tag{1.24}$$

1.3.5 Effects of Turbulence on Astronomical Imaging

The impact of wavefront phase fluctuations in astronomical imaging can be described by means of the Fourier Optics formalism. In this framework the complex amplitude of a wavefront in the pupil plane is related to its 2-d intensity distribution in the focal plane via its Fourier Transform:

$$I(\mathbf{r}) = |\mathbf{FT}(A(\mathbf{R})\Theta(\mathbf{R}))|^2 \tag{1.25}$$

$\mathbf{R}$ and $\mathbf{r}$ denote 2-d vectors in the pupil and focal plane, respectively. While $\Theta(\mathbf{R})$ gives the aperture function of the pupil, $A(\mathbf{R}) = A_0(\mathbf{R})\exp^{i\Phi(\mathbf{R})} = \exp^{\ln A_0 + i\Phi(\mathbf{R})}$ denotes the complex amplitude of the incoming wavefront. It can be shown that the power spectrum of wavefront perturbations is equal to $E_\Phi + E_{\ln A}$ with $E_{\ln A} \ll E_\Phi$, which means that amplitude fluctuations of an incoming wavefront can be neglected in the first order approximation (Roddier (1981), Masciadri et al. (2004), Angel (1994)). As already mentioned, in the case of an aberration free plane wave passing a circular aperture, the resulting PSF is given by the Airy-disk (Hecht (1998)). Its FWHM defines the maximum achievable resolution of a telescope and is given by:

$$\alpha[rad] = 1.22\frac{\lambda[\mu m]}{D[m]} \tag{1.26}$$

In addition to the PSF another important quantity often used in the turbulence imaging framework is the Optical Transfer Function (OTF). It is related to the PSF via its Fourier Transform:

$$OTF(k) = \mathbf{FT}(PSF(r)) \tag{1.27}$$

The OTF can be interpreted as a measure for the response of an optical system. It describes how amplitudes of certain spatial frequencies become damped when propagating through an optical system. As a result of the Fourier formalism, the OTF of a whole system consisting of atmosphere and telescope is the product of their respective OTFs. Since the OTF of the telescope is solely static, it is not considered in the following. Combining equation 1.25 and 1.27 the atmospherical OTF can be written as the autocorrelation function of the complex wavefront amplitude in the pupil plane.

Following Roddier (1999), the atmospherical OTF is related to the phase structure function of an atmospherically distorted wavefront by:

$$OTF(\mathbf{r}) = \langle \exp[i(\Phi(\mathbf{r'}) - \Phi(\mathbf{r}+\mathbf{r'}))]\rangle = \exp[-1/2 D_\Phi(r)] \tag{1.28}$$

Using $\mathbf{k} = \mathbf{r}/\lambda F$ where λ is the imaging wavelength and F the focal length and assuming moreover radial symmetry ($k = abs(\mathbf{k})$), one can deduce expressions for short time ($T_{exp} << \tau_G$) and long time exposure OTFs ($T_{exp} >> \tau_G$) for Kolmogorov turbulence using equation 1.9:

$$OTF(k)_{se,le} = \exp[-3.44(\frac{\lambda F k}{r_0})^{5/3} \cdot A] \tag{1.29}$$

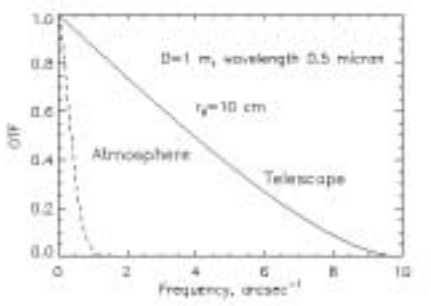

Figure 1.5: The OTF as a measure of the response of an optical system: While a telescope (solid line) also passes - depending on the telescope diameter - high order spatial frequencies, which contribute to the final image, the atmosphere (dashed line) leads to a cut off at low spatial frequencies.

The value of the parameter A depends on the exposure-time and is 1 for long time exposures while for short time exposures it becomes:

$$A = (1 - 0.5(\frac{\lambda F k}{D})^{1/3}) \tag{1.30}$$

In the first case the atmospherical OTF drops down very fast to 0 resulting in a strong damping of high spatial frequencies (see Figure 1.5). Those are not able to contribute anymore to the PSF shape. As an ultimate effect, the shape of the PSF does not depend any more on the diameter of the telescope but is determined by the atmospherical parameters.

1.4 Partial Correction of the Atmosphere

1.4.1 The AO-PSF

AO-systems provide only a partial correction of the turbulence degraded PSF. Depending on the quality of the performed correction, the AO-PSF may be seen as a kind of intermediate state between the seeing disk and the ideal Airy-disk. In order to understand the formation and resulting shape of a long term exposure PSF one may start by considering a short term exposure PSF first (recorded with an integration time of the order of τ_0). A short exposure PSF is dominated by a characteristic speckle pattern. Its origin can be deduced from interferometric considerations. An incoming distorted wavefront impacting at the telescope pupil of diameter D, can be decomposed into small parts of the order of the size r_0 defining independent sub-apertures. Each sub-aperture is characterized by a random orientation of the enclosed wavefront tilt. The resulting speckle pattern is finally formed by constructive interference of waves from sub-apertures with similar wavefront tilts. Hence, according to diffraction theory, speckles have a size of roughly λ/D and are randomly distributed over an area λ/r_0, which defines the size of the seeing disk (see Figure 1.6 (left)). Due to the temporal variability of the phase of the incoming wavefront, the speckle pattern changes in time and results - in the case of a long term exposure - in the seeing disk. When turbulence is compensated by means of Adaptive Optics, the residual phase error decreases and energy is transferred coherently from the seeing halo to the diffraction limited core of the PSF. The latter starts to appear at residual phase errors below 2rad RMS. Hence, a partially corrected PSF is characterized by a diffraction limited core located above the residual seeing limited halo (see Figure 1.6 (right)). The halo is formed by the incoherent summation of speckle noise originating from residual (uncorrected) wavefront errors. Thus, increasing the quality of the

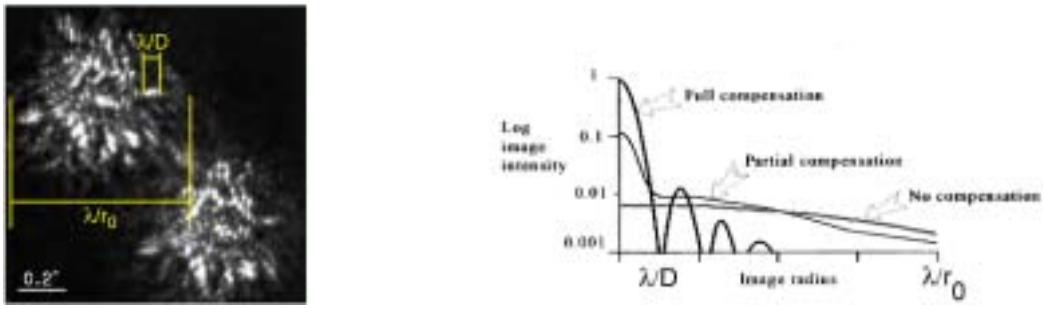

Figure 1.6: **Left:** Typical speckle pattern as seen in short term exposures with an integration time of the order of τ_0. Speckles of size λ/D are randomly spread over an area λ/r_0 (image is taken from Vernin et al. (1991)). **Right:** Effects of wavefront compensation on the peak contrast ratio, Strehl-ratio and intensity profile of the turbulence-degraded PSF (plot taken from Hardy (1998)).

correction, more and more energy is transferred from the halo into the core. The properties of long term exposure AO-corrected PSFs was intensively studied within the last years, for instance by Veran et al. (1997).

1.4.2 Strehl-Ratio

An important quantity to classify the quality of the partially corrected PSF is the Strehl-ratio (Strehl (1902)). As shown above, residual wavefront errors lead to a degradation of the shape of the ideal PSF, since some flux of the diffraction limited core will be redistributed in the seeing halo, which leads to a decrease of the peak intensity. By comparing the peak intensity of the partially corrected PSF with the peak intensity of the corresponding Airy-disk, one obtains a measure for the correction quality. Following Hardy (1998), the Strehl-ratio is defined as:

$$S = \frac{I(P)}{I^*} = \frac{1}{\pi} \mid \int_0^1 \int_0^{2\pi} \exp\left(ik\Phi(\rho,\Theta)\right)\, \rho\, d\rho d\Theta \mid^2 \tag{1.31}$$

where $I(P)$ and I^* are the peak intensities of the partially corrected PSF and the corresponding ideal PSF. $\Phi(\rho,\Theta)$ denotes the aberrated wavefront. By evaluating the integral one finally obtains an approximation, describing the Strehl-ratio as a function of the residual variance of the phase error σ^2 (Maréchal (1947)):

$$S \approx \exp(-\sigma^2) \tag{1.32}$$

1.5 Wavefront Sensors

1.5.1 Shack-Hartmann Sensor

The Shack-Hartmann sensor (SHS) is the most commonly used sensor type enjoying a big acceptance within the astronomical AO-community, which is associated with its simple and straightforward principle of operation. The sensor has intensively been investigated and tested for its performance depending on constraints like limiting magnitudes (Feautrier et al. (2000)) and noise propagation (Kasper (2000)). Invented at the beginning of the last century and mainly used for lens testing purposes (Hartmann (1900)), the SHS subdivides the pupil into small sub-apertures of the order of r_0 by means of a lenslet array (see Figure

1.7). The local wavefront slope of an aberrated wave $\Phi(x, y)$ can be measured by the angular displacement α_x in each sub-aperture with respect to a reference position (Roddier (1999)):

$$\alpha_x = \frac{c_x}{fM} = \frac{\lambda}{2\pi A_{sa}} \int_{sa} \frac{\partial \Phi(x, y)}{\partial x} dxdy \tag{1.33}$$

A_{sa} denotes the size of the sub-aperture, c_x the spot displacement on the detector, f the focal length of the microlens and M the magnification factor between pupil plane and microlens plane. A big advantage of this sensing concept is the linear response of the sensor with respect to the local tilt.

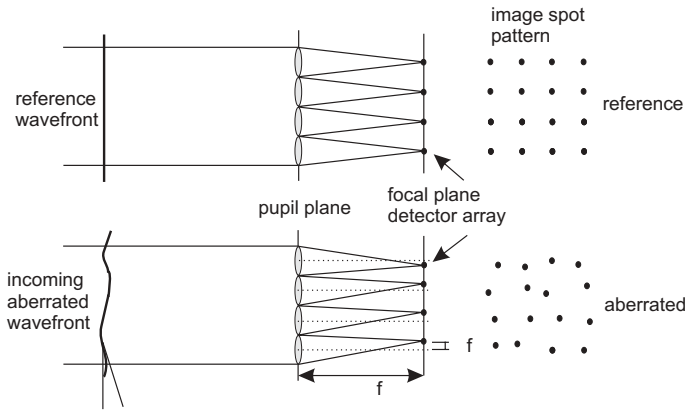

Figure 1.7: Function principle of a Shack-Hartmann-Wavefront sensor: By means of a lenslett array the pupil is divided into sub-apertures. Local wavefront tilts result in a characteristic shift in the x,y direction of each sub-aperture image with respect to their reference position

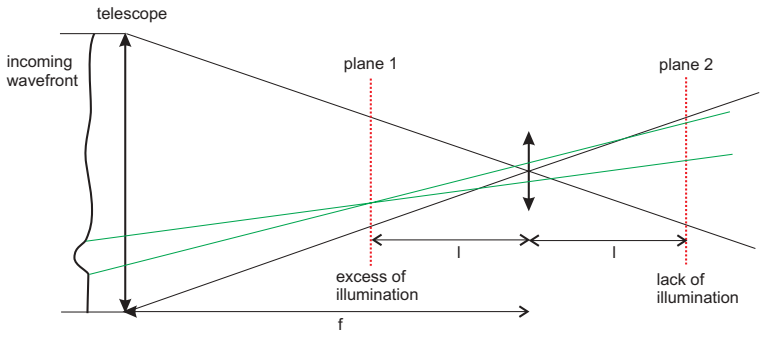

Figure 1.8: Function principle of a Curvature Wavefront sensor: The local curvature can be determined by measuring the change in intensity of two symmetrically out of focus images.

1.5.2 Curvature Sensor

In addition to the SHS, the curvature wavefront sensor (CWFS) has already proven its efficiency mainly for low order adaptive optics corrections and is adopted at several telescopes like Gemini, CFHT, SUBARU and VLT. Originally proposed in 1988 by F. Roddier the CWFS measures the curvature of an incoming wavefront (Roddier (1988)). This is achieved by recording the intensity distribution at two symmetrically arranged out of focus positions. In practice a field lens is conjugated to the pupil plane and a fast oscillating membrane provides de-focussed pupil images on a CCD detector. In order to reconstruct the wavefront, the

Poisson equation with Neumann boundary conditions has to be solved. The latter are given by the radial wavefront tilts at the edge of the pupil. According to Figure 1.8, a positive local wavefront curvature leads to an excess of illumination at a certain point at plane 1 (at a distance l before the focus), while simultaneously a lack of illumination at the corresponding point at plane 2 is recorded. In the geometrical optics approximation, the normalized difference between the two intensity distributions $I_1(\mathbf{r})$ and $I_2(\mathbf{-r})$ is related to the wavefront phase error $W(\rho, \theta)$:

$$\frac{I_1(\mathbf{r}) - I_2(\mathbf{-r})}{I_1(\mathbf{r}) + I_2(\mathbf{-r})} = \frac{f(f-l)}{2\pi l}\left[\frac{\partial W(\rho,\theta)}{\partial \rho}\delta_c - \nabla^2 W(\rho,\theta)\right] \tag{1.34}$$

Here δ_c is a linear impulse distribution around the pupil edge, f the focal length, and l the distance from the focal plane to the two out of focus screens. Equation 1.34 contains all information necessary to extract the information about the entire wavefront and exhibits moreover that the gain of the curvature sensor can also be adjusted by varying l. This results in a very flexible system, which can be adjusted to the seeing conditions (optical gain).

1.5.3 Pyramid Sensor

The local wavefront slope can also be obtained by another kind of WFS using a glass pyramid as sensing device (Ragazzoni (1996)). The Pyramid WFS (PWFS), as an extension of the Focault knife test, measures the local tilt not in the focal but in the pupil plane (unlike the SHS). Considering the geometrical optics approximation, the stellar light is focussed on the tip of the pyramid (See Figure 1.9). The pyramid will split the incoming light into four pupils of full aperture. These are re-imaged on a detector by a relay lens. Assuming now a local wavefront tilt at the pupil, light rays of this region will hit only one side of the pyramid, leading to a bright corresponding spot in one of the four corresponding pupil images, while the other three remain dark. Such a configuration is only able to detect the sign of the local wavefront slope, but cannot measure the amplitude of the tilt, since the recorded illumination pattern of the four pupils does not depend on the position where the aberrated ray hits the side of the pyramid. Nevertheless, the information about the slope amplitude of the local tilt is intrinsically hidden, since the relative distance of the aberrated ray from the vertex of the pyramid is proportional to its slope. Hence by introducing a periodic oscillation of the stellar PSF over the pyramid vertex, one can measure the amplitude of the local slope, since the detector does not saturate instantaneously. Following Riccardi et al. (1998) in the case of small signals a linear relation between the local wavefront tilt in the x,y-direction and the signal in the re-imaged pupil plane is given by:

$$\frac{\partial W(x_p, y_p)}{\partial x_p} = a_0 \frac{\pi}{2} S_x \tag{1.35}$$

$$\frac{\partial W(x_p, y_p)}{\partial y_p} = a_0 \frac{\pi}{2} S_y \tag{1.36}$$

a_0 defines the amplitude of the oscillation and S is given by the intensity distribution at the re-imaged pupils:

$$S_x(x_i, y_i) = \frac{(I_A(x_i, y_i) + I_D(x_i, y_i)) - (I_B(x_i, y_i) + I_C(x_i, y_i))}{\sum I_i(x_i, y_i)} \tag{1.37}$$

and

$$S_y(x_i, y_i) = \frac{(I_D(x_i, y_i) + I_B(x_i, y_i)) - (I_A(x_i, y_i) + I_C(x_i, y_i))}{\sum I_i(x_i, y_i)} \tag{1.38}$$

$I_j(x_i, y_i)$ denotes the intensity at position x_i, y_i for pupil-image j. Obviously, the gain of the PWFS can also be adjusted in closed loop by changing the oscillation amplitude, which makes it much more flexible to react to changing seeing conditions. Furthermore - in the case of

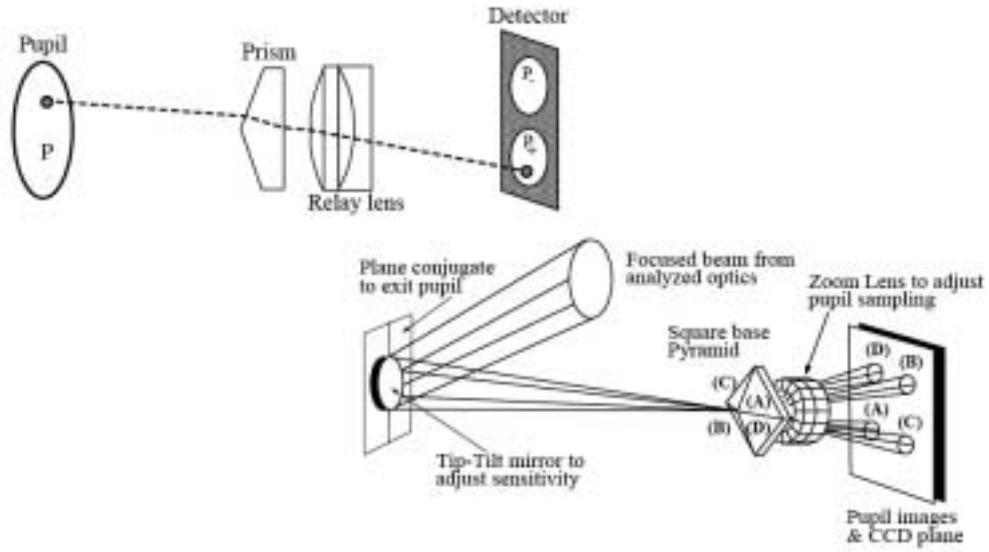

Figure 1.9: Principle of Pyramid Wavefront Sensor. **Up:** A prism splits the incoming light into four pupils of full aperture, which are re-imaged by a relay lens. A local wavefront tilt leads to a changing intensity pattern in the corresponding pupil images, which gives the sign of the tilt, but not its absolute amplitude. **Down:** In order to reconstruct the amplitude of the local wavefront slope, a periodic oscillation of the PSF is introduced by means of a tip-tilt mirror .

point-like reference sources - the PWFS leads to a higher sensitivity (fainter limiting magnitude) when a diffraction limited correction at the sensing wavelength is achieved (Ragazzoni (1996), Esposito et al. (2001)). Due to its pupil plane sensing fashion, the pyramid WFS can be used for a layer-oriented Multi-Conjugated Adaptive Optics (MCAO) system (see section 1.6). However the PWFS is not suitable for large (static) wavefront aberrations due to the very limited dynamic range (Costa (2005)).

1.6 Limitations of Conventional AO and Current Trends

Although astronomical adaptive optics is a very powerful method to reach diffraction limited imaging, it is still hampered by limited sky coverage arising from a combination of two issues:

- **Limiting magnitude of guide star:** Bright reference sources are required, since the limiting magnitude of the guide star does not depend on the telescope diameter but is influenced by the sub-aperture size and integration time of each WFS measurement cycle as well as by the readout noise of the detector. WFS-units on modern AO-instruments like NACO reach a limiting magnitude in the visible (0.45-0.8micron) of 16th mag and in the NIR (0.8 - 2.5 micron) of 12th mag (for a sub-aperture size of $\sim 1.1\ m$ and an integration time of $\sim 20\ ms$).

- **Anisoplanatic effects:** Only in very rare cases (for instance search for planetary companions)is the science target suitable to be used as guide star to track wavefront aberrations. In general, bright stars close to the science target provide light for the WFS. This approach leads to an additional measurement error arising from anisoplanaticity. Reference stars and science target are in slightly different directions, so that

their light rays incidenting on the telescope pupil probe different parts of the atmosphere. Therefore, the WFS measures a different wavefront deformation than the one which really has to be corrected (see Figure 1.10 (left)). The additional error $< \sigma_\theta^2 >$ can be estimated from the accumulated phase error difference of light rays probing the turbulent atmosphere in two different directions θ (Hardy (1998)):

$$< \sigma_\theta^2 >= 2.914 k^2 (\sec\gamma)^{8/3} \Theta^{5/3} \int_h dh C_N^2(h) h^{5/3} \tag{1.39}$$

Here implicitly $D \gg r_0$ is assumed. According to the definition of r_0 and τ_0 one can define $\theta_0 = \left[2.914 k^2 (\sec\zeta)^{8/3} \int_h dh C_N^2(h) h^{5/3}\right]^{-3/5}$ as the angular separation for which the accumulated variance of the phase error reaches $1 rad^2$. The opening angle θ_0 defines the isoplanatic patch and the variance of the residual wavefront error can be written as:

$$< \sigma_\theta^2 >= (\theta/\theta_0)^{5/3} \tag{1.40}$$

As a result of the increasing wavefront aberration, the quality of the correction drops down with increasing angular distance between science target and guide star, limiting the usable Field of View (FoV) per guide star. The maximum possible separation depends mainly on the seeing-quality and the corrected wavelength band. It can range from several arcseconds (in the visible) up to 20-30 arcseconds (in the K-band).

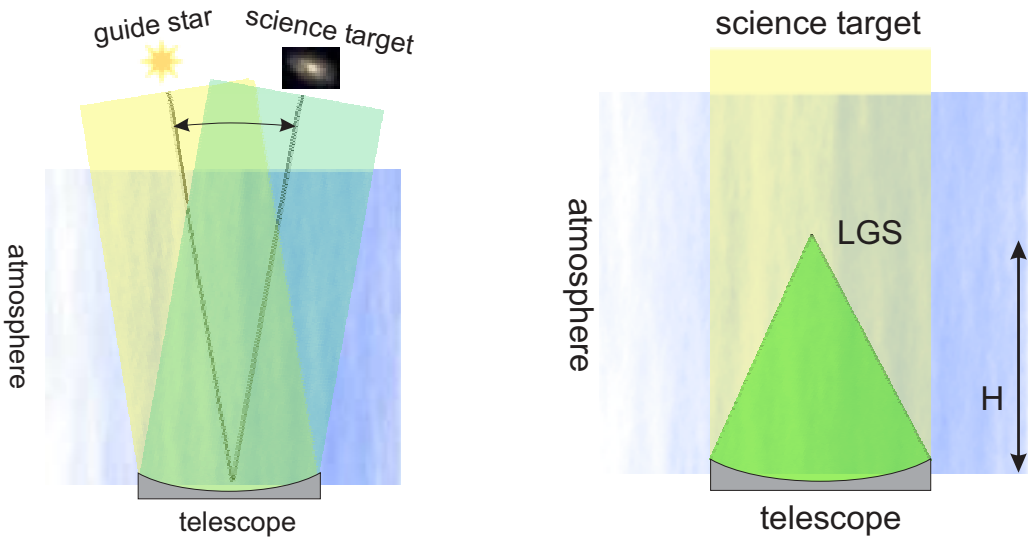

Figure 1.10: Origin of angular (left) and conical (right) anisoplanatism. Left: Light rays of guide star and science target probe different parts of the atmosphere leading to a mismatch of the measured guide star wavefront and the science target wavefront. Right: Due to the finite distance of the laser beacon, light rays of the reference source do only probe parts of the turbulent atmosphere.

Summarizing both effects, the availability of AO corrections over the entire sky depends on the distribution of suitable guide stars. The lack of a high enough density (Bahcall et al. (1980)) of bright sources leads to low sky-coverage of AO-systems using natural guide stars (NGS) (See Figure 1.11 (left)). Due to the demands in terms of sub-aperture size, integration time and anisoplanaticity, sky coverage is a function of wavelength and becomes higher for longer wavelength.

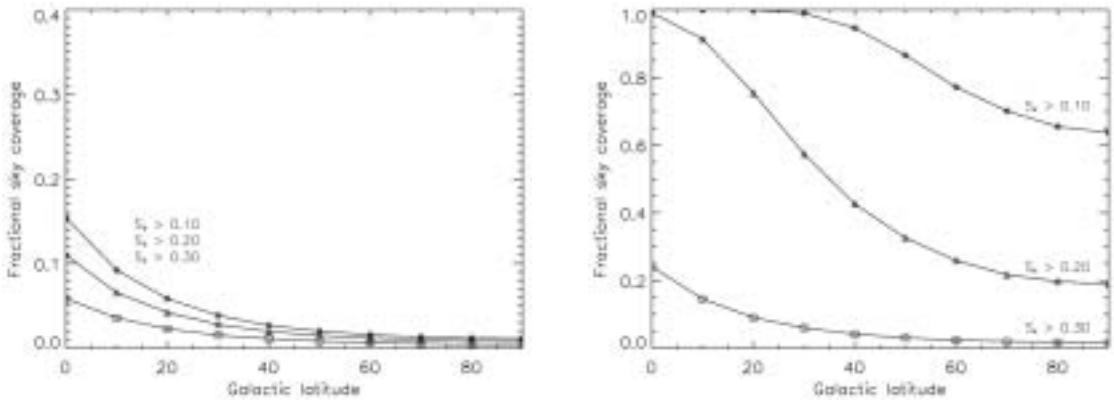

Figure 1.11: Comparison of achievable sky coverage as a function of Strehl-ratio S in K-band and galactic latitude using NGS (left) or LGS (right). Note the different scales used for the sky-coverage. A star density according to Bahcall et al. (1980) is assumed. The limiting R-band magnitude for the NGS case is 13.5mag, while the limiting magnitude in the LGS case is 18.5mag. For the simulation an isoplanatic patch size of 20 arcseconds has been assumed. Both plots were calculated at W.M. Keck observatory.

1.6.1 Increasing the Sky Coverage - Laser Guide Stars

A promising approach to extend the sky coverage (see Figure 1.11 (right)) is by projecting artificial stars close to the scientific target (Thompson et al. (1987)). This idea came already up in the late 1970s (for military applications) and its feasibility was proven the first time in the early 1980s at SOR (Fugate et al. (1991)). For pure astronomical applications Foy and Labeyrie (1985) discussed the usage of a laser beam to probe the turbulent atmosphere for its distortions. Although a Laser Guide Star (LGS) in any case can be created within the isoplanatic patch around the science target, a full sky coverage is not achieved due to the absolute tip-tilt indetermination (see Figure 1.12, Pilkington et al. (1987)) problem. Although several attempts have been made to overcome this problem (Foy et al. (1995), Ragazzoni (1996), Ragazzoni (1997)), still the most favored approach is to sense a natural guide star (NGS) to obtain information about the tip-tilt of an incoming wavefront, and use the LGS for all high order corrections. Tip-tilt guide stars can be much fainter, since only

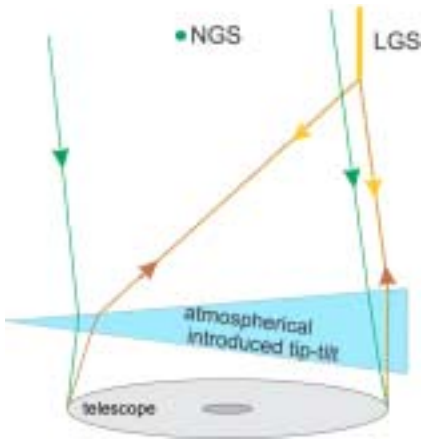

Figure 1.12: Problem of tip-tilt indetermination of LGS-light probing the atmosphere. Unlike a NGS, a LGS is launched from the ground. Light rays from the laser projector will intersect the turbulent atmosphere two times resulting in a lack of tip-tilt information.

two modes have to be measured leading to less sub-apertures and lower noise propagation. Moreover, the distance of the reference star to the scientific target can be increased, since angular anisoplanatism effects decrease for low order aberrations (Rigaut et al. (1992), Flicker et al. (2003)). In contrast, for pure tip-tilt correction, the demands on loop frequency are almost as high as for high order modes, since temporal de-correlation is only a weak function of the mode (see Figure 1.4). However, the gain in sky-coverage is not for free, because it implies focal anisoplanatism resulting from the finite distance of the laser beacon (Welsh and Gardner (1991), Fried and Belsher (1994)). According to Figure 1.10 (right), light of the LGS does not sample the entire atmosphere (as a NGS) but only a cone. In analogy to equation 1.40 the resulting phase error $< \sigma^2_{cone} >$ can be described by:

$$< \sigma^2_{cone} >= (D/d_0)^{5/3} \tag{1.41}$$

The quantity d_0 describes the diameter of the telescope aperture over which the cone-effect leads to a wavefront error of 1 rad^2. d_0 is a function of the observing conditions similar to r_0 and τ_0, but depends moreover on the focussing height of the Laser. In the case of sodium LGSs, assuming a correction in the NIR, d_0 is of the order of 5-10m. The cone effect can in principle be overcome by using several LGS to sample the entire turbulence volume below the LGSs (Tallon and Foy (1990), Johnston and Welsh (1994), Lloyd-Hart et al. (2005)), leading to turbulence tomography (see Figure 1.13), which is discussed in more detail further below.

How are LGS created? At the moment two different ways are known:

- **Rayleigh beacons:** The Rayleigh backscattered return signal of a laser fired into the atmosphere can be used for wavefront sensing (Fugate (1994) , Laurent (1995), Thompson et al. (2002)). In this case the Laser is focussed at a low altitude of 10-20km. Since the laser light will be backscattered at all altitudes, a selection of light rays coming solely from a certain altitude (range gating) is achieved using a pulsed laser, synchronized to a shutter at the WFS-CCDs. Although Rayleigh LGS are cheap and reliable, they are not widely used for AO purposes, since they suffer severe disadvantages such as a huge conical anisoplantism and perspective elongation effects (see section 2.1). The low focussing height recently turned into an advantage by the appearance of the Ground Layer Adaptive Optics (GLAO) concept (Rigaut (2002)). In this particular case one is interested to extract the information about ground layer turbulence, located within the first kilometer above the ground. This favors a low focussing height of the laser beacon.

- **Sodium beacons:** Several authors (for instance Happer et al. (1994)) favor a different approach. In the mesosphere, at a height of 90-100km, exists a layer with a thickness of roughly 10km enriched by sodium (10^{13} Atoms per m^3). These atoms can be excited by a laser beam tuned to the corresponding Na-D2 lines to perform a resonant backscattering. This leads to a reference beacon at high altitude. Due to the high demands in terms of laser power and stability, however, this type of guide star is technically and financially challenging. Moreover, several parameters of the sodium layer such as number of atoms, height and thickness change seasonally and during the night (Butler et al. (2003)). Additionally, one has to compensate a varying focussing position of the LGS in the image space, which depends on the viewed zenith angle. Nevertheless, sodium LGS are successfully operated at several $8 \ldots 10$m class telescopes (Bouchez et al. (2004), Rabien et al. (2004), van Dam et al. (2004)).

1.6.2 Current Trends - Different AO for Different Science

For more than 15 years Adaptive Optics is now a proven concept to reach diffraction limited image quality, and AO-systems are available as facility instruments at almost all 8...10m class telescopes. Different demands depending on the conducted science lead to a wide spreading of requirements for current AO instruments.

Extreme Adaptive Optics

Exo-planetary search favors a correction in the visible or near-infrared wavelength band, generating as low speckle pollution as possible. Requirements on the FoV are relaxed since planetary companions are supposed to be found mainly within a few arcseconds around the host star. Hence an AO-system is desired which is able to remove high spatial frequencies in the phase error at a high temporal bandwidth (1-2 KHz). In the case of a 8...10m telescopes this implies a DM consisting of more than 1000 actuators to achieve high Strehl values of the order of 95%. Feasibility studies of such *extreme AO-systems* are done for several 8...10m class telescopes (for instance Feldt et al. (2003)) and planned to be implemented as 2nd or 3rd generation instrumentation.

Multi-conjugated Adaptive Optics

In contrast, high resolution imaging over a bigger FoV at moderate Strehl-ratio but with a high uniformity of the PSF, is desired to resolve structures of extended sources. Multi Conjugated Adaptive Optics (MCAO) (Rigaut et al. (2000)), Beckers (1988)), is a promising approach to achieve diffraction limited image quality over FoVs of up to 1-2 arcminutes. Recapitulating the previous section, in the case of classical AO the integrated wavefront phase error over the line of sight of the WFS is measured. This leads to anisoplanaticity effects, which arise due to the lack of information about turbulence within the entire 3-d volume of the FoV (this is even more severe in the case of LGS, caused by the low focussing altitude).

In the case of MCAO, the complete information about the turbulent atmosphere within the FoV is retrieved by the means of several guide stars, which illuminate the entire turbulent volume from several directions (see Figure 1.13). Turbulence tomography, as one possibility to compute the induced phase error of a certain turbulent layer, is introduced in this framework (Tallon and Foy (1990)). It finds its practical implementation in the star oriented approach, where one wavefront sensor is conjugated to one guide star. In this case the information about different directions sampled by each WFS is combined to give implicitly the 3-d information of the atmosphere within the FoV (Ellerbroek et al. (1994)). Then, the influence of a single turbulent atmospherical layer can be computed and hence, each significant layer can be corrected by a conjugated DM. The tomographic approach has been verified 1999 (Ragazzoni et al. (2000)) in an open loop measurement, done at the Telescopio Nazionale di Galileo (TNG). Although much efforts have been put into turning tomography into a robust and adoptable technique (Ragazzoni et al. (1999)), obviously this technique requires a huge amount of computational power and therefore puts stiff constraints on a real time system.

A different attempt in the framework of MCAO to obtain information about a single turbulent layer has been introduced by Ragazzoni et al. (2000). In the so called layer-oriented approach, each WFS-camera is not conjugated to a single star, but to a turbulent layer one wants to correct. In this way the number of required WFS-cameras can drastically be reduced, limiting the drawback of readout noise of the detector. Moreover, light of several guide stars

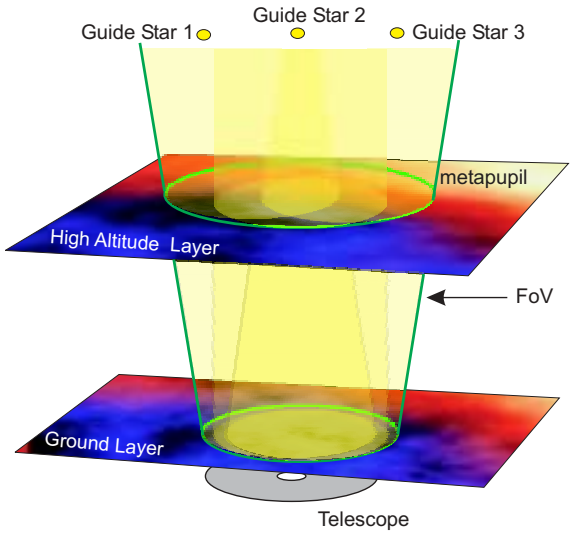

Figure 1.13: Principle of atmospheric tomography. Several guide stars (NGS or LGS) illuminate the volume within the FoV probing in this way the entire atmosphere. The number of necessary guide stars depend on the altitude of the highest turbulent layer one wants to correct. A full correction is only guaranteed as long as this layer is fully covered by the footprint of the guide star metapupils.

can optically be co-added such that one is able to use fainter guide stars. The complexity of the entire MCAO-instrument can be minimized, since the information concerning one layer can be directly fed from the conjugated WFS into the corresponding DM resulting in a combination of independent control loops. Although the layer-oriented concept might look superior to the star-oriented MCAO approach, it also suffers some limitations. Strongly varying guide star brightness will lead to an overestimation of turbulence from a certain direction in the case of optical co-adding (Nicolle et al. (2004)). Another problem is that may be (this has not been investigated further up to today) both loops cannot be operated completely independently, assuming a nested loop configuration. A WFS conjugated at a certain height, will "see" the applied shape of DMs conjugated to other heights de-focussed. Thus it will be sensitive to low order spatial frequencies of the correction unit. This may lead to instabilities or even singularities in the control process. Hence a cascading system may be required, implying additional optical enhancements.

Sky coverage of layer-oriented MCAO can be enhanced by applying the Multiple Field of View concept (MFoV, Ragazzoni et al. (2002)). In this case guide stars from a certain annular FoV enclosing the science FoV are used to feed one WFS, which is conjugated to a turbulent layer.

Star- and layer-oriented concepts are still discussed controversially concerning performance expectations and correction quality. Therefore ESO plans in 2006 to operate with MAD (Multi-conjugate Adaptive optics Demonstrator), the first demonstrator to verify and compare star and layer-oriented concepts at the VLT. Several other MCAO instruments are planned at different telescope facilities. Gemini observatory develops a sodium LGS assisted MCAO instrument for Gemini south. The Fizeau-Interferometer LINC-NIRVANA for the Large Binocular Telescope (LBT) will be equipped with two layer-oriented MFoV correcting units providing a flat wavefront for the beam combiner (Gaessler et al. (2004)).

Ground-Layer Adaptive Optics

Measuring and correcting solely the influence of the ground layer turbulence is worthwhile to consider, as has been proposed recently (Rigaut (2002)). By correcting only the ground layer turbulence, one removes the major contributor to phase aberrations of incoming wavefronts. The correction is valid over big FoVs since the ground layer looks the same for different directions as a consequence of its proximity to the telescope pupil. Several simulations done for potential NGS or LGS Ground Layer Adaptive Optics (GLAO) configurations (Tokovinin (2000)) suggest that GLAO would reduce the seeing disk of a PSF in the H-band by up to a factor of 5 over a FoV of several 10th of arcminutes. GLAO may be seen as "MCAO light", since one needs the tomographic knowledge about the turbulent atmosphere, but operates only a single correction loop conjugated to the ground. In this context the Rayleigh LGS undergoes kind of a reincarnation due to the low focussing altitude, which automatically illuminates only the ground layer turbulence (Morris et al. (2004)). GLAO becomes an interesting alternative to the classical AO approach in order to increase the spatial resolution of, for instance, an Integral Field Spectrograph Unit (IFU) (Hubin et al. (2004)).

1.7 Extremely Large Telescopes

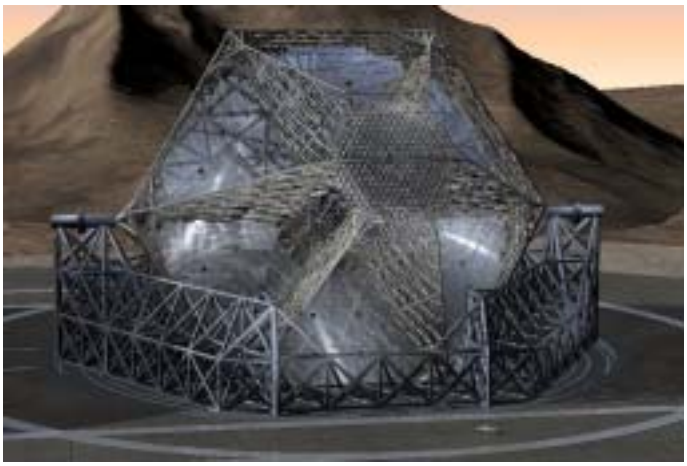

Figure 1.14: Computer simulation of the mechanical structure of OWL. The telescope is operated without a dome, leading to severe complications on mechanical accuracy and windload.

While modern 8 . . . 10m class telescopes at the moment are equipped with 1st generation instrumentation, in parallel several ongoing projects are conducted to study the feasibility of telescopes in the range from 30m to 120m in primary mirror diameter (Gilmozzi et al. (1998), Andersen et al. (2000), Mountain et al. (1997)). Such Extremely Large Telescopes (ELTs) are supposed to be realized within the next 10-20 years at expected construction costs of up to 1GEuro. ELTs like the planned Overwhelmingly Large Telescope (OWL), a project promoted by the European Southern Observatory (ESO), would have a resolving capability better than 1 mas at a wavelength of $0.5\mu m$. This opens windows for completely new science like imaging and spectroscopy of Earth-like exo-planets (Chelli (2005), Hawarden et al. (2003)), the study of the stellar evolution in *extra-galactic* star forming regions or precise measurements of cosmological parameters. ELTs will be in direct competition to planned NIR space telescopes like the JWST. In the optical wavelength band - assuming a full AO correction - ELTs are clearly superior in terms of point source detectability due to the much bigger mirror diameter (see Figure 1.15). This advantage, however, vanishes to

longer wavelengths. In the mid-infrared ELTs suffer from background flux originating in the Earth's atmosphere and from warm optical surfaces of the telescope, which severely constrain the achievable S/N-ratio.

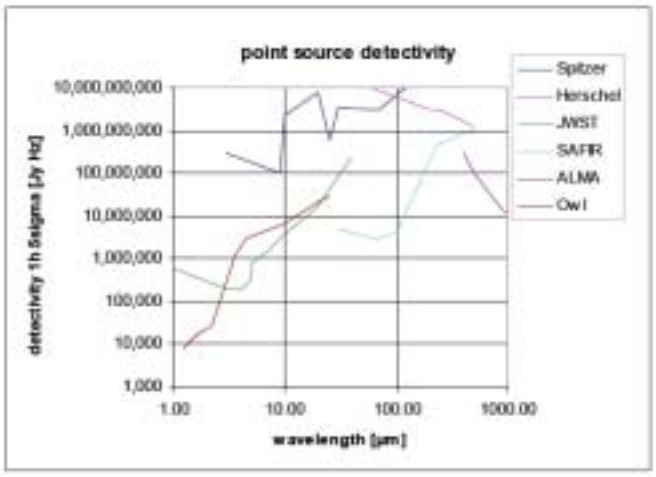

Figure 1.15: Comparison of point source detectivity of several planned observatories. The OWL 100m version would be competitive up to the mid-infrared and thus suitable for JWST follow up observations. This plot was kindly provided by Rainer Lenzen.

Building an ELT with the current state of technology is quite challenging but not impossible. Nevertheless, its complexity will exceed by far all telescopic designs performed up to now. In order to give the reader a feeling about the enormous challenges and difficulties, in the following several aspects of the ESO OWL-100m approach are listed.

- **Opto-mechanical design:** To focuss the incoming light of the scientific target a complex *6 mirror solution* is considered. This includes a spherical segmented primary mirror, a flat segmented secondary mirror and four additional elements as corrector systems, to limit cost risks at optimal performance and FoV (Dierickx et al. (2004)). The dimension of the necessary imaging opto-mechanics to carry the mirrors exceeds the present limit of manufacturability (Brunetto et al. (2003)).

- **Mirror Segmentation:** In the case of OWL the diameter of the primary mirror is still not finally defined, and varies between a 60 m and 120 m solution. Primary and secondary mirrors will be composed of hexagonal elements with a size of 1.6 m. In the case of a 100m solution this results for the primary in more than 3000 segments. Taking into account a reasonable time-span of 6 years for filling the entire mirror, this leads to an overall daily mirror production of 1.4 mirrors and makes a fabrication at industrial level indispensable.

- **PSF study:** A segmented primary and secondary mirror results in a PSF of high complexity, even when assuming ideally co-phased segments (which is a further issue that has to be accomplished). Hence, a detailed knowledge of the PSF is essential for almost all astronomical applications. The resulting PSF has already been studied intensively (Yaitskova et al. (2002)) by means of computer simulations (see Figure 1.16).

- **Mechanical accuracy:**. An accurate pointing with long term stability has to be guaranteed and is a further critical issue. In order to move the entire telescope structure,

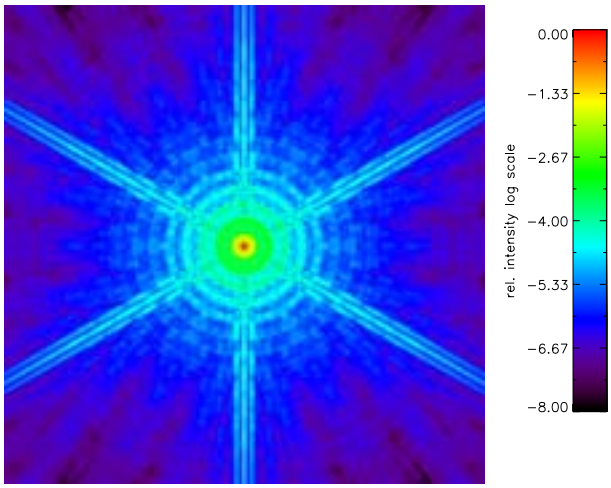

Figure 1.16: PSF-simulations done by the author in the framework of the T-OWL mid-infrared imager Phase A study for OWL. The simulation shows the resulting polychromatic PSF for a wavelength range from 10-11 micron,. It is taking into account the hexagonal segmentation of the OWL primary and secondary mirror including spider structure. The entire FoV visible is 2" × 2".

new ways in terms of materials and statical optimization have to be found to minimize its weight. As Figure 1.14 depicts, it is planned to operate the telescope without an enclosure, which additionally incorporates strong demands on the stability against windload (Quattri et al. (2003)).

- **Impact on AO:** In the case of OWL - even for most optimistic assumptions - the secondary mirror will be located at a height of 80m above the ground. Hence the incoming light when reflected by the primary intersects again a non negligible depth of the ground layer turbulence. Its impact to AO requirements is hardly studied up to now. This becomes even more severe for an observation at low zenith distance, since the primary mirror intersects the ground layer turbulence and could lead to strong inhomogeneities over the telescope pupil.

Obviously, an ELT will extremely cost intensive. Hence, ELTs become only interesting for the scientific community and justifiable for society if they reach their full capacity in terms of resolution and light concentration over a wide range of wavelength bands from the visible to the mid-infrared. This is even more so as only a few telescopes of this size will be built. As a consequence, an adaptive optics systems for such a telescope may not be seen as one facility instrument. AO-systems have to be part of the telescopic environment as a fully operational turn-key-system, which can be handled by visiting astronomers like for instance an auto-guider. This means in practice for the AO-system at an ELT:

- to be operational 365 days per year even under moderate to bad atmospherical conditions
- offering AO-support over a wide range of wavelengths from the optical to mid-infrared
- deliver good correction quality at sufficiently high Strehl-ratios
- offer nearly 100% sky coverage

Demands on a potential AO-system to fulfill the requirements mentioned above have been collected by Rigaut et al. (2000). They are summarized in Tables 1.3 and 1.4. According to

		r_0(550nm) = 10cm		r_0(550nm) = 20cm	
	Actuator pitch	SR($550nm$)	SR($1.65\mu m$)	SR($550nm$)	SR($1.65\mu m$)
case 1	10cm	74%	97%	90%	99%
case 2	25cm	25%	86%	64%	99%
case 3	50cm	2%	61%	25%	86%
case 4	100cm	seeing limited	21%	2%	61%

Table 1.3: Performance estimates of the Strehl-ratio at various actuator spacings assuming median and good seeing conditions.

	No. of actuators	Computational Power[Gflops]	CCD pixelrate[Mpixel/s]
case 1	200000	$9 \cdot 10^5$	800
case 2	30000	$2 \cdot 10^4$	125
case 3	8000	1500	31
case 4	2000	93	8
SOR	789	≈ 2	4x4.5

Table 1.4: System requirements for an AO-system at an ELT fulfilling the four cases denoted in Table 1.3. For comparison the system requirements for a currently operating high order AO-system at Star Fire Optical Range (SOR) are listed as well.

Table 1.3 sufficient Strehl-ratios over the entire wavelength range from the visible to the mid-infrared can only be obtained at an actuator spacing of 10cm - 20cm (which corresponds to case 1 and case 2). The resulting system requirements exceed by far the state of current AO and computer technology. Hence, assuming a required actuator spacing of 10cm (case 1) leads to a DM with an overall number of correction elements of 10^6. Although standard mirrors at the moment are equipped with actuators of about 10^3 elements, an interesting avenue to reach higher numbers are liquid crystal devices or Micro Electro-Mechanical Systems (MEMS). These systems are currently under developed, but they still suffer from a relatively small actuator stroke. This constraint might be overcome by nature itself. The pupil diameter of $8 \ldots 10$m class telescopes does not reach the dimensions of atmospherical outer scale. Thus, the overall wavefront tilt and the demands on actuator stroke scales with $D^{5/3}$. In the case of ELTs this may be strongly relaxed, taking into account outer scale effects of the turbulent atmosphere. Le Louarn et al. (2000), for instance, showed that for an outer scale of 25m the required actuator stroke at an 100 m-telescope will be approximately $5\mu m$.

A further issue is the availability of suitable CCD detector arrays, since - following the top level requirements of OWL (100 m approach) - a diffraction limited observation in the visible over a FoV of 30" $\times$ 30" would lead to detector size of 30000 $px \times 30000$ px.

Several papers already discussed the question of how to obtain high sky-coverage at sufficient Strehl-ratio over a certain FoV in the case of ELTs. Le Louarn et al. (2000) discussed several potential options to overcome the sky-coverage problem. A conventional solution using solely a single guide star is ruled out not only by the resulting low sky-coverage but also due to the restricted FoV. Using a single sodium LGS fails due to immense conical anioplanatism. Hence the only possible solution is by using a tomographic MCAO approach implying several guide stars. Ragazzoni (2000) pointed out constraints on the maximum useable FoV in the case of the tomographic approach, which is a function of the telescope diameter. In the case of a 100m telescope, the reachable FoV is of the order of 17' for NGS and 13' for sodium LGS. Moreover he verified that in the infrared a solution using solely NGS, within

a field of 12', results in a sky coverage of 50% at a median Strehl-ratio of 0.4. Going to the visible wavelength band Le Louarn et al. (2000) commented that the adoption of LGS is the only solution to guarantee a sufficient sky coverage at acceptable Strehl-ratio.

Chapter 2

The Pseudo Infinite Guide Star Technique

Laser guide stars in an (MC)AO framework have the promising capability to increase drastically the sky-coverage and currently several 8 . . . 10m class telescopes become equipped with such facilities (for instance Keck, VLT, Gemini). Regarding ELTs, adopting multiple sodium LGSs is an essential premise to attain a sufficient sky coverage over a large FoV in the visible wavelength band. This chapter will discuss drawbacks when scaling the sodium LGS-system to dimensions of ELTs, trace the origin of upcoming issues and point out the consequences. Furthermore it will introduce several technical approaches, which are currently under investigation, to counteract these problems. As a main part of this chapter a novel and alternative solution will be presented by introducing a new wavefront sensing concept. This technique will measure the phase distortions in the pupil plane by recording intensity fluctuations (pupil plane WFS). It is composed of two independently working sensing devices. These are a mask with circular slits and a reflective rod. The mask, able to measure phase distortions in the radial direction, is a completely novel technique introduced for the first time in this thesis and based on an inversion of the Bessel Beam concept. The reflective rod as representative of the z-invariant techniques was recently introduced. It measures the wavefront error in the azimuthal direction. As a further part of this chapter it is shown how both components can be combined by introducing a practical optical setup. Concerning light efficiency, the slit-mask will be moreover compared with the discussed alternative approaches such as "temporal gating", and a novel kind of gating technique will be presented. Finally it is shown that this sensing concept is compatible to all MCAO approaches by proposing possible MCAO optical setups.

2.1 Limitations of Sodium LGS at ELTs

For 8 . . . 10m class telescopes wavefront sensing with sodium LGSs is more challenging than in the NGS case, but with current WFS approaches (see 1.5) still feasible. However, adopting sodium LGS at ELTs, several effects become dominant, which can all be traced back to the fact that the artificial guide star takes shape in the mesosphere, resulting in two major constraints:

- The light source is positioned at a finite distance with respect to the telescope.
- The light source cannot be considered as a point source (like a NGS), but is strongly elongated in the vertical direction in dependence on the thickness of the mesospheric

sodium layer.

Both effects result in drawbacks for AO-systems discussed in the following sections:

2.1.1 Perspective Elongation and De-focussing Effects

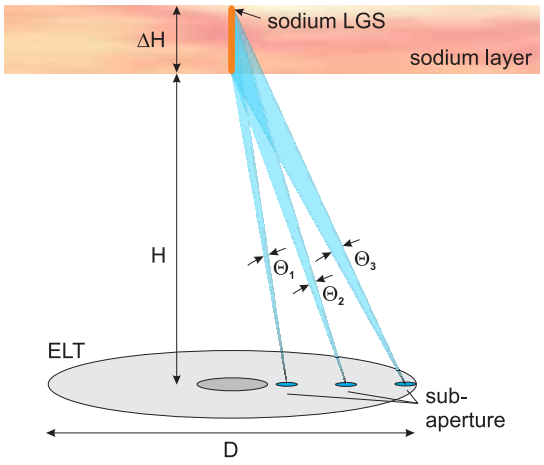

Figure 2.1: Perspective elongation: A sub-aperture at the edge of a telescope "sees" the laser beacon elongated due to its finite distance and its vertical extent in the mesosphere.

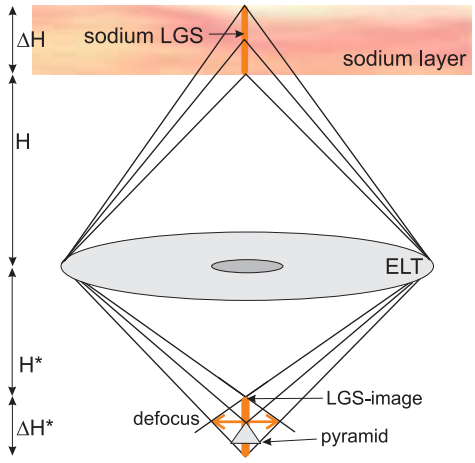

Figure 2.2: Defocus: A telescope will image the LGS extended in image space. Simultaneously, the WFS-device (e.g. a pyramid) can only be conjugated to a single plane leading to non-negligible defocussing effects.

A sub-aperture, located off-axis with respect to the laser projection axis, "sees" the extended light source elongated (see Figure 2.1). This effect is a function of the radial distance of the sub-aperture from the telescope center and becomes maximized for a sub-aperture close to the edge of the telescope. Assuming the geometric optics approximation, the maximum spot elongation θ may be described as

$$\theta \approx \frac{D\Delta H}{2H^2} \tag{2.1}$$

giving θ in radians. Here, H denotes the height of the light source above the telescope center, ΔH the vertical elongation, and D the telescope diameter. This leads to a spot elongation on the order of ≈ 10" for a D=100m telescope assuming that the sodium LGS takes shape in the mesosphere at an altitude of $H \approx 100\,\mathrm{km}$ and with a thickness ΔH of $\approx 10\,\mathrm{km}$. Note that this computation already implies an on-axis laser launch from the center of the pupil. This result translates into stringent demands on the FoV for each sub-aperture and also requires a huge number of pixels for the wavefront sensor CCD. As a consequence, hardware requirements in terms of physical size and fast enough read out capabilities become challenging. Additionally, such an elongation limits the accuracy of any centroiding technique, as the spot becomes more elongated with increasing radial distance from the center (Viard et al. (2001)). Even more problematic is the fact that under several circumstances the spot elongation could be larger than the isoplanatic patch itself. Perspective elongation becomes already an issue at 8...10m class telescopes considering an off axis launch of the laser. Figure 2.3 shows the effect of perspective elongation in the case of the W.M. Keck telescope. Hereby the laser projector was located 11.2m away from the optical axis, leading to a spot elongation of up to 3.5".

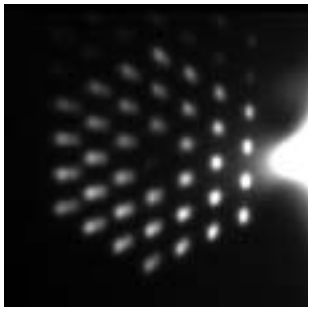

Figure 2.3: Perspective elongation of SHS spots. The laser projector is located at a distance of 11.2m from the optical axis. The resulting elongation is up to 3.5".

In general, conventional WFSs perform the sensing in a single plane, which is, depending on the sensor type, either the pupil plane or the focal plane. This 2-d approach only works because it is implicitly assumed that the light source is at infinite distance (which is in fact true for NGS). In this case all rays enter the optical system parallel and will be focussed at a single plane. Therefore perspective elongation - as one might think in the first instance - may not simply be overcome by using pupil plane wavefront sensors. In this case the effect of an extended source located at a finite distance impacts in a different way. In Figure 2.2 a pyramid wavefront sensor is assumed, conjugated to an extended light source in the image plane. The pyramid as the sensing device can exclusively be conjugated to one altitude, which leads to a de-focussed spot at the tip of the pyramid. The angular size of such a spot is the same as estimated in equation 2.1 for perspective elongation.

2.1.2 Huge Conical Anisoplanatism

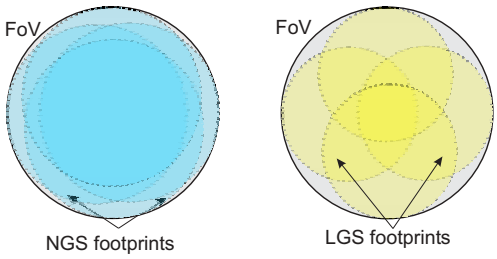

Figure 2.4: Effect of huge conical anisoplanatism in the case of tomographic MCAO. An increasing conical anisplanatism decreases the coverage of high altitude layers by the related footprints of the LGSs. Left: Coverage of a high altitude layer in the case of four NGS. Right: Corresponding coverage of a high altitude layer in the case of four LGS.

Conical anisoplanatism, another issue, was already discussed in the previous chapter. But it is often regarded to be solved intrinsically by implementing a MCAO setup. This statement is certainly only true as long as noise considerations are not taken into account. Because of the huge conical anisoplanatism expected for ELTs, a tomographic solution with LGSs is more noisy than a solely NGSs approach. This originates from the lower coverage of high altitude layers by the related footprints of the LGS. Hence, high altitude layers become by far less sampled with LGSs than by a corresponding NGS configuration (see Figure 2.4).

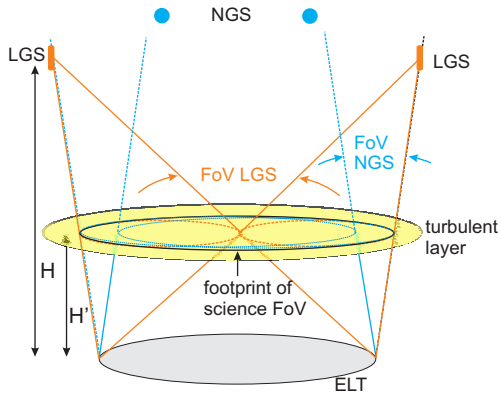

Figure 2.5: Elongated LGSs lead to severe constraints on the minimum FoV in the case of MCAO. In order to correct a science field of 3' at a D=100m telescope, the sodium LGS will be spread over a field of 14'.

2.1.3 Demands on FoV

In the case of MCAO, the finite distance of the LGS with respect to the ELT has an impact on the requirements on the minimum FoV. In order to sample the entire footprint of a given science FoV at a turbulent layer located at a height H' (see Figure 2.5 for details), light rays of the LGS will intersect the turbulent layer under bigger differential angles as in the case of NGSs. This leads to an increase of the required FoV for the WFS. A detailed treatment of this issue can be found in Farinato et al. (2005). He showed that correcting a science field of $3'$ at a D=100m telescope, in minimum five LGS have to be placed in a circular arrangement with a diameter of $14'$ to guarantee a proper turbulence coverage.

2.1.4 Ray Skewness

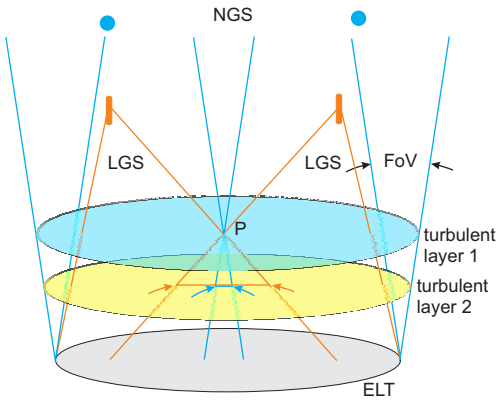

Figure 2.6: Ray skewness: In layer-oriented MCAO, low order spatial frequency contributions of non-conjugated layers can still be measured by a WFS depending on the grade of de-focus. In the case of ELTs, ray skewness leads to a faster de-focussing and thus to a faster de-correlation of non-conjugated layers.

The origin of the immense FoV demands translates in the case of layer-oriented MCAO into a further limitation. In the layer-oriented MCAO-approach, although the WFS is conjugated to one specific layer, it is nevertheless possible to recover low order spatial frequency

information of layers located below or above. This is possible since the WFS still sees such layers de-focussed. Unlike for NGS, the finite distance of the LGS results in bigger differential angles under which a specific layer is probed (see Figure 2.6). This leads to a faster de-focussing of non-conjugated layers, which decreases ultimately the correction efficiency of a layer-oriented MCAO system. Although it is a severe limitation, up to now this effect has been hardly investigated quantitatively, and should therefore be the subject of further studies.

2.2 Overcoming Perspective Elongation and De-focussing

2.2.1 Temporal Gating

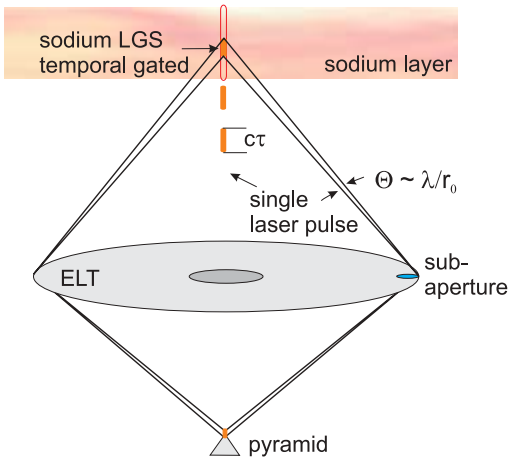

Figure 2.7: Defocus and perspective elongation can be reduced by using a pulsed Laser system. This however is connected with a considerable loss of light.

As shown above, especially perspective elongation and related de-focussing effects become significant already for 8 . . . 10m class telescopes in the case of an off-axis launch of the laser. Methods to counteract, like for instance temporal gating, are currently under investigation. Temporal gating is performed by means of a pulsed laser. The WFS-camera has to be synchronized to the repetition rate of the laser using a fast shutter on the CCD. Frames are only taken when each pulse reaches the desired height in the atmosphere (See Figure 2.7). In this way, temporal gating uses only a thin slice of the total excitable mesospheric column to form a laser beacon, which reduces the spot size on the WFS-detector. A typical upper limit for the thickness (and therefore the light efficiency) of such a slice is determined by the residual elongation, which practically is of the order of the seeing. In such a case standard WFSs are still able to operate without any loss of performance.

In the case of ELTs the residual vertical extent of the excited sodium layer leads to additional problems because it cannot be made arbitrarily small. Hence the elongation of the projected guide star is never smaller than a certain amount. Taking equation 2.1 and substituting ΔH by $c\tau$, where τ denotes the pulse duration, and constraining moreover the expression for the isoplanatic angle defined as the ratio $r_0/ < h >$, one obtains an upper limit to the macro–pulse duration given by

$$\tau < \frac{2 r_0 H^2}{< h > Dc} \tag{2.2}$$

where $< h >$ is the average height of turbulence (or, in MCAO, the highest layer where

the DM is conjugated to). Considering a sodium LGS at conventional 10m telescopes and assuming some reasonable numbers such as $r_0 = 10\text{cm}, < \text{h} >= 8\text{km}, \text{D} = 10\text{m}, \text{H} = 90\text{km}$, this leads to a minimum pulse-frequency of 20 kHz. For ELTs, this value will be increased by a factor of 10. Today, as has been pointed out by Thompson et al. (2002), no sodium laser facility exists which could reach such requirements for ELT diameters aiming at corrections in the visible. For instance, when increasing the pulse frequency of the laser, the shape of the produced output pulse degrades from a rectangular into a gaussian shape, limiting a proper synchronization with the CCD. Simultaneously, such an approach severely constrains the light efficiency. Photons, originating from non-temporal gated heights, which arrive when the CCD shutter is closed, cannot contribute to the recorded wavefront sensor signal. To counteract, one could put all energy into the pulse. This translates into higher power requirements with further technical efforts and would cause saturation effects within the sodium layer.

2.2.2 Dynamical Refocussing

An interesting attempt to increase the efficiency of the temporal gating technique is by using fast refocussing systems. Different solutions for this approach are discussed in the literature (Lloyd-Hart et al. (2005), Beckers et al. (2004)). One attempt is to follow the up-travelling pulse in the sodium layer by using in the image space a fast optical system (small F-ratio). In practice this is realized by means of a pulsating membrane, which dynamically refocusses a thin slice of the sodium layer. While dynamical refocussing is tested at 6m class telescopes, in the case of ELTs several difficulties have to be considered. For example, an increased dynamical range of the membrane which scales with the focal length of the telescope. (In the case of OWL, which presumably will have a F/6 optical design, the dynamical range will increase by at least a factor of 5).

2.3 The Pseudo Infinite Guide Star Wavefront Sensing Concept

Attempts like the fast refocussing techniques are more a pragmatic than an ideal solution, since they try to solve the problems by projecting the existing 3-d problem into a 2-d problem. Only then standard WFS methods can be adopted, because they are optimized for 2-d sensing (2-d sensing in this case means that the sensing device is conjugated to a single plane). Unfortunately this attempt can only be realized under immense technical efforts and leads in practice to increased system complexity.

This thesis, however, wants to follow a somewhat opposite approach and introduce a novel WFS-concept. As will be shown, this technique deals with the real origin of perspective elongation and all related effects in a much more natural manner. A new WFS concept overcoming such constraints is favorable, as long as it can easily be implemented, calibrated and handled in a reliable way, because it would reduce the complexity of an AO-system at an ELT. But how has such a wavefront sensor to be designed? As summarized in the previous section, all issues can be traced back to the finite distance of the LGS, in combination with its vertical extent in the atmosphere. Hence, the LGS as 3-d light source requires either a 3-d wavefront sensing device adopted to its shape, or one projects simply the LGS for the WFS-process virtually to infinity. The wavefront sensor ultimately proposed here is a combination of both ideas. A concept for a 3-d z-invariant wavefront sensor has been introduced by Ragazzoni et al. (2001), which is able to sense the incoming wavefront for azimuthal aberrations. The second technique, based on the inversion of the Bessel Beam method, is a completely new approach and is able to sense the incoming wavefront in radial

directions. In the next sections, both techniques will be explained in detail with a focus on the novel Inverse Bessel Beam concept. Moreover it is shown how, by combining both sensor types, the information about the entire wavefront can be retrieved, and finally an optical setup is suggested.

2.4 Diffraction-less Beams: The Bessel Beam Concept

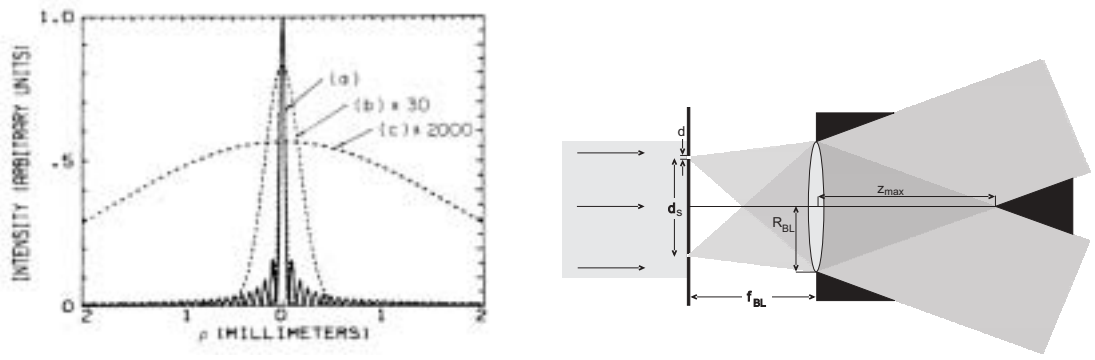

Figure 2.8: **Left:** Comparison of transverse beam profile of a Bessel Beam and a conventional Gaussian Beam of the same spot size propagating along the z-axis (perpendicular to the profile axis). While the Bessel Beam profile (solid line) is invariant along the axis of propagation up to a certain distance, the Gaussian Beam exhibits normal diffractive spreading, which is denoted by the dashed curves showing the beam profile after increasing distance (a=0m, b=1m and c=10m). **Right:** Arrangement to create a non-diffractive beam. Collimated light is sent through a circular slit mask in the focal plane of a lens with F-ratio $f_{BL}/2R_{BL}$. Behind the lens, the light will form a beam along the optical axis which does not diffract until the shadow zone at z_{max} is reached. Both Figures (left and right) were taken from Durnin (1987).

.

Bessel Beams are a concept to create diffraction-less beams over a certain range in the propagation direction of the light wave. Any beam with the intensity maximum along the axis of propagation is undergoing diffractive spreading proportional to the ratio of the wavelength λ over the beam size r. This leads to a rapid decrease of the on-axis intensity in the propagation direction of (see Figure 2.8 (left)). The spreading is determined initially by the nature of electromagnetic waves and gets increasingly noticeable at the distance r^2/λ, which is called the Rayleigh range. Techniques to reduce diffractive spreading have been pursued for a long time, for example to design super gain antennas (Toraldo di Francia (1952)). In Durnin (1987) solutions in free space to the Helmholtz wave equation

$$\left[\nabla^2 + \kappa^2\right] \Phi(r;\kappa) = 0 \tag{2.3}$$

are shown, which are non-diffractive over a finite distance without violating the law of diffraction. The simplest of Durnin's predicted non-spreading beam solutions, which satisfy equation 2.3, is a monochromatic wave, propagating in the z-direction with a field amplitude of

$$\Phi(x, y, z;\kappa) = \exp[i\beta z] J_0(\alpha\rho) \tag{2.4}$$

where $\alpha^2 + \beta^2 = \kappa^2$, $x^2 + y^2 = \rho^2$ and J_0 is the zero-order Bessel function. The half-width of the central peak is approximately given by α, while the envelope of the Bessel function decays as ρ^{-1}. These classes of solutions obviously have an intensity distribution in the x-y

plane denoted by the zero-order Bessel function. Hence these kinds of beams are referred to as Bessel Beams (see Figure 2.8 (left)). The theory is experimentally verified by Durnin et al. (1987) using a circular slit in the focal plane of a lens and illuminating it from behind with collimated monochromatic light of wavelength λ. The experimental arrangement is shown in Figure 2.8 (right). The lens transforms points in the focal plane, selected by a circular slit of width Δd, to plane waves of a certain direction. All these plane waves interfere along the optical axis until the end of the shadow zone defined by the circular aperture, z_{max}, providing within this distance a diffraction-less beam (z_{max} is determined by $R_{BL}/\tan(\theta)$, where θ is given by $tan^{-1}(d/2f_{BL})$). A variety of further possibilities exist to create Bessel Beams. Hermann et al. (1991), for instance, proposed to use conical lenses or utilize spherical aberrations.

2.5 A Multi Inverse Bessel Beam Radial Wavefront Sensor

2.5.1 Function Principle of the Slit-mask

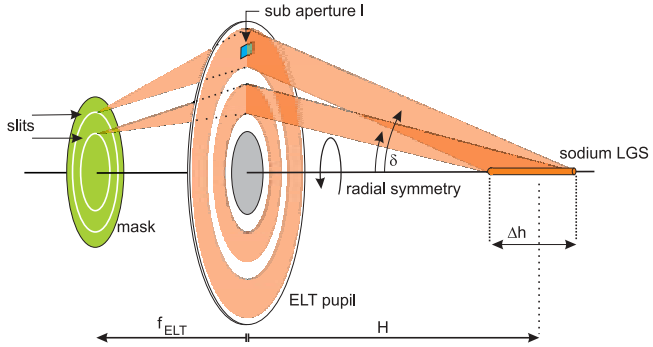

Figure 2.9: A mask with circular silts placed in the focal plane of the telescope selects certain angular directions of light rays originating at a LGS. This approach may be interpreted in analogy to the temporal gating approach as *angular gating*

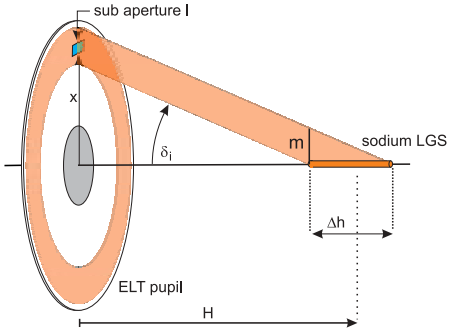

Figure 2.10: Geometrical condition to calculate the projected footprint size m of the LGS onto the telescope pupil

By inverting the setup shown in Figure 2.8 (right), one is able to perform wavefront sensing in the radial direction. According to the geometric optics approximation, fixed positions in the focal plane of a telescope are directly associated to directions of incoming parallel light on the sky. Therefore, a mask with circular concentric thin slits placed in the focal plane will select light rays coming from certain directions δ. This is also valid for rays originating at the LGS, which as a result is projected virtually to infinity by the mask (note: this helps to avoid geometrical effects, but the light does not sample higher layers of the atmosphere, as a true source at infinity like a star does). To deduce how the mask is able to sense an incoming wavefront of a sodium beacon, only light rays are considered which are emitted by the LGS at a defined direction δ_i.

According to Figure 2.9, it is assumed that the sodium LGS takes shape in the mesospheric sodium layer of thickness Δh, located at a distance H from the telescope aperture. Furthermore a sub-aperture l, located at the telescope pupil in distance x from the telescope center, is considered. For the sensing process it is mandatory that the radial size of the sub-aperture has to be much smaller than the projected footprint of the LGS for the selected direction δ_i. This constraint is in the case of OWL (its foreseen central obstruction will have

a diameter of 35% with respect to mirror diameter) fulfilled for any radial position of the sub-aperture, which can be revised by applying geometrical optics considerations (see Figure 2.10). This yields

$$\frac{x}{H - \Delta h/2} = \frac{m}{\Delta h} \tag{2.5}$$

an equation for m, which denotes the absolute vertical extent of the LGS footprint at the pupil. A lower limit for m is given in the case of a sub-aperture close to the edge of the central obstruction ($x = 17.5$m). At this point the projected footprint is still 1.6m and thus significantly larger than a typical sub-aperture size l (l normally is on the order of r_0, which translates into 20cm in the H-band).

For simplification reasons it is assumed in the following that distances between two circular slits in the focal plane have been selected such that no overlap of two successive footprints in the pupil plane occurs. In practice this means: Each sub-aperture is exclusively illuminated by light from one direction δ_i. But it is important to realize that in principle the light throughput can be increased by illuminating each sub-aperture with rays from several directions. This approach leads to a new gating concept called *angular gating* (see Figure 2.15 and section 2.5.3). Hence, in the aberration free case, the sub-aperture l will be illuminated by light of the LGS coming from portion s (see Figure 2.11). Introducing a wavefront distortion close to the telescope pupil, the amount of light from the LGS projected into the sub-aperture does change with the amplitude of the atmospheric phase aberration at the edges of the sub-aperture.

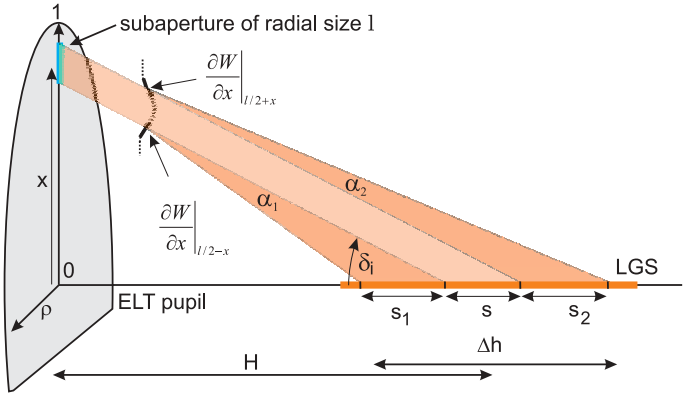

Figure 2.11: A radial wavefront error at the edge of the sub-aperture is related to a change of the "effective" beacon length illuminating the sub-aperture. Details see text.

A wavefront error with positive curvature within the sub-aperture leads to an additional

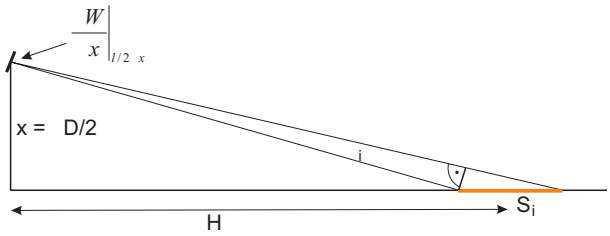

Figure 2.12: Geometrical situation to connect the radial wavefront error slope $\frac{\partial W(\rho,\theta)}{\partial x}$ at the edge of the sub-aperture with the resulting maximum differential α_i.

amount of light refracted into the sub-aperture. Such rays are originating at additional portions s_i of the LGS and are associated with different directions than δ_i. Thus, the intensity within the sub-aperture is proportional to the "effective" length $s + s_1 + s_2$ of the beacon contributing to its illumination. By defining I and I' as brightness within the sub-aperture in the non-aberrated and aberrated case, respectively, one can describe the resulting normalized brightness fluctuation as:

$$\frac{I' - I}{I} = \frac{\Delta I}{I} \propto \frac{\Delta s}{s} = \frac{s_1 + s_2}{s} \tag{2.6}$$

While s is the reference beacon length for the non-aberrated case, $\Delta s = s_1 + s_2$ denotes the net change of the beacon length introduced by the radial distortion. Depending on the curvature radius, this may lead to positive or negative values for Δs and determines thus the strength of the intensity fluctuation within the sub-aperture. The maximum differential angle of a ray originating at the LGS, which will still be refracted into the sub-aperture, is related to s_i via (see Figure 2.11):

$$s_i = H \cdot \frac{2 \cdot H}{\varrho \cdot D} \cdot \alpha_i \qquad\qquad i = 1, 2 \tag{2.7}$$

Here ϱ denotes the normalized radial pupil coordinate and is connected to the radial distance x from the center of the pupil via:

$$x = \varrho D/2 \tag{2.8}$$

The portion s in the non-aberrated case is given by:

$$s = l \cdot \frac{2 \cdot H}{\varrho \cdot D} \tag{2.9}$$

In order to compute the ratio $\Delta I/I$, equations 2.7 and 2.9 are combined with equation 2.6:

$$\frac{\Delta I}{I} = \frac{H}{l} \cdot (\alpha_1 - \alpha_2) \tag{2.10}$$

According to Figure 2.12, the angle α_i is proportional to the radial wavefront slope at the edge of the sub-aperture. Therefore the difference $\alpha_1 - \alpha_2$ can be written as

$$\alpha_1 - \alpha_2 = \frac{\partial W(\rho, \theta)}{\partial x}\bigg|_{x-l/2} - \frac{\partial W(\rho, \theta)}{\partial x}\bigg|_{x+l/2} \approx \frac{\partial^2 W(\rho, \theta)}{\partial x^2} \cdot l \tag{2.11}$$

leading to the second radial derivative. Moreover x has to be transformed into the normalized pupil coordinate ρ. This is done by calculating the square of the derivative $\partial x/\partial \rho$ of equation 2.8, which leads to an additional factor $4/D^2$:

$$\alpha_1 - \alpha_2 = \frac{\partial^2 W(\rho, \theta)}{\partial \rho^2} \cdot \frac{4}{D^2} \cdot l \tag{2.12}$$

By combining ultimately equations 2.12 and 2.10, one obtains a relation which describes the dependency of the normalized intensity fluctuation within the sub-aperture on the second radial derivative of the phase error of the wavefront:

$$\frac{\Delta I}{I} = \frac{4H}{D^2} \cdot \frac{\partial^2 W(\rho, \theta)}{\partial \varrho^2} \tag{2.13}$$

It has to be pointed out that the gain $4H/D^2$ of the mask does not depend on the sub-aperture size l.

2.5.2 Defining and Controlling the Sub-aperture Size

Still an open question is how to control the sub-aperture size, which determines the sampling of the wavefront error. The radial mask placed in the focal plane influences – depending on the phase aberrations – the intensity distribution in the pupil plane as measured by a pupil plane WFS. The sampling grid and therefore the sub-aperture size can be adjusted by the used pixel grid of the CCD (see Figure 2.24). This may be a major advantage, since due to its flexibility the system can easily be adjusted to varying atmospherical conditions.

2.5.3 Efficiency Estimates

Constraining the Slit-width

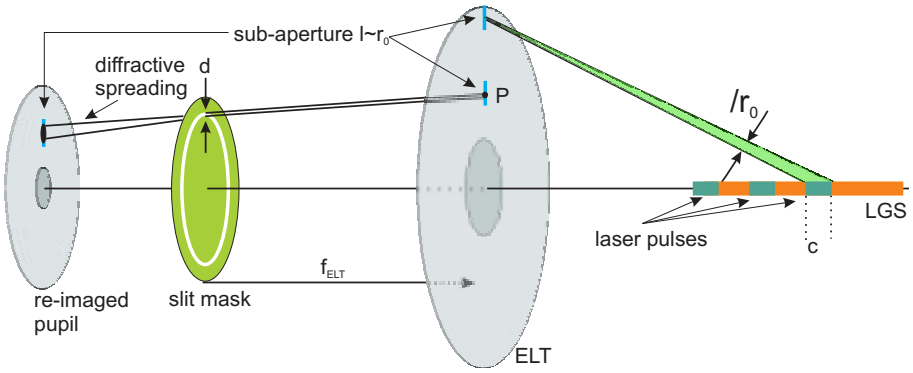

Figure 2.13: Efficiency comparison of slit mask with temporal gating approach: Temporal gating has to constrain the angular elongation of the LGS to the order of the seeing λ/r_0. Simultaneously a lower limit for the slit width can be determined considering diffraction effects. It can be shown that the light throughput per slit is as high as in the case of temporal gating (details see text).

The mask rejects most of the incoming light of the LGS, at first glance resulting in an inefficient usage of the available photons as in the temporal gating approach (all blocked photons can not contribute to the recorded signal). In this section both concepts will be compared in a quantitative way and it will be shown that the mask (and hence angular gating) is in terms of light efficiency superior to temporal gating. Unsolved technical issues of temporal gating (see section 2.1) are neglected, and it is assumed that the pulse frequency of the laser can be made arbitrarily high. For a sub-aperture at the edge of the telescope the apparent spot elongation depends on the length of the excited column and hence in the case of temporal gating on the pulse duration τ (indicated in Figure 2.13 with the dashed line). As long as the angular elongation is of the order of the seeing (λ/r_0), the performance of a conventional WFS will not be affected (assume for instance a SHS operated in the V-band with a sub-aperture size of the order of r_0, where each lens produces a seeing limited image of the guide star on the CCD). Therefore this constraint defines an upper limit for the effectively used beacon length for the temporal gating and hence implicitly the amount of available light.

A lower limit for the slit width of the mask can be estimated by diffraction optics considerations. In this case the pupil re-imaging optics views a sub-aperture at the pupil through a thin slit of width d. Hence waves originating from each point P at the pupil have to pass the slit, which leads to diffractive spreading (see Figure 2.13). This results finally in a smoothing

of each single point. In order to minimize cross-talk, the induced radial smoothing of points of a sub-aperture has to be smaller than the sub-aperture size l, which is normally adjusted to the coherence length r_0. To estimate this effect quantitatively it is assumed that each point viewed through the slit leads to a PSF, whose FWHM in the radial direction is given by λ/d. Hence one may write

$$\frac{\lambda}{d} \leq l = r_0 \tag{2.14}$$

Solving equation 2.14 for the slit width d yields:

$$\frac{\lambda}{r_0} \leq d \tag{2.15}$$

This means: The minimum possible angular slit width in the infinity focal plane has to be of the order of the seeing. Thus the same amount of light will pass through *each slit* and enter the optical system, as in the temporal gating approach. Hence the light throughput will be identical.

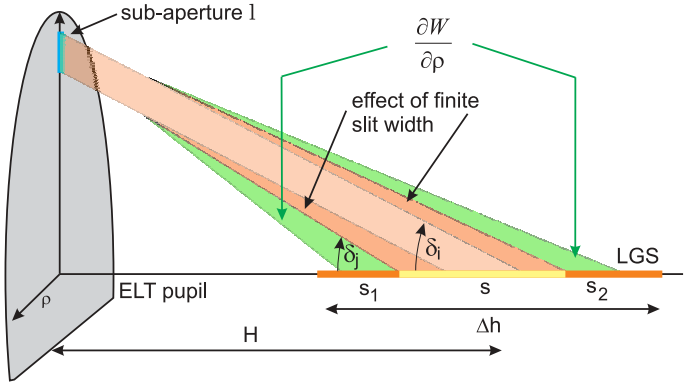

Figure 2.14: Consequence of broadening the slit width. Although on the one hand a gain in terms of light-throughput can be achieved, on the other hand this approach leads to a loss of dynamic range and thus sensitivity of the mask.

To increase the throughput, one can in the first instance think about broadening the slit width. This, however, is connected with a loss of dynamic range of the sensor. A finite slit width is coupled with an additional amount of light illuminating the sub-aperture l. It originates from directions up to δ_j (see Figure 2.14), adjacent to direction δ_i, increasing the reference beacon length s and thus the reference intensity I. On the other hand, a given wavefront distortion will result in a fixed change of the beacon length s_i or intensity I'. For this reason the measurable net change in intensity fluctuation (= dynamic range) for a fixed wavefront distortion will decrease with increasing slit width. This has a drawback on the sensitivity of the slit mask sensing device.

Minimum Slit Distance and Multiple Gating

The light selection process of the mask can be seen in analogy to the temporal gating as *angular gating*. But, unlike for temporal gating, the light throughput per sub-aperture can easily be increased performing multiple gating with multiple slits. Each sub-aperture is illuminated by light from several directions (See Figure 2.15), which translates simply into an increased number of concentric slits. To estimate how many different directions per sub-aperture can be used for angular gating, it is mandatory to figure out the necessary minimum distance

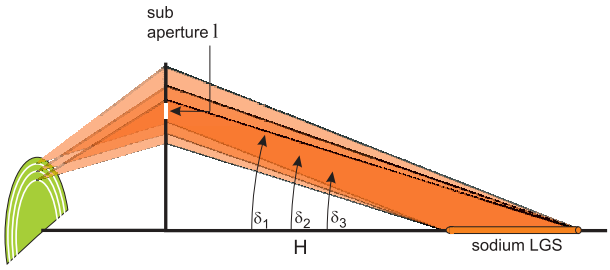

Figure 2.15: To increase the light throughput, a sub-aperture can be simultaneously illuminated by light from several directions (*angular gating*). Depending on the radial position this leads to 4-10 times more light throughput in comparison to temporal gating.

between two successive slits. The latter is constraint, since the mask - in order to perform the sensing - has to block light within a certain differential angle (given by the expected radial wavefront distortion) around the reference direction δ_i. Otherwise, aberrated light rays which have to be blocked enter the optical system through an adjacent slit and contribute nevertheless to the intensity distribution recorded by the detector. The minimum separation between two angularly gated directions δ_i and δ_k therefore has to fulfill the condition (see Figure 2.16):

$$\frac{\partial W(\rho,\theta)}{\partial \rho} < \delta_i - \delta_k \tag{2.16}$$

where $\frac{\partial W(\rho,\theta)}{\partial \rho}$ denotes the maximum radial wavefront slope which still has to be blocked. A upper limit for $\frac{\partial W(\rho,\theta)}{\partial \rho}$ at the edge of a sub-aperture l may be retrieved directly from the definition of r_0. The wavefront RMS phase error encircled by r_0 is $1\,rad = \lambda/2\pi$. The corresponding Peak To Valley (PTV) phase fluctuations is given by deducing the typical PTV/RMS ratio. As a rule of thumb a factor 6 is used (this value can be determined by averaging the PTV/RMS ratio for a series of Zernike modes, which are used to compose the wavefront fluctuation within r_0). Therefore λ is a typical upper limit for a PTV wavefront error within the sub-aperture $l = r_0$. This finally translates into a maximum slope of the radial wavefront error $\frac{\partial W(\rho,\theta)}{\partial \rho}$ of λ/r_0. As a result, the angular distance μ between two successive slits has to be at least on the order of the seeing ($\mu \geq \lambda/r_0$).

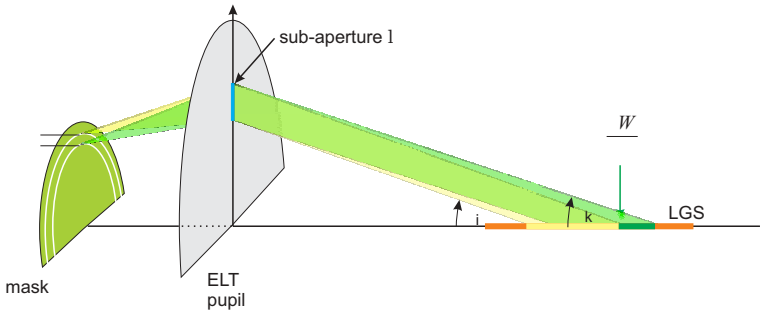

Figure 2.16: A condition for the minimum angular slit distance μ can be retrieved assuming that two gating directions δ_i and δ_k have to be at least separated by the expected slope of the radial wavefront error $\frac{\partial W(\rho,\theta)}{\partial \rho}$ at the edge of a sub-aperture.

Finally, one can derive an expression to estimate the gain of multiple angular gating with respect to temporal gating. Therefore a sub-aperture l is considered (see Figure 2.17), which is

located at distance $\rho D/2$ from the center of the pupil. Again ρ denotes the normalized radial pupil coordinate and D the telescope diameter. The sub-aperture will only be illuminated by light rays originating from a cone of directions located between δ_1 to δ_2, since for these directions the projected footprints of the LGS cover the sub-aperture. Using the geometrical optics approximation, M slits in the focal plane will cover an angle $M\mu$, which is exactly the differential angle $\delta_2 - \delta_1$. M denotes a multiplicity factor describing how many slits can be used for angular gating. A relation to compute M can be deduced by realizing that the length of the absolute radial size of the LGS footprint at the pupil from direction δ_1 and the absolute length of the differential angle $M\mu$ at the pupil are equal (see Figure (2.17)):

$$\frac{\Delta h \rho D}{2H} = M\mu H \tag{2.17}$$

solving now the upper equation for M yields:

$$M = \frac{\Delta h \rho D}{2\mu H^2} \tag{2.18}$$

According to equation 2.18, the multiplicity factor M is a function of the radial position ρ of the sub-aperture and moreover sensitive to the choice of the slit distance μ. Inserting typical numbers as for instance in the case of OWL ($D = 100$m, $\mu = 1$", $H = 100\ km$, $\Delta h = 10\ km$) one obtains $M \approx 10\rho$. The planned diameter of the central obstruction of OWL constrains ρ to range from 0.35 to 1. Thus the light throughput of the slit mask and therefore angular gating is at least a factor of 3.5 more efficient as temporal gating. The efficiency will benefit further from good seeing conditions, since the minimum slit-distance and slit width may be reduced.

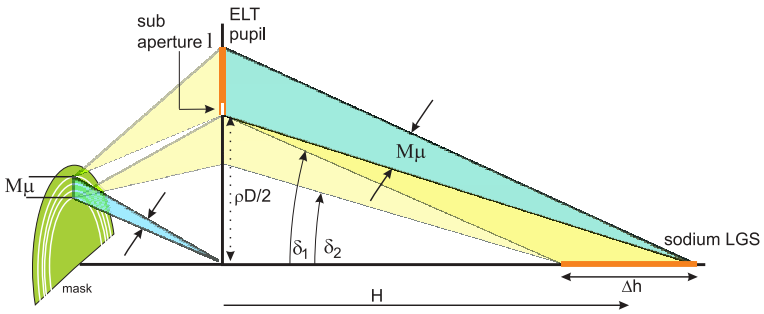

Figure 2.17: The achievable multiplicity factor M for multiple angular gating, and therefore the resulting gain in terms of light throughput, can be deduced following geometric optics considerations. The radial elongation of the angle $M\mu$ at the pupil is equivalent to the projected footprint of the LGS for the direction δ_1.

2.5.4 Physical Extent of the Mask and Size Limitations

In the case of OWL, the physical diameter of the slit mask will have to be 0.54m (assuming a F/6 optical design for OWL, which leads to a focal length of 600m). An angular separation $\mu = 1$" of two successive slits corresponds to a physical extent of ~ 2.9mm in the focal plane. Assuming equidistant slits and a central obstruction of $\varepsilon = 0.35$, the mask can be equipped with 38 slits with a width of 2.9mm. Imposed by the radial dependency of the angular gating, a choice of equidistant slits, however, would lead to a radial brightness gradient within the

re-imaged pupil. Therefore a solution may be preferred where a constant gain in terms of light throughput over the pupil is guaranteed. This would correspond to a slit distance following a ρ^{-1} law.

As a major limitation, the circular slit mask is, due to its radially symmetric design, only able to perform sensing in radial directions. In principle it is possible to extend the sensing capability of the mask and retrieve information about the entire wavefront phase error. One solution would be to introduce a grid of further blocking elements per slit in the azimuthal direction (on the order of the seeing). This approach is connected to a further loss of light and leads to an increasing inefficiency in terms of light throughput.

2.6 Azimuthal Sensing with a z-invariant Wavefront Sensor

2.6.1 Sensing Concept

To obtain information about the azimuthal phase aberration of an incoming wavefront, the use of a second independently working sensing device is proposed, based on a concept presented by Ragazzoni et al. (2001). As sensing device a reflective rod is placed in the image space of the telescope optics conjugated to the laser beacon. This section gives a brief summary

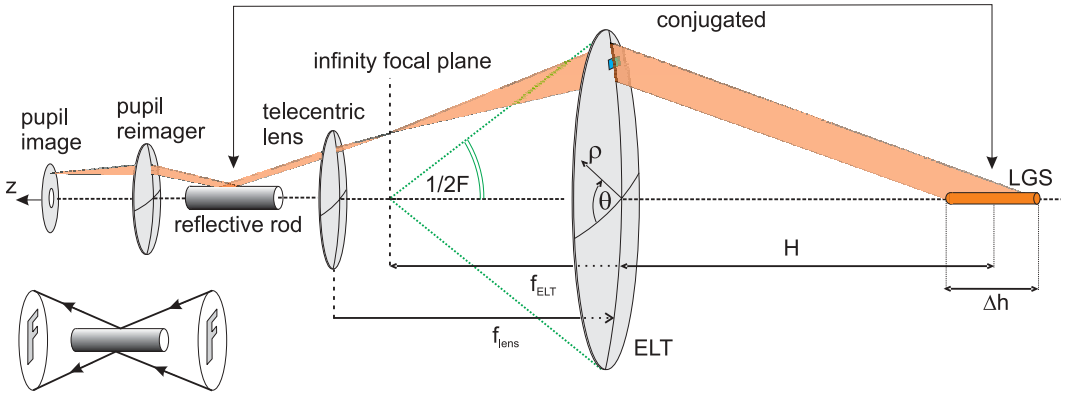

Figure 2.18: Concept of z-invariant wavefront sensing. A reflective rod as z-invariant 3d sensing device is conjugated to the LGS in the image space. It matches in a natural way the introduced geometry of the extended light source. The rod "sees" the pupil via a telecentric optic, eliminating projection effects. **Lower left:** Due to the reflection of rays at the rod surface, the pupil image becomes rotated by 180°.

on the capabilities of the reflective rod as a 3-dimensional z-invariant azimuthal wavefront sensing device. For simplicity, it is assumed that the pupil plane, as seen from the rod, is located at infinity. Therefore, a telecentric optic is introduced into the optical path prior the rod (see Figure 2.18). A single ray originating at a certain altitude of the LGS (see Figure 2.19) will pass the telescope pupil and will be focussed at the conjugated point P located at the surface of the rod of radius r. Since the projection of the ray trajectory is normal to the rod surface, the reflected ray will not be deflected in the azimuthal direction. In the case of an azimuthal wavefront distortion, the ray will leave the pupil with a slope according to the introduced azimuthal wavefront error $\partial W(\rho,\theta)/\partial\theta$. This translates for a telecentric system into a parallel shift b proportional to $\partial W(\rho,\theta)/\partial\theta$, which can be written as:

$$b = \frac{2F}{\rho}\frac{\partial W(\rho,\theta)}{\partial\theta} \tag{2.19}$$

Obviously, b depends on the focal ratio $F = f/D$ of the telescope and a normalized weighting factor ρ^{-1}, determined by the radial position where the ray leaves the pupil. As a result of the shift, the aberrated ray will hit the rod surface not normal and suffers a deflection in the θ-direction. Due to the z-invariance of the sensor this assumption is also true for all rays

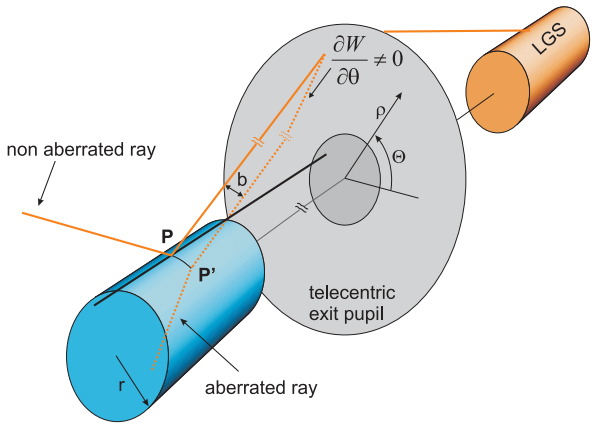

Figure 2.19: Azimuthal wavefront sensing with a reflective rod: While a non-aberrated ray will be reflected by the rod normal to the rod surface, this condition is not valid for a ray aberrated in the azimuthal direction, which will be deflected in the azimuthal direction.

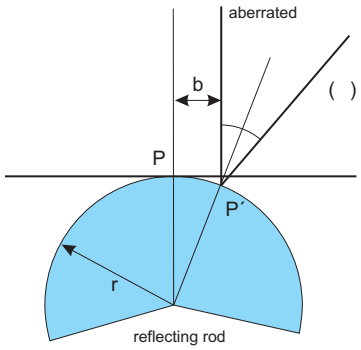

Figure 2.20: Impact of an azimuthal aberration $\frac{\partial W(\rho,\theta)}{\partial \theta}$: Stigmatic and aberrated rays, coming from the same point on the infinitely distant exit pupil, are parallel. The aberrated ray will be shifted by b, which leads to a deflection of $\beta(\theta)$.

passing the same point at the pupil but coming from different heights of the beacon. In the case of an aberration associated to a non–zero derivative with respect to the azimuth angle θ, the ray hits the rod at P' displaced from P by an amount b, and is deflected at an angle β given by (see Figure 2.20):

$$\beta \approx \frac{2b}{r} \tag{2.20}$$

where $b \ll r$ is assumed. Combining equation 2.19 and equation 2.20 yields:

$$\beta \approx \frac{4F}{\rho r}\frac{\partial W(\rho,\theta)}{\partial \theta} \tag{2.21}$$

To describe the resulting intensity modulation at the exit pupil image, one has to consider two rays coming from points (ρ,θ) and $(\rho,\theta+d\theta)$ at the edge of one sub-aperture. Due to the reflection process and depending on the local azimuthal distortion, θ will be mapped to $\theta+\pi+\beta(\theta)$ and $\theta+d\theta$ to $\theta+d\theta+\pi+\beta(\theta+d\theta)$ (see Figure 2.21); the angular separation between the reflected rays is then given by

$$d\theta' = d\theta + \beta(\theta+d\theta) - \beta(\theta)\,. \tag{2.22}$$

Expanding $\beta(\theta+d\theta)$ to first order according to equation 2.21 gives:

$$d\theta' \approx d\theta + \frac{4F}{\rho r}\frac{\partial^2 W}{\partial^2 \theta}d\theta \tag{2.23}$$

The transformation $d\theta \rightarrow d\theta'$ is associated with a modification of the ray density on the exit pupil image. As a consequence, the modulated intensity ratio $\Delta I/I$ can be written as

$$\frac{\Delta I}{I} \approx \frac{4F}{\rho r}\frac{\partial^2 W}{\partial \theta^2} \tag{2.24}$$

Here I denotes the illumination within a sub-aperture in the non-aberrated case, while ΔI is the change in intensity, induced by the aberration.

In conclusion: The z-invariant WFS is, as its radial counterpart, sensitive to the second derivative of wavefront phase aberrations, but with respect to the azimuthal coordinate. The sensitivity is inversely proportional to the radius of the reflective rod such that the rod WFS can be adjusted to a desired sensitivity by varying its radius. This makes the sensor particulary flexible for the combination with other devices such as the slit mask, the sensitivity of which is fixed.

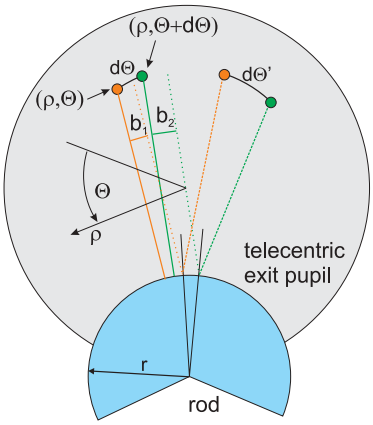

Figure 2.21: Resulting intensity modulation on the re-imaged pupil in the case of non-zero azimuthal wavefront curvature: Two aberrated rays of distance $d\theta$ (dotted lines) at both edges of an azimuthal sub-aperture are considered. Both will be mapped at points, whose relative distance $d\theta'$ depends on their local wavefront error. This transformation is associated to a modification of the ray density on the image of the exit pupil, leading to a modulation of the signal.

2.6.2 Constraints on the Rod Sensing Device

Effects of the rod on pupil re-imaging

According to equation 2.24 a decrease of the rod diameter leads to an increase of the sensitivity of the WFS. This is, however, associated with a loss of sampling capability. As depicted in Figure 2.22 and Figure 2.23, in reality the LGS has a finite lateral width on-sky and will therefore exhibit a finite physical size u perpendicular along the optical axis in the image space, when imaged by the telescope optics. Due to the curved shape of the rod-surface this leads to a characteristic spreading after the reflection, visible at the re-imaged pupil. As a result, each point of the pupil will be re-imaged to an arc of angular extent α. This angular extent has to be constraint to be within one sub-aperture in order to minimize crosstalk between two adjacent azimuthal sub-apertures. In this way, the desired sampling accuracy defines a lower limit for the rod radius. The impact on the FWHM of the resulting arc can be estimated following Figure 2.22, which showns that α is given by $2u/r$.

These considerations can be adopted in the framework of ELTs. Assuming that the lateral angular spot size of the LGS does not exceed the size of the seeing λ/r_0 and taking into account that an ELT transforms angles in object space depending on its total focal length

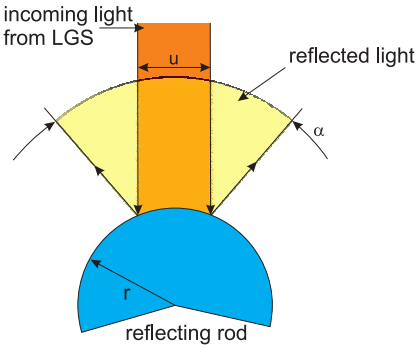

Figure 2.22: Due to its finite angular extent, a LGS will be imaged by the telescope to a defined lateral size u. This leads, caused by the curved surface of the rod, after the reflection process to a spreading α

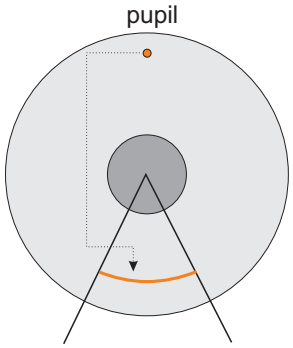

Figure 2.23: As a result of the imaged finite lateral spot size of the LGS, the rod transforms each point at the re-imaged pupil into an arc of angular extent α.

f_{ELT}, one obtains an angular spreading α depending on the rod radius r of:

$$\alpha \approx \frac{\lambda f_{ELT}}{r r_0} \tag{2.25}$$

Solving equation 2.25 for r defines a lower limit for the rod radius in the case of an ELT. For OWL (according to the actual design $f_{ELT} = 600$ m) the necessary minimum rod radius is of the order of 8.3 cm (to obtain at least 180 distinguishable azimuthal sub-apertures).

Rod Length and Rod Position

Rod-length and rod position are in principle determined by the conjugated altitude and vertical extent of the sodium layer in the object space. However, these quantities depend on several seasonally changing parameters and thus may vary strongly. As a result, not only the necessary rod length, but also the absolute position of the rod in the image plane can vary. A detailed knowledge about the structure and parameters of the sodium layer can be retrieved by different measurement techniques like LIDAR (Butler et al. (2002)), where in addition to the altitude and thickness of the sodium layer also its density as a function of height can be recorded. A changing altitude of the sodium layer may require a huge accuracy and mobility of the opto-mechanical components. This is even more the case, since rod position and required rod length are a function of the zenith viewing angle. Finally, absolute rod position and length depend strongly on the chosen rod radius. This has to be considered for a practical optical sensor layout and is intensively discussed in section 4.3.2.

2.7 Combining the Signals - The Pseudo Infinite Guide Star WFS

In order to recover the full information about the atmospherically induced phase error of an incoming wavefront, the Inverse Bessel Beam (IBB) and z-invariant sensing concept have to be combined. This can be done in a straightforward way as both sensing devices do not interfere, since they perform the sensing process at physically separated planes (the mask in the infinity focal plane and the rod in the LGS focus.). This results in a pupil plane wavefront sensor measuring the second derivative of an incoming wavefront as is the case for a curvature

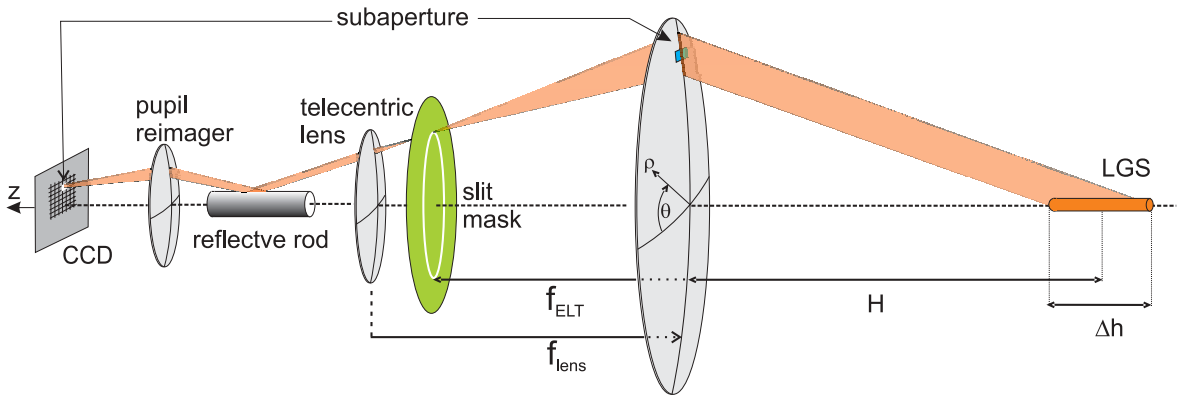

Figure 2.24: Layout of the PIGS wavefront sensor. A LGS illuminates the telescope aperture of an Extremely Large Telescope. The mask with circular slit acting as radial wave front sensor is placed in the infinity focus. The reflective rod as azimuthal sensor is separated from the pupil by a telecentric lens and positioned in the image of the LGS. A re-imaging optics is used to image the pupil onto a CCD-detector.

WFS. The complete sensor is named Pseudo Infinite Guide Star Sensor (PIGS) (note: for the rod not the sodium LGS but the corresponding pupil plane is projected to infinity). Figure 2.24 depicts a sketch of a possible practical layout. A LGS in the sodium layer is excited at altitude H having a vertical extent Δh. It illuminates a telescope with F-ratio of f_{ELT}/D. The slit-mask is placed at the infinity focal plane of the telescope performing the radial sensing. The rod is separated from the pupil by a telecentric lens with focal length f_{lens} and positioned where the image of the LGS is formed. This setup guarantees conditions for each device as described in section 2.5 and 2.6. The pupil is re-imaged by a relay lens onto a CCD-detector, whose resolution defines the sub-aperture size. Since both sensors act completely independent, the resulting total intensity fluctuation is composed by adding both signals in a linear way:

$$\frac{\Delta I}{I} \propto \left(A\frac{\partial^2 W}{\partial \varrho^2} + B\frac{\partial^2 W}{\partial \theta^2} \right) \tag{2.26}$$

Here $A = \frac{4H}{D^2}$ and $B = \frac{4F}{\rho r}$ denote the expected sensitivty for each component (see equations 2.13 and 2.24). A proper balancing of both means:

$$A \approx B \Rightarrow \frac{4H}{D^2} \approx \frac{4F}{\rho r} \tag{2.27}$$

Investigating equation 2.27, this can be achieved by adjusting the rod radius r and/or the F-ratio F to the diameter D .

2.8 PIGS in MCAO

Up to now a practical implementation of the PIGS sensor was introduced for a conventional single conjugated AO system. Such a solution, however, is in the case of ELTs inapplicable due to the resulting low sky-coverage, and therefore a MCAO-approach is favored. The PIGS sensor offers great flexibility and can easily be inserted in a MCAO environment. Moreover - due to its pupil plane WFS design - it is practicable for both common MCAO approaches, the layer and the star oriented system. Figure 2.25 and Figure 2.26 sketch a possible solution for the PIGS sensor implemented in both layer-oriented and star-oriented system. To enhance differences between these sensing concepts, only on-axis rays from infinity and the LGS are

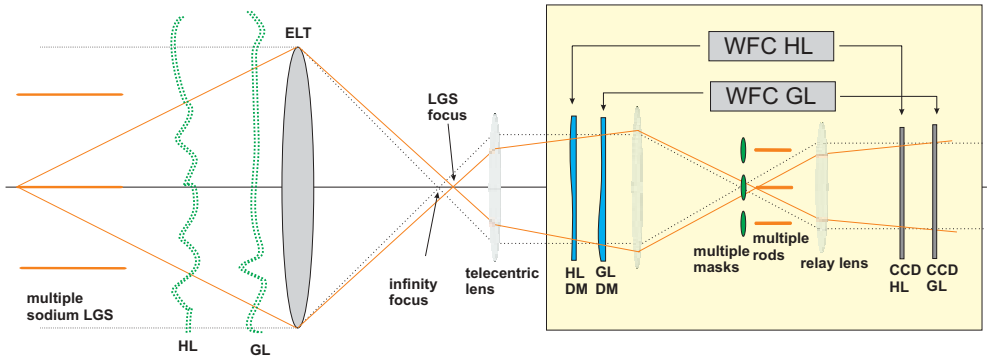

Figure 2.25: The PIGS sensor in a telecentric layer-oriented MCAO setup (yellow box). Each PIGS sensor is conjugated to one sodium LGS, respectively. A relay lens is imaging Ground Layer (GL) and High Layer (HL) turbulence to separate WFS-CCDs. For clarity, only rays for the on-axis guide star are included.

indicated. In both cases, one PIGS sensor (mask and rod) is conjugated to a single sodium LGS. In the layer-oriented solution, light from each guide star will be optically co-added. It is imaged by means of a relay lens to the WFSs, which are conjugated to a certain height (high layer and ground layer) measuring in this way directly the induced distortion of this layer. Hence each DM can be driven via independently operated control loops. In the star-oriented

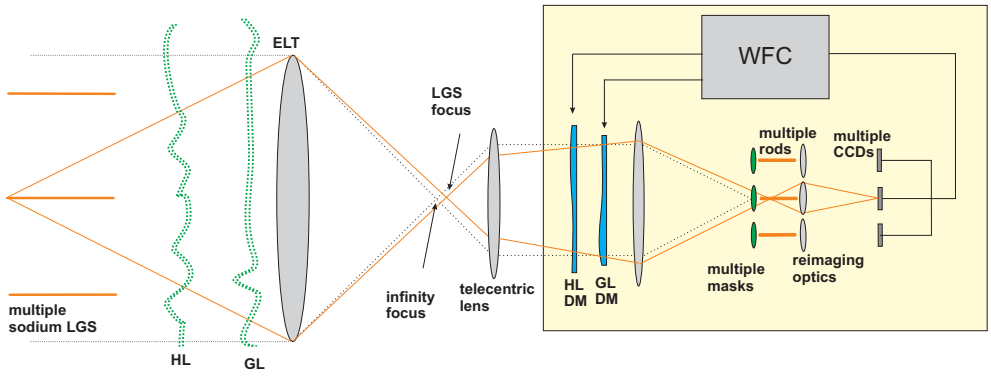

Figure 2.26: The PIGS sensor in a telecentric star-oriented MCAO approach (yellow box). Like in the layer-oriented technique, each PIGS sensor is conjugated to one sodium LGS, respectively. However, information about the wavefront error from each guide star is recorded in separate WFS. All information is pipelined and processed in a single control loop, operating the DMs, conjugated to the desired heights.

case the light of each LGS will be sensed by one mask-rod system and re-imaged to separate CCDs, each measuring the induced distortion over the line of sight with respect to the guide star. Information about turbulence layers is implicitly conserved, but has to be disentangled from the data by a suitable wavefront computer (WFC) to drive the DM.

Chapter 3

Laboratory Verification of the z-invariant Sensor

The last chapter introduced the Inverse Bessel Beam (IBB) and z-invariant concepts as novel wavefront sensing techniques. It has been demonstrated that both ideas can be merged to a wavefront sensing device, optimized for LGS-based (MC)AO facilities at ELTs. This approach would overcome several problems linked to the finite distance and vertical extent of the sodium beacon. As a further part of this thesis and main scope of this chapter, the z-invariant concept was studied in the laboratory for its feasibility and limitations. The chapter deals with questions such as how to estimate important parameters like azimuthal sub-aperture size and effects induced through warping due to misalignment. Moreover, an adequate alignment procedure for the reflective rod is introduced, and a detailed description of the data reduction approach is presented. The final section of this chapter addresses why the testing and verification of the slit mask sensor hardly can be accomplished under laboratory conditions.

3.1 Principal Setup

The z-invariant concept is a wavefront sensing technique proposed especially with the view on ELTs. Therefore a reliable and convincing laboratory verification of the z-invariant method can be achieved by modelling a down-scaled ELT. However, a proper dimensioning to numbers manageable in the laboratory simulating similar geometrical conditions as for an ELT, leads to stiff demands on the optical setup. The scaling factor in the case of OWL could be e.g. 1000. The diameter of $\sim$ 100m would translate into a lens of an aperture diameter of 100mm. Simultaneously the distance of the LGS with respect to the telescope ($\sim$ 100km) and the vertical extent of the laser beacon in the mesosphere ($\sim$ 10km), corresponds to a light source placed in a distance of 100m with respect to the focussing optics, characterized by a lateral extent of 10m along the optical axis. An optical setup fulfilling such a specification could be realized by means of an optic shifting the light source virtually to the desired distance (see section 3.7 and Figure 3.20).

Section 2.6 states that the sensitivity of the reflective rod is neither affected by the relative distance of the light source and the telescope nor the vertical extent of the light source on sky. In addition, the main goal of this laboratory experiment was to sense a strongly extended light source by means of the rod.

To guarantee a sufficient extent in the image space, the light source was finally placed at

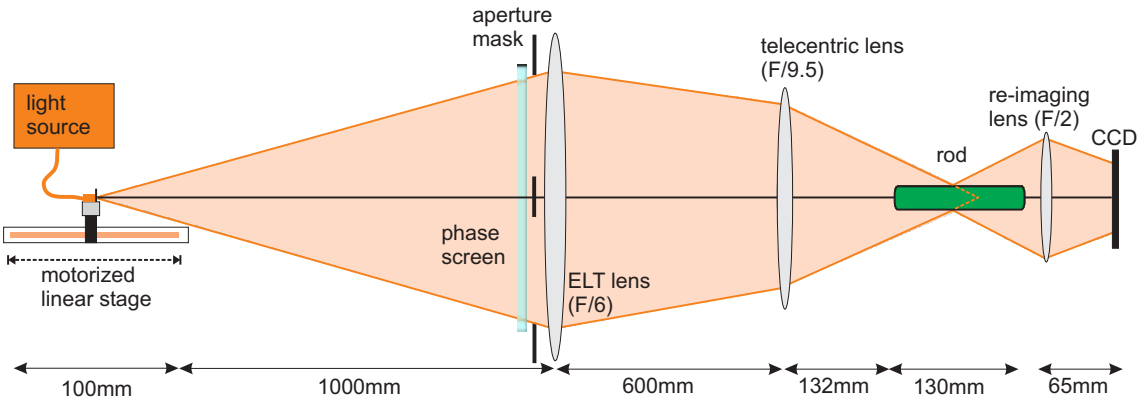

Figure 3.1: Sketch of lab setup. A light source mounted on a motorized linear stage is simulating an extended LGS. A phase screen to emulate atmospherically induced wavefront phase errors was mounted in front of a lens, whose aperture was constraint by a stop. A second lens creates a telecentric beam as seen from the reflective rod serving as sensing device. The rod is placed in the image position of the light source. The pupil is re-imaged by means of a lens onto a CCD

a distance of 1000mm with an overall extent of 100mm (scaling its properties by 1:10000). In this way the ratio of LGS-altitude and its vertical extent on the sky is conserved. The complete laboratory setup is depicted in Figure 3.1. According to their functions, the setup can be split up into three main components, namely:

- A LGS simulating unit to emulate an extended light source
- An atmosphere and telescope unit, which mimics atmospherical induced wavefront perturbation and the focussing optics of an ELT with central obscuration.
- A sensing and pupil re-imaging unit.

3.1.1 LGS Simulator Unit

To create the extended light source a flexible light guide coupled to a white light source has been mounted on a motorized linear translation stage. The stage in principle offers a maximum travelling range of 150mm and can be positioned with an accuracy of 0.1μm. It was controlled from a PC via a serial interface and has been operated by a set of ASCII-commands. To control and run the stage under a Windows-IDL environment, a dynamical shared windows library (.dll) embedded into IDL has been developed. The library offers a basic set of commands to move the stage. To control the angular extent of the light source, a plate with a hole of a diameter of 0.5mm has been placed in front of the light guide. The optimum hole-diameter was found by reference measurement done before. This process is in more detail described in section 3.3. A piece of paper glued on the plate served as diffusor. The complete opto-mechanical construction of the LGS-simulator is depicted in Figure 3.2.

3.1.2 Atmosphere and Telescope Unit

The atmosphere and telescope unit (see Figure 3.3) has been composed of an F/6 (d=100mm) lens. A telescope aperture stop with a central obstruction has been built to simulate the telescope. The stop constrained the overall aperture diameter to 80mm (this is equivalent to

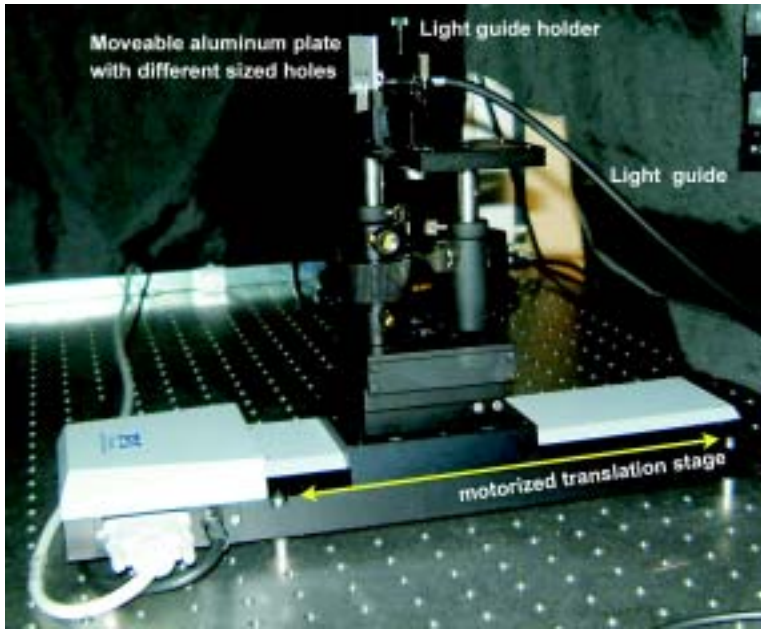

Figure 3.2: To emulate a laterally extended light source, the LGS simulator consists of a flexible light guide, which has been mounted on a motorized linear translation stage. The light guide was connected to a white light source. The angular spot size has been constraint by a hole, drilled in an aluminum plate. To guarantee diffuse light, a piece of paper was glued on the plate.

an 80m ELT). It introduced moreover a central circular obstruction of relative size $\epsilon = 0.35$. The obstruction was held in place by a configuration of four orthogonal 10mm thick spiders (see Figure 3.6), which were used for alignment purposes. By mounting a plate holder in front of the aperture stop, phase-screens (simulating ground-layer turbulence) can be introduced into the light cone coming from the LGS-simulator.

3.1.3 Sensing and Imaging Unit

The sensing and imaging unit consists of a F/9.5 (d=63mm) lens, displaced from the pupil plane at a distance of its focal length. This ensures a telecentric configuration. Hence, the pupil is shifted to infinity and rays from a defined point at the pupil enter the optical system as if originating from a certain direction. The reflective rod as sensing device is aligned to the optical axis at the image position of the LGS produced by the preceding optical components. To determine correctly the overall length and position of the rod one also has to consider the impact of its finite thickness on the imaging characteristics. This leads to a change in the absolute image position and length. A detailed treatment of this problem can be found in section 4.3.2 with the further description of the on-sky experiment at the WHT. The pupil has been re-imaged by a camera composed of a F/2 (d=25mm) lens and an EDC-2000 CCD (see Figure 3.4).

Figure 3.3: Atmosphere and telescope simulator. From left to right: phase screen, aperture stop and ELT-lens.

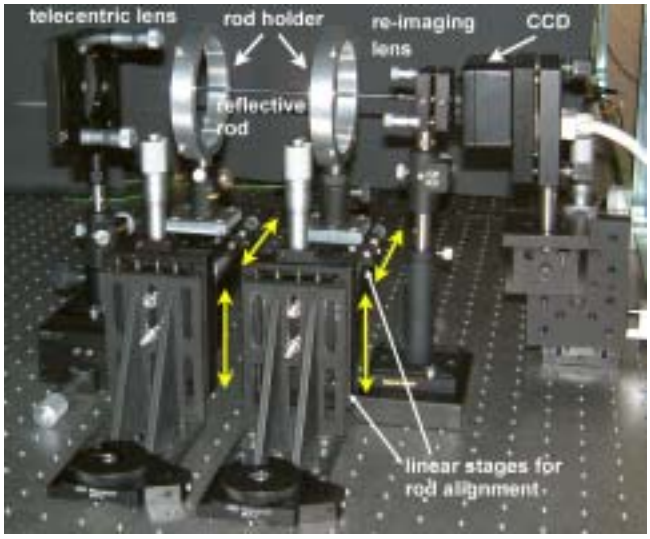

Figure 3.4: Sensing and imaging unit. From left to right: Telecentric lens, rod embedded into rod-holder, pupil re-imaging lens and CCD.

3.2 Rod Peculiarities

3.2.1 Rod Composition and Rod Opto-mechanical Issues

As substrate for the sensing device a commercially available glass-stirrer was used. Although this unconventional approach introduces non negligible static aberrations, it turned out that these can be calibrated sufficiently by the z-invariant reference measurements. A suitable diameter of the rod was estimated according to section 2.6.2, which yield 4mm. Based on the lateral extent of the light source along the optical axis in the image space and taking into account the finite thickness of the rod, a total rod-length of 130mm was required. Finally, to achieve a high grade of reflectivity, the glass-substrate was aluminized.

To perform precise measurements, the reflective rod has to be accurately aligned along the optical axis of the optical setup. Taking into account its 3-d design this is necessary, since already a small misalignment of the order of several 1/10mm between rod-axis and optical axis imposes non negligible warping effects on the re-imaged pupil. A proper adjustment of a rotationally-symmetric, extended object in 3-d space along a defined axis requires at least four degrees of freedom. For this reason a special opto-mechanical device was designed offering such possibilities. As depicted in Figure 3.5, the rod is embedded in-between two cylindrical aluminium holders and carried by a set of two almost perpendicular 0.1mm thin steel wires, which hold the rod with high accuracy and stability in position. Such steel wires have to be as thin as possible to reduce shading effects, seen at the re-imaged z-invariant pupil (see Figure 3.8). To adjust the relative orientation of the rod with respect to the optical axis, each cylindrical rod-holder was mounted on a set of two perpendicularly arranged linear translation stages (see Figure 3.4).

3.2.2 Alignment of the Reflective Rod

The rod alignment is the most important issue. The 3-dimensional object has to be precisely positioned by means of a 2-d imaging device like a CCD camera. A proper alignment procedure can be found by assuming first a perfect rod alignment.

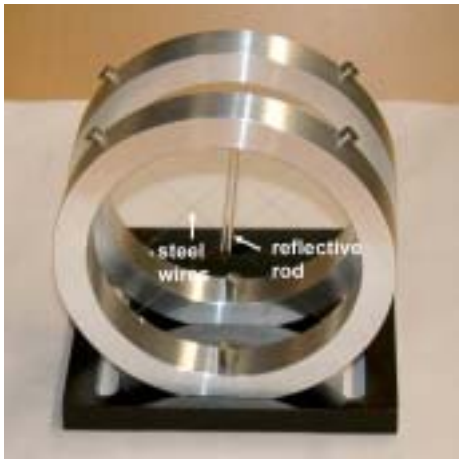

Figure 3.5: Image showing the mount embedding the reflective rod. The sensing device is held in position by a set of perpendicular steel wires.

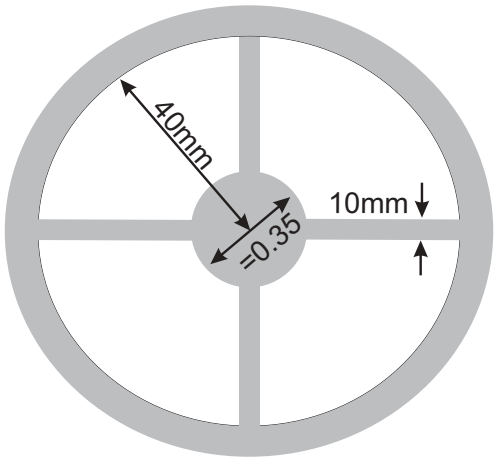

Figure 3.6: Sketch of the aperture mask used to simulate a telescope with a central obstruction of $\epsilon = 0.35$ as is the case for OWL.

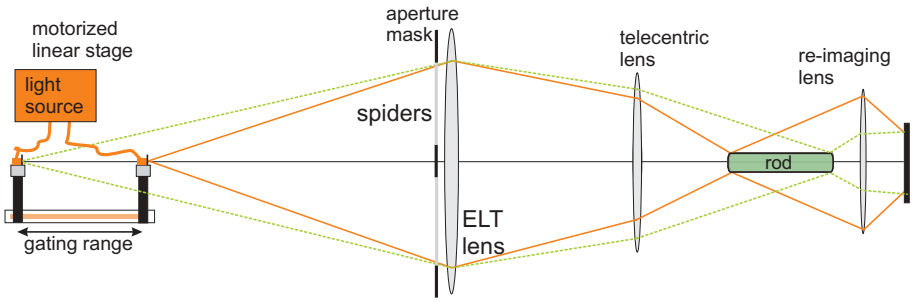

Figure 3.7: The alignment of the rod as 3-d sensing device has been verified in an iterative procedure, by applying an undistorted pupil image at both edges of the gating range of the light source (indicated by solid and dashed lines, respectively). As reference the rectangular spiders of the aperture mask were used, which are - in the case of perfect alignment- imaged congruently.

In absence of distortions, the spider cross (see Figure 3.6) arranged in the pupil will be imaged congruently. This immediately changes in the case of slight misalignment and, as a result, the cross will be transformed into a curved shape. By focussing the re-imaging system to the entrance pupil and moving the light source along the defined gating range, the user can verify the alignment accuracy at each altitude according to the curvature of the imaged spiders on the CCD. In an iterative way, the rod can be positioned by examining the resulting pupil image at both ends of the gating range (see Figure 3.7). While Figure 3.8 (left) shows a pupil image for the case of a residual rod misalignment (the spider cross is re-imaged slightly deformed), Figure 3.8 (right) depicts the pupil image after finishing the alignment procedure.

3.3 Controlling the Azimuthal Sub-aperture Size

A further important problem of the reflective rod has been discussed in chapter 2.6.2 theoretically. It is the smearing effect due to the rod curvature. Points in the pupil plane become

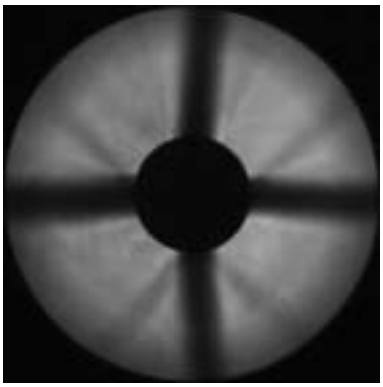
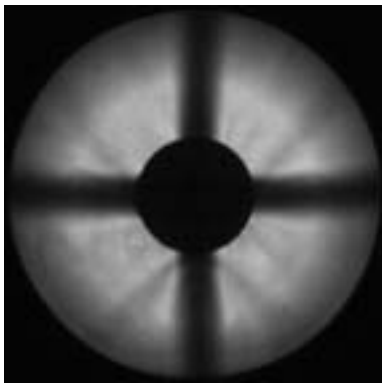

Figure 3.8: Effect of misalignment as seen in the resulting pupil image. **Left:** Already a slight misalignment leads to distortions of the spider pattern. **Right:** In an almost perfect alignment the spider pattern will be accurately re-imaged. In both cases static aberrations introduced by the steel wires of the rod holder are visible.


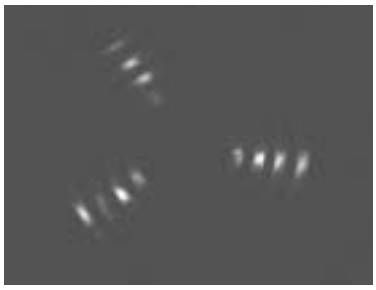
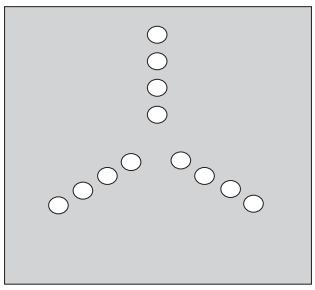

Figure 3.9: CCD images taken after placing the mask (right) in the pupil. The rod transforms holes (still visible due to reflection effects) into arcs. The images were taken for a light source size of 1.0mm (left) and of 0.2mm (middle). This leads to a resolution of 15 and 72 azimuthal sub-apertures, respectively.

converted into arcs of an angular spreading α in the image plane. In order to minimize cross-talk between sub-apertures, the azimuthal elongation of a single arc should not exceed the angular size of the azimuthal sub-apertures. The resulting arc-elongation α is exclusively determined by the ratio of imaged spot size and rod radius as was shown in section 2.6.2. Hence, to test the sensing capability of the reflective rod with a sufficient azimuthal resolution, a proper balancing of both parameters has to be guaranteed. Since for all laboratory experiments only one rod was in use, the resulting arc-elongation was solely adjustable by varying the width of the light source.

To estimate the smoothing effect, the principal setup as depicted in 3.1 has been slightly modified. The phase screen close to the pupil was replaced with a specially configured opaque pupil mask (Figure 3.9 (right)). The latter is characterized by sets of radially arranged holes separated by 120°. The LGS angular spot elongation was controlled by a plate, consisting of a set of holes with varying diameters from 0.1mm to 3mm, mounted in front of the light guide (see Figure 3.2). A pragmatic approach has been followed, by varying the hole diameter of the light source plate until the corresponding arc size drops below the desired limit. As ultimate goal, the z-invariant WFS should be able to distinguish at least 36 azimuthal sub-apertures. In this case a smoothing of the edges of the spider cross is sufficiently suppressed and ensures an accurate alignment. This leads to an over-sampling by a factor of 3 with respect to the minimum required resolution of 12 azimuthal sub-apertures. This number is the minimum

for the data reduction process aimed at fitting Zernike modes up to the 11th radial order (= 12th azimutal order) to the resulting wavefront data.

36 azimuthal sub-apertures corresponds to an angular extent of the arc-size of less than 10°. The angular size has been determined by fitting a Gauss function to a tangential cut of each arc. The desired sub-aperture accuracy was obtained by a physical spot size of 0.5mm. Figure 3.9 shows two typical images obtained for a pinhole size of 0.2mm and 1.0mm resulting in 72 azimuthal sub-apertures and 15 azimuthal sub-apertures, respectively.

As a further advantage, these images contain implicitly a possibility to check the accuracy of the rod alignment. Images of the pupil holes on the same radius have to show the same flux for a perfectly aligned system. Moreover they should not be degraded by azimuthal transformation effects.

3.4 Phase Screens and Reference Measurements

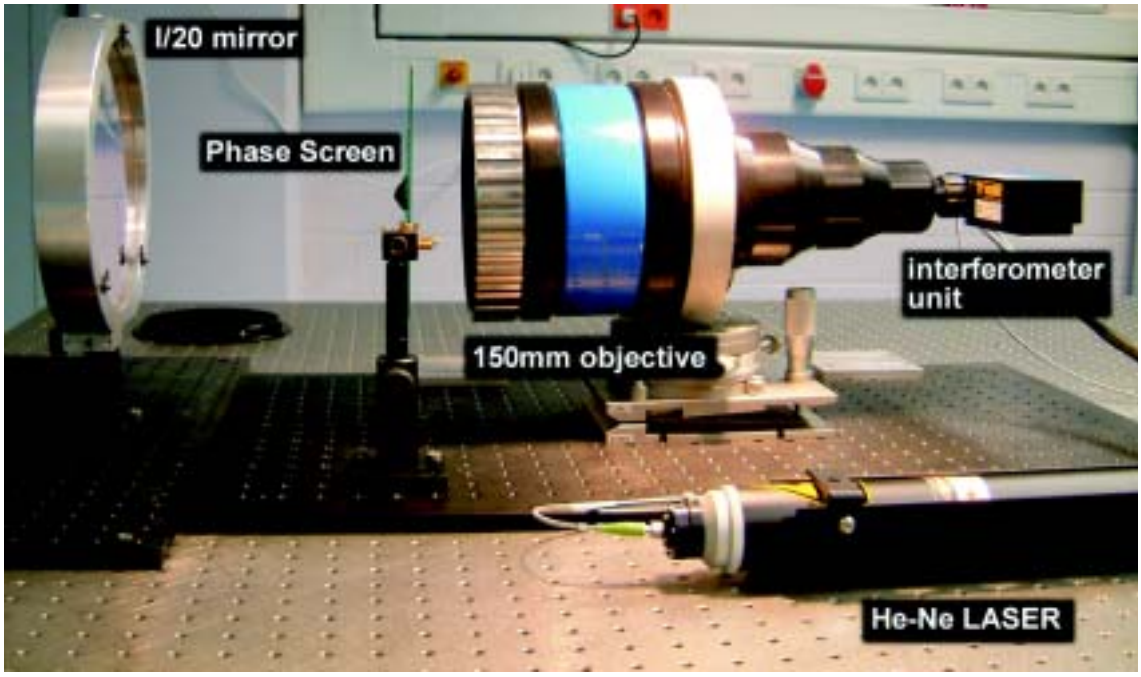

Figure 3.10: Setup of interferometric reference measurements obtained with a Twyman-Green-interferometer from FISBA. The interferometer was operated in transmission mode. The measured phase screen was inserted between the objective and a mirror of surface accuracy of $\lambda/20$.

Phase screens are a proper tool to simulate atmospherically induced wavefront phase aberrations under laboratory conditions. A variety of methods - as for instance ion-exchange (Bähr et al. (1994)) - do exist to manufacture such screens. Especially this type of phase screens is able to simulate accurately Kolomogorov turbulence and its characteristical parameters. A detailed treatment of the manufacturing process and typical measurement strategies to characterize phase screens is given in Egner (2003). A major disadvantage, however, is that such screens are quite expensive and not necessarily required to verify sensing techniques like in this case. Hence, for all measurements done in the laboratory, conventional window glass and commercially available CD-covers have been tested. Both are suited very well,

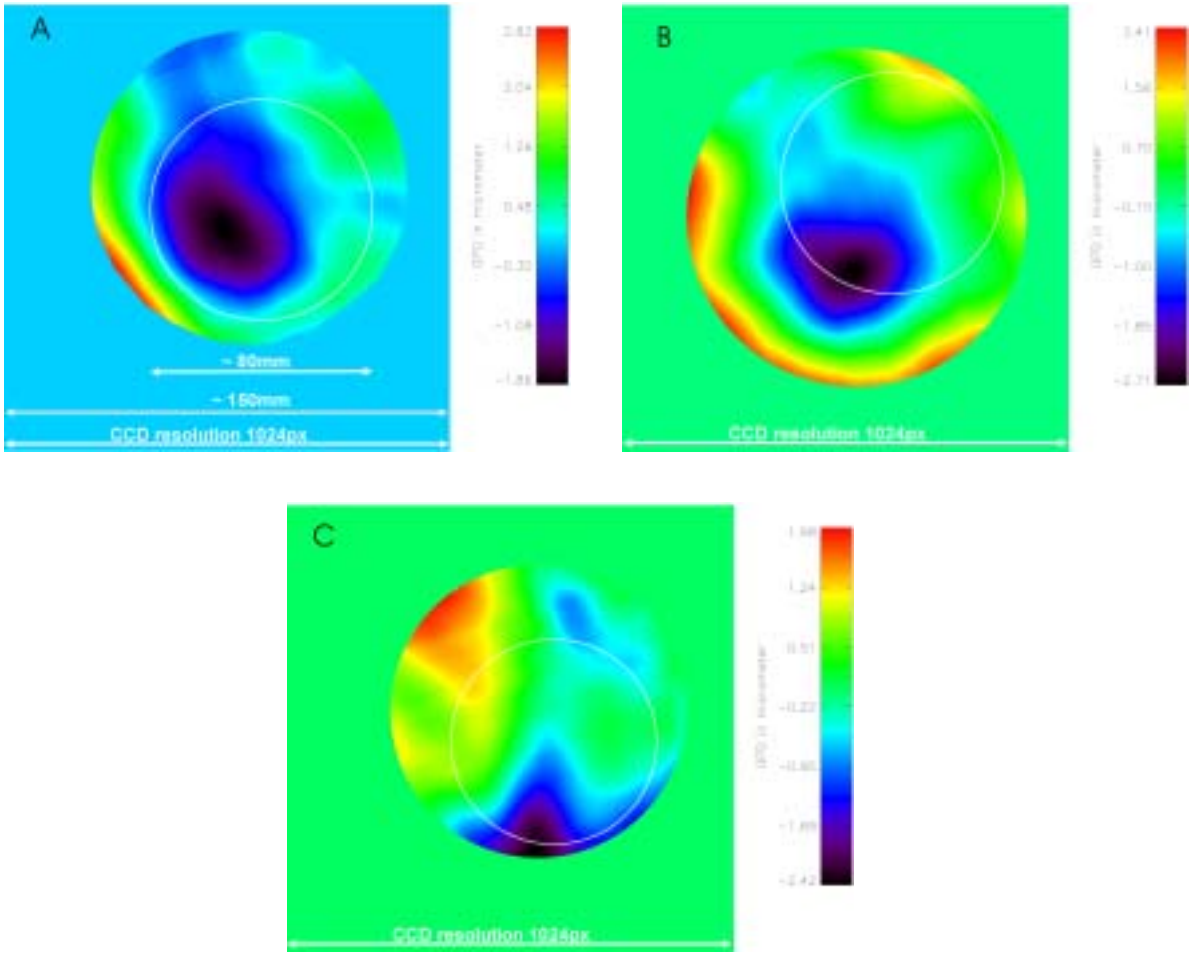

Figure 3.11: OPD reference measurements of 3 glass plates used as phase screens for the laboratory experiment. The reference measurements were performed over the full interferometer (diameter = 150mm) aperture. The Glass plates introduce PTV wavefront phase errors similar to an atmospherical distortion, of the order of several micrometers. To avoid redundancy, only those parts of the glass plate (indicated by the encircled area) have been used as phase screen for the z-invariant test setup , which impose different wavefront phase patterns.

since they introduce PTV wavefront errors of the order of several micrometers, similar to the atmosphere. Detailed measurements of the power spectrum of CD-covers have already been done in the framework of laboratory tests for the ESO Multi Conjugated Adaptive Optics Demonstrator (MAD). It could be shown that CD-covers exhibit a phase power spectrum quite comparable to a Kolmogorov distribution, since low spatial frequencies are contributing stronger to the induced wavefront phase error than high spatial frequencies (Vernet et al. (2002)). For practical reasons window glass was preferred as phase screen for all z-invariant experiments, since it was much easier to perform suitable reference measurements. Such reference measurements (see Figure 3.10) have been done using a Twyman-Green Interferometer from FISBA Optics (resolution 1024px $\times$ 1020px) reconstructing the induced absolute Optical Path Difference (OPD) of each phase screen in Ångstrom.

Figure 3.11 shows for 3 glass plates (later used for the laboratory measurements), the interferometrically reconstructed OPD after removing tip-tilt. They were sampled over the full interferometric aperture of 150mm and induce PTV wavefront errors between 4.4μm and 5μm. Screens A and B show both similar de-focus structures localized close to the center of

each screen. From this it becomes obvious why it is advantageous to record such glass plates over a wider field of view. This way one is able to select the parts of each screen showing the least similarities in the induced wavefront phase error pattern. In the picture, areas of each screen, which finally have covered the ELT-lens pupil for the z-invariant measurements, are indicated by circles.

3.5 Controlling Phase Screen Position and Warping Effects

3.5.1 Phase Screen Positioning

How does one verify which part of the measured phase screen covers the pupil of the ELT lens? How does one ensure that reference and z-invariant pupil images superimpose? *Fiducial marks* are in this framework a suitable tool to handle both. An additional glass plate was marked with an asymmetric dot-pattern, which can be identified on a one-to-one basis at the corresponding pupil images. For the data acquisition process, the reference plate has been fixed with modelling clay in front of the phase screen. Measurements with and without reference glass plate must be performed in order to define the relative position at the CCD images for each phase screen. To guarantee that the fiducial marks are equivalently oriented with respect to the phase screen, both were marked with reference crosses (see Figure 3.12).

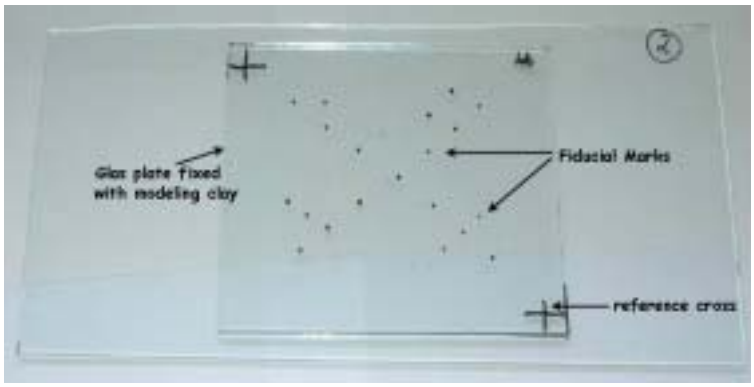

Figure 3.12: Phase screen with fiducial mark screen on top: In order to guarantee a proper alignment a re-moveable fiducial mark screen was used. Reference crosses give the possibility to detach the fiducial mark screen and re-install it later in the same position.

3.5.2 Plate Scale Adjustment and Warping Effects

Fiducial marks are not only suitable to verify the absolute positioning of the phase screen with respect to the pupil image. It is moreover possible to characterize quantitatively induced warping effects on the re-imaged pupil by misalignment of the rod. Even in the case of perfect alignment, fiducial marks might be quite useful to trace the relative plate-scale change of the pupil images imposed by the different resolution of the CCDs. To remove the influence of the limited positioning accuracy of the rod, it was assumed that a misalignment distorts the re-imaged pupil (and therefore also the shape of the OPD-surface) according to a geometrical transformation. Such a transformation is in the 2-d case defined by:

$$g[x, y] = f[x', y'] = f[a(x, y), b(x, y)] \tag{3.1}$$

where $g[x, y]$ represents the pixel in the output image at coordinate (x, y), and $f[x', y']$ is the pixel at (x', y') in the input image that is used to derive $g[x, y]$. The functions $a(x, y)$ and $b(x, y)$ can be described as polynomials in x and y of degree N and specify the spatial transformation by a set of equations. Considering only first order effects leads to a cut-off after the linear term and one can write:

$$x' = a(x, y) = a_0 + a_1 x + a_2 y + a_3 xy \tag{3.2}$$

$$y' = b(x, y) = b_0 + b_1 x + b_2 y + b_3 xy \tag{3.3}$$

Neglecting the mixed xy term the resulting equations comprise 6 free parameters. These parameters can model low order distortions like a relative shift in x, y-direction, rotation, radial scaling and a linear shearing in x and y-direction. It turned out that such a description is sufficient to describe the induced warping metric.

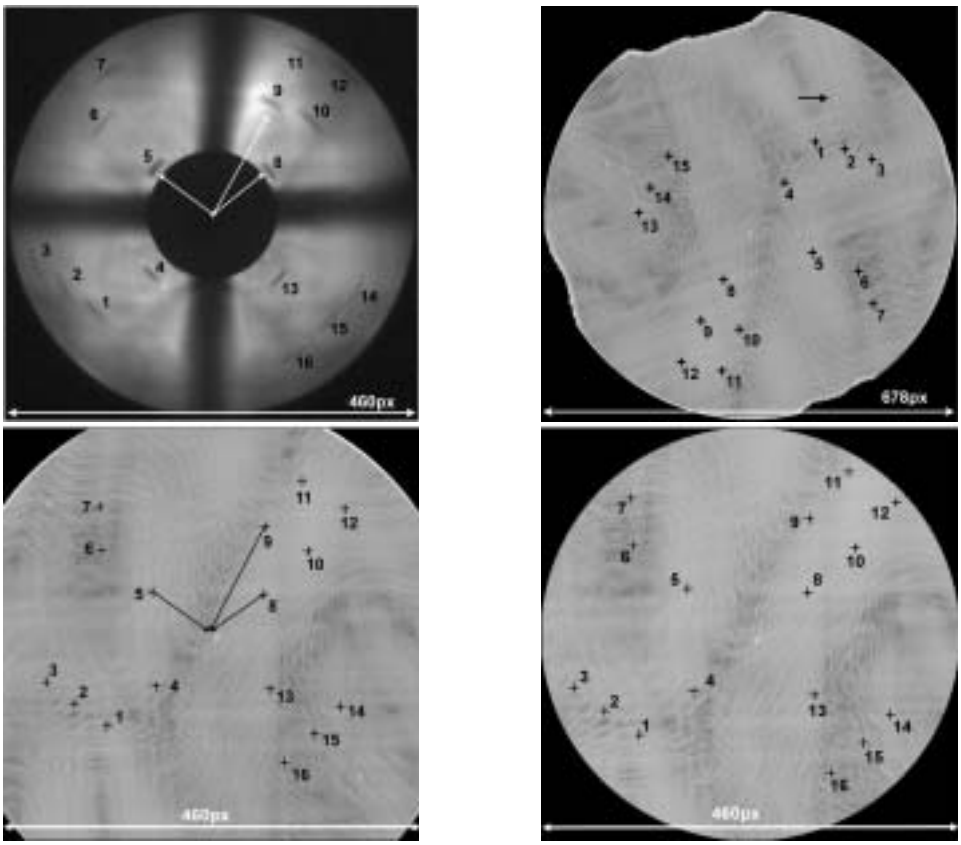

Figure 3.13: Warping and cutting the pupil image of the interferometric measurement. **Top left:** z-invariant pupil image showing fiducial marks used as reference. **Top right:** Interferometric raw image showing the corresponding set of fiducial marks (this image has been edge enhanced and contrast enhanced by a suitable power law transformation). Each fiducial mark has been marked by a cross and numbered according to its counterpart in the z-invariant image. **Bottom left:** Interferometric image after applying the warping. The image is now adjusted to the same plate scale as the z-invariant pupil-image. In order to find the corresponding center one can trace the position vector of several fiducial marks. **Bottom right:** Applying a pupil mask centered around the found pupil center in order to cut only relevant phase screen areas.

A convenient way to compute the warping parameters a_i, b_i is to track the transformation of all fiducial marks of the interferometric reference via their counterpart within the

z-invariant pupil image. Figure 3.13 (upper left) depicts a typical z-invariant pupil image including several fiducial marks. They all can be identified in Figure 3.13 (upper right), which displays the corresponding interferometric reference frame.

The warping parameters a_i, b_i can be calculated straightforward. The absolute positions of each spot, according to the specified coordinate system in both data sets, are determined and then inserted into equations 3.2 and 3.3. This leads in the case of n reference spots to a set of $2n$ equations for all 6 unknown warping parameters a_i, b_i and yields the transformation in parameterized form. From this a_i, b_i were computed by performing a least-squares fit.

To verify the quality of the transformation and check if sufficient degrees of freedom have been considered, the interferometric OPD image containing the recorded fiducial mark pattern has been transformed according to the previously defined warping parameters (see Figure 3.13 (lower left)). To define quantitatively the quality of the performed warping as given by the 6 degrees of freedom, residual positioning errors of each fiducial mark with respect to the z-invariant image were determined. Such errors were in the worst case (considering a sub-aperture close to the central obstruction) to be found within 1/6 of a azimuthal sub-aperture. To crosscheck, a warping according to an 8-parameter transformation has been done, but did not yield significantly better accuracy.

For the further data evaluation, one has to define a pupil mask, which constrains the aperture to relevant parts visible in both data sets. This is necessary for a final comparison of the interferometric pupil images with the corresponding z-invariant pupil images. For a proper centering, the corresponding center position in 3.13 (lower left) has to be determined. This is done by calculating the position vector of several fiducial marks with respect to the pupil center of the z-invariant image. Figure 3.13 (lower right) shows the ultimately transformed and cut interferometric reference frame superimposed with an accurately centered circular pupil mask.

3.6 Data Acquisition and Evaluation

The laboratory experiment has been done in open loop, and was designed to measure induced static wavefront phase errors, which were compared with the interferometric reference measurements. To simulate an extended light source in the z-invariant setup, the motorized linear stage has been moved in small steps along the defined LGS gating altitude. For all experimental runs the gating height has been divided into 40 steps. At each step, a pupil image has been taken with the CCD-camera. After the acquisition procedure all frames were numerically co-added. In order to evaluate for each phase screen the experimental data properly, several data-sets were necessary:

- Two frames were obtained with the interferometric reference measurements:
  i) One frame was taken to synthesize the OPD of the phase screen (see Figure 3.16 (top left)).
  ii) A second frame was obtained with attached fiducial mark screen in order to define the reference for the warping computation.

- Three frames were taken with the z-invariant setup:
  i) A reference image without phase screen to define the intensity distribution I. This frame eliminates static aberrations.
  ii) An image obtained by inserting the phase screen in front of the entrance pupil to determine the resulting intensity distribution I' in the aberrated case (See Figure 3.15).
  iii) An image with phase-screen and attached fiducial mask plate to define the reference

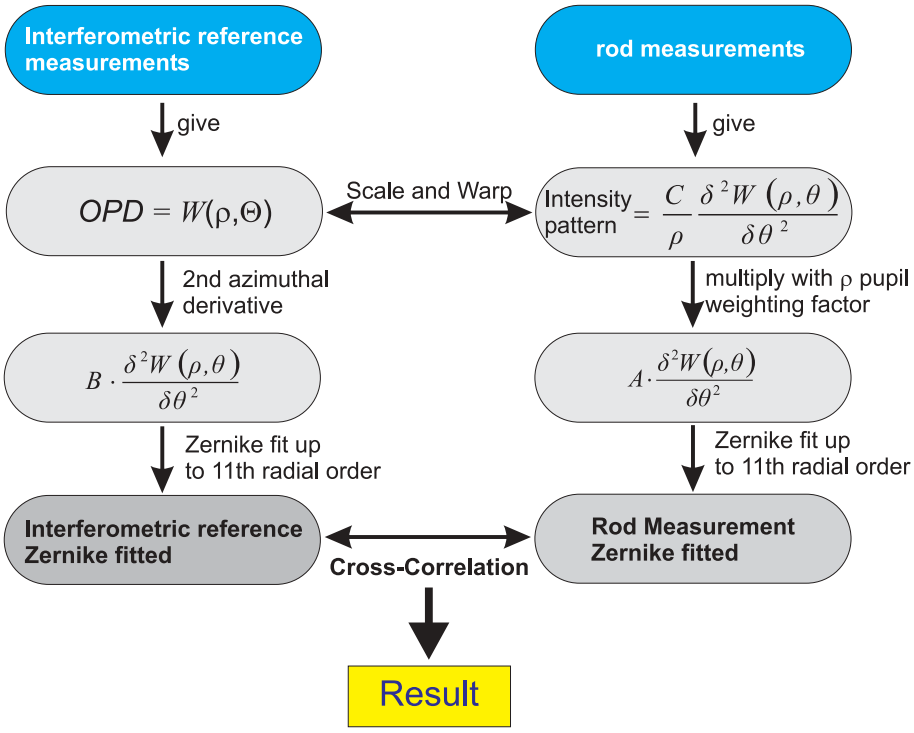

Figure 3.14: Overview of complete data reduction pipeline

position and warping effects.

To keep the entire data processing as simple as possible, the data were reduced according to equation (see section 2.6)

$$\frac{\Delta I}{I} \propto \frac{C}{\rho}\frac{\partial^2 W(\rho,\theta)}{\partial\theta^2} \tag{3.4}$$

While the z-invariant measurements contain information about the left part of equation 3.4, the right part can be computed out of the interferometric OPD data-set (giving $W(\rho,\theta)$). Hence, both data sets have to be still processed further, before they can be ultimately compared by correlation analysis (see section C). An overview of all necessary steps to perform the full reduction procedure is depicted in Figure 3.14.

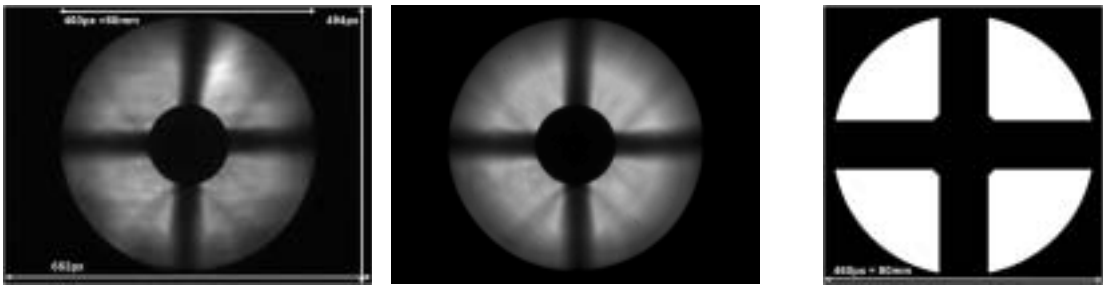

Figure 3.15: Raw images taken of the z-invariant setup. **Left:** Image including Phase Screen giving I'. **Middle:** Reference image to measure static aberrations giving I. In both cases, the shading of parts of the pupil, due to the aperture mask, is visible. **Right:** A digital pupil mask to define all areas relevant for the further correlation analysis.

3.6.1 Reduction of Interferometric Measurements

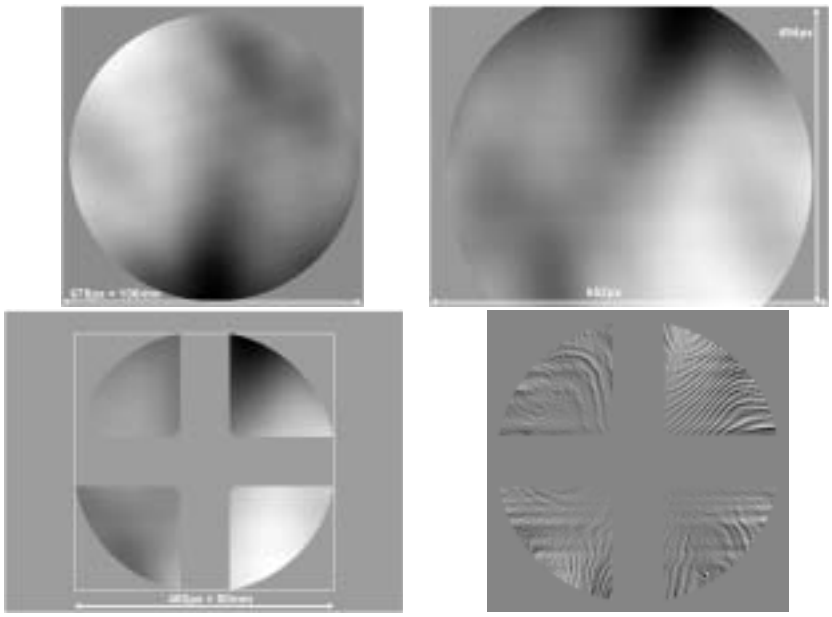

Figure 3.16: **Upper left:** Interferometric OPD raw data of a phase screen. **Upper Right:** Warped OPD image after performing proper transformation. **Lower Left:** Warped OPD image superimposed with pupil mask. **Lower Right:** Resulting second azimuthal derivative of warped interferometric OPD image. The image suffers high spatial frequency noise probably originating from the low surface accuracy of the glass-plate.

According to the defined procedure in section 3.5.2 the interferometric OPD raw data (see Figure 3.16 (upper left) was in a first step transformed to remove induced warping effects (see Figure 3.16 (upper right)). Then relevant parts were cut with a suitable pupil mask defined by the z-invariant pupil-images (see Figure 3.15 (right)).

The information about the second azimuthal derivative of the wavefront (see Figure 3.16 (lower right)) has been retrieved by numerical computations . Starting from the basic definition of the second derivative $f''(x)$ of a function $f(x)$ in the one-dimensional case, which is given by

$$f''(x) = \frac{f'(x+h) - f'(x)}{(x+h) - x} = \frac{f'(x+h) - f'(x)}{h} \tag{3.5}$$

and inserting the expression for the first derivative

$$f'(x) = \frac{f(x+h) - f(x)}{(x+h) - x} = \frac{f(x+h) - f(x)}{h} \tag{3.6}$$

leads to:

$$f''(x) = \frac{\frac{f(x+2h)-f(x+h)}{(x+2h)-(x+h)} - \frac{f(x+h)-f(x)}{(x+h)-x}}{(x+h) - x} = \frac{\frac{f(x+2h)-f(x+h)}{h} - \frac{f(x+h)-f(x)}{h}}{h} \tag{3.7}$$

h in the denominators may be set in the case of digital images to 1, which yields:

$$f''(x) = f(x+2h) - 2f(x+h) + f(x) \tag{3.8}$$

In the discrete space of digital image processing, $f(x+2h)$ and $f(x+h)$ may be defined by shifting the initial function $f(x)$ for 1, 2 pixel in the direction of x. Considerations have to

be extended into 2-d space. Assuming polar coordinates the second azimuthal derivative f''_{az} for an image I can be defined as:

$$f''_{az} = rot(I, 2\zeta) - 2rot(I, \zeta) + I \tag{3.9}$$

where $rot(I, \zeta)$ defines a rotation operator, rotating the image by a small angle ζ.

3.6.2 Reduction of z-invariant Data

According to equation 3.4, the intensity ratio $\frac{\Delta I}{I} = \frac{I'-I}{I}$ can be computed out of the obtained z-invariant rod measurements providing I and I'. The resulting frame (see Figure 3.17 (left)) is cut and superimposed by a pupil mask. Such a pupil mask (see Figure 3.15 (right)) was constructed to exclude all (for the correlation) non relevant parts, such as central obstruction and areas shaded by the spider-cross.

Equation 3.4 contains on the *right* side in the denominator a normalized radial weighting factor ρ (see Figure 3.17 (middle)), which has been taken into account by multiplying the resulting intensity ratio on the *left* side. This has been done in order to prevent singularities in the case of a division and hence numerical issues for points close to the center of the pupil ($\rho \to 0$). This step finally yields image 3.17 (right).

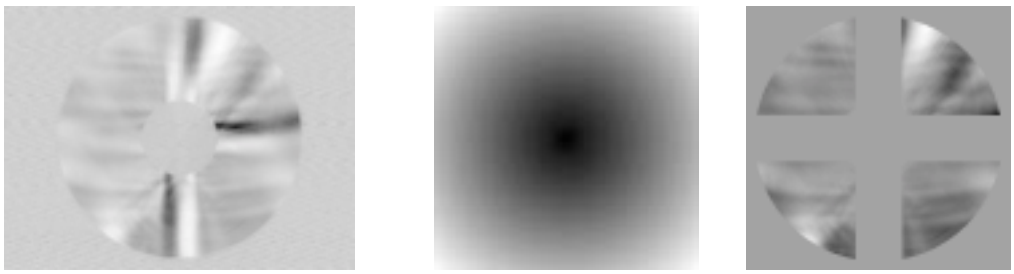

Figure 3.17: z-invariant data reduction steps: **Left:** resulting z-invariant frame from computing the ratio $(I - I')/I$ given by the obtained data sets. **Middle:** Normalized ρ weighting function (center 0, pupil border 1). **Right:** Final z-invariant pupil ratio superimposed with pupil mask.

3.6.3 Results

In principle, already now both data sets should show a similar intensity pattern, and can be compared by correlation analysis (see appendix C). Considering the up to now reduced z-invariant and interferometric images (Figure 3.16 (right) and Figure 3.17 (right)), both suffer from high spatial frequency noise contributions originating from irregularities and low surface quality of the used phase screens. In order to reduce this effect, images are smoothed by fitting Zernike polynomials up to the 11th radial order. In total, 3 different screens were tested.

Figure 3.18 depicts the amplitude spectra of Zernike modes fitted to z-invariant and interferometric reference measurements of each screen, respectively. Figure 3.19 shows the Zernike fitted z-invariant and interferometric data sets. All are characterized by a strong correlation already visible by eye. Table 3.1 denotes the obtained correlation between z-invariant and interferometric Zernike coefficient sets. For all phase screens, the correlations are better than 80%. Although the results are convincing, a higher correlation might be hampered by several

reasons. As main error source low surface quality and residual misalignment of the sensing device can be seen. Both effects impose static aberrations, which were not completely removed by the calibration. Further errors are introduced through the limited accuracy of the 6-parameter transformation, where high-order warping effects are not sufficiently described. Finally, the limited dynamic range of the used sensing CCD (8 bit) might be a further issue. Taking into account these limitations, the results verify the functionality of the z-invariant sensing concept.

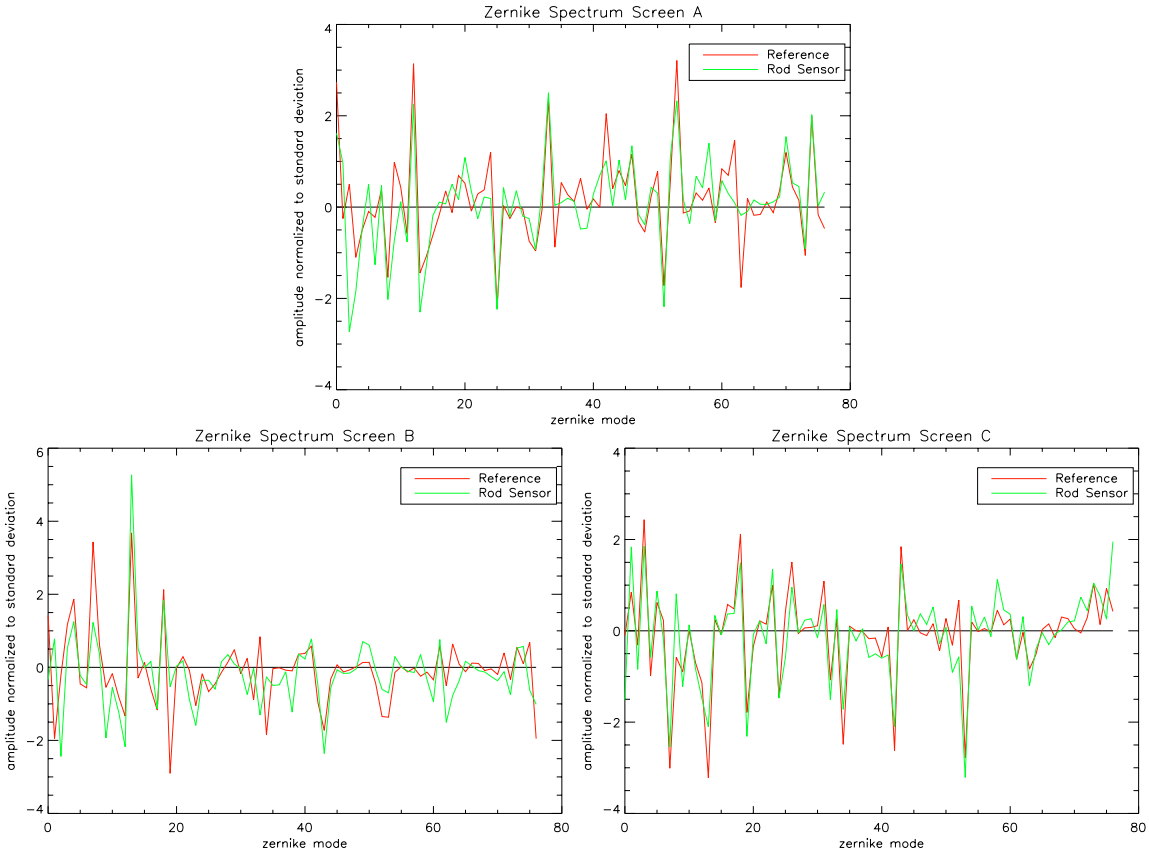

Figure 3.18: Resulting Zernike amplitude spectra for corresponding z-invariant and interferometric data set, depicting the strong correlation of all three phase screen measurements.

phase screen	Screen A	Screen B	Screen C
correlation	88%	85%	80%

Table 3.1: Computed correlation coefficients for 3 different phase screens. The coefficients were obtained by correlating the resulting Zernike amplitude spectra of reduced interferometric and z-invariant data.

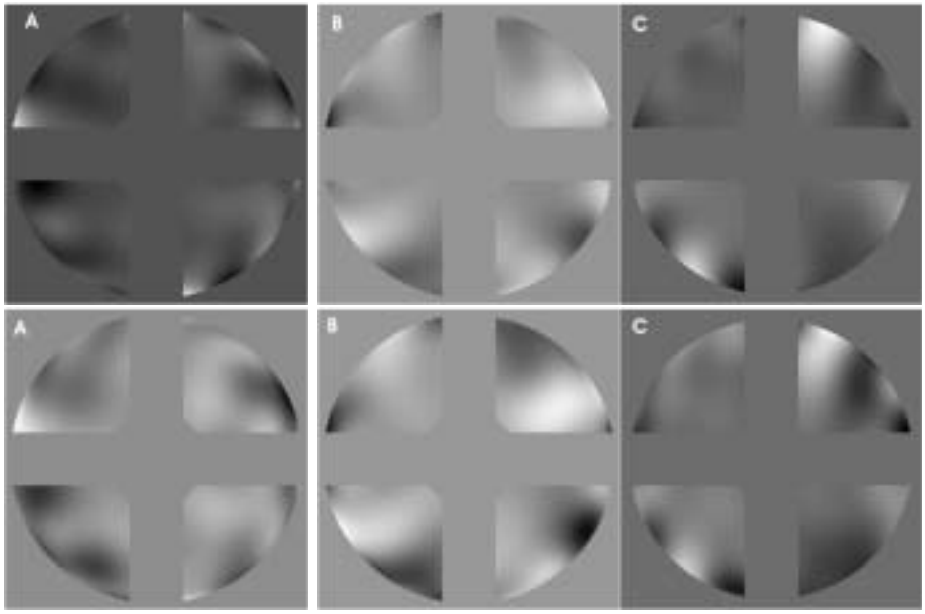

Figure 3.19: Fully reduced and Zernike fitted images of interferometric (first row) and z-invariant (second row) data sets for three different phase screens A, B and C (from left to right). Already by eye a strong correlation is visible.

3.7 Limitations of Laboratory Setup for Slit-Mask Verification

Limited by practical issues, a similar laboratory study of the circular slit mask as a practical implementation of the IBB-concept was not possible. As deduced in 2.5.1, the gain of the slit mask required to amplify phase errors is determined by the ratio $4H/D^2$. Hence, it does only depend on parameters which cannot be properly adjusted in a laboratory experiment. In the real LGS-OWL configuration the parameters H and D lead to a sufficient amplification of the measured wavefront error of the order of 40. In the case of the laboratory setup, this value drops to 0.625 considering the optical configuration in the case of the z-invariant setup.

As shown in the introduction part of this chapter, a proper down-scaling conserving the

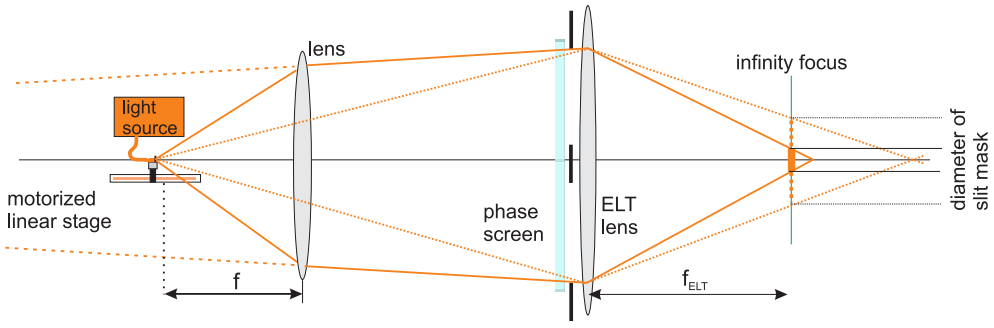

Figure 3.20: To increase the F-Ratio of an incoming beam and thus projecting the light source virtually to a greater distance, an additional lens has to be placed with respect to the light source in distance close to it focal length. .

geometrical ratios at the telescope results in a distance of 100m for the light source with respect to the telescope simulator lens. Such a distance can be simulated by introducing a suitable lens, which is positioned from the light source close to its focal length to increase the F-ratio of the incoming beam (see Figure 3.20). This approach has nevertheless an impact on the resulting focus position of the imaged light source, which is projected closer to the telescope infinity focus. As a consequence, the diameter of the converging beam in the infinity focal plane, constraining the size of the slit mask, will be strongly decreased. A ZEMAX simulation yields a mask of a diameter of 0.48mm. Neglecting for the moment imposed alignment complications, such masks cannot be manufactured anymore with conventional drilling or milling techniques. A possibility would be, e.g., to build such a mask by lithographic techniques. However, assuming a minimum number of 5 required slits in order to cover the entire pupil, this leads to a slit-to-slit distance of $40\mu m$. Hence, the resulting slit width is of the order of several microns, which is of the order of the wavelength of light. Due to diffraction effects, this leads to a strong smearing of the imaged radial sub-aperture, drastically limiting the sensing capability.

Chapter 4

PIGS - First Results on the Sky

Encouraged by the convincing results obtained under laboratory conditions, the z-invariant sensor has been tested in an open loop experiment at the 4.2 m William Herschel Telescope (WHT) at La Palma. This has been accomplished in collaboration with the university of Durham and the Isaac Newton Group (ING), which operate since 2001 a Rayleigh laser guide star (RLGS) demonstrator (Morris et al. (2004)) at the WHT. At the WHT, the RLGS is thought to be an extension of their AO-system NAOMI, and it will be part of the planned Ground-layer Laser Adaptive optics System (GLAS).

The WHT is the only telescope in Europe equipped with a low altitude RLGS facility. It fulfills several premises for the realization of the PIGS experiment, e.g it provides an optical bench accessible in one of the Nasmyth platforms. The major idea was - in analogy to the laboratory experiment - to build a down-scaled version conserving the geometrical ratios of the sodium LGS - ELT conditions. In the case of a 4.2m telescope this translates into a LGS height of roughly 4km and a focussing range of 500m. To keep the optical design and necessary modifications as simple as possible, the goal was to embed the PIGS-WFS unit into the RLGS beam. The total available experimental time was split into two runs of 4 full nights in September 2003, and 2 full and 2 half nights in November 2003. The experiments were performed, as a kind of add-on, in parallel to on-sky demonstrator tests of the RLGS-system. Hence, the WFS experiment and its success was mainly constraint by the stability, functionality and availability of the RLGS. Due to the constraints given by the status of the laser system, expectations in terms of quantitative results were not too high. The main goal of this experiment was to test the sensor functionality in a more realistic environment and to obtain preliminary results on the feasibility of the design. Additionally, it was possible to learn more about the limits of the z-invariant sensor. This experience provides a guideline for follow-up experiments. Another task was to invent and test a procedure to align the rod as accurately as possible to the optical axis determined by the RLGS. While in a laboratory framework the alignment of the z-invariant senor can be done (as seen in chapter 3.2.2) in a straightforward manner, at the telescope this becomes more demanding. The test of the mask was limited by the low power of the RLGS and should be repeated after the new, by far more powerful laser planned for the WHT, is commissioned. The results for the z-invariant sensor were better than expected. It was possible to show in a qualitative way that the rod-sensor is working by localizing and following the movement of the ground layer turbulence in both the reference data and z-invariant data set.

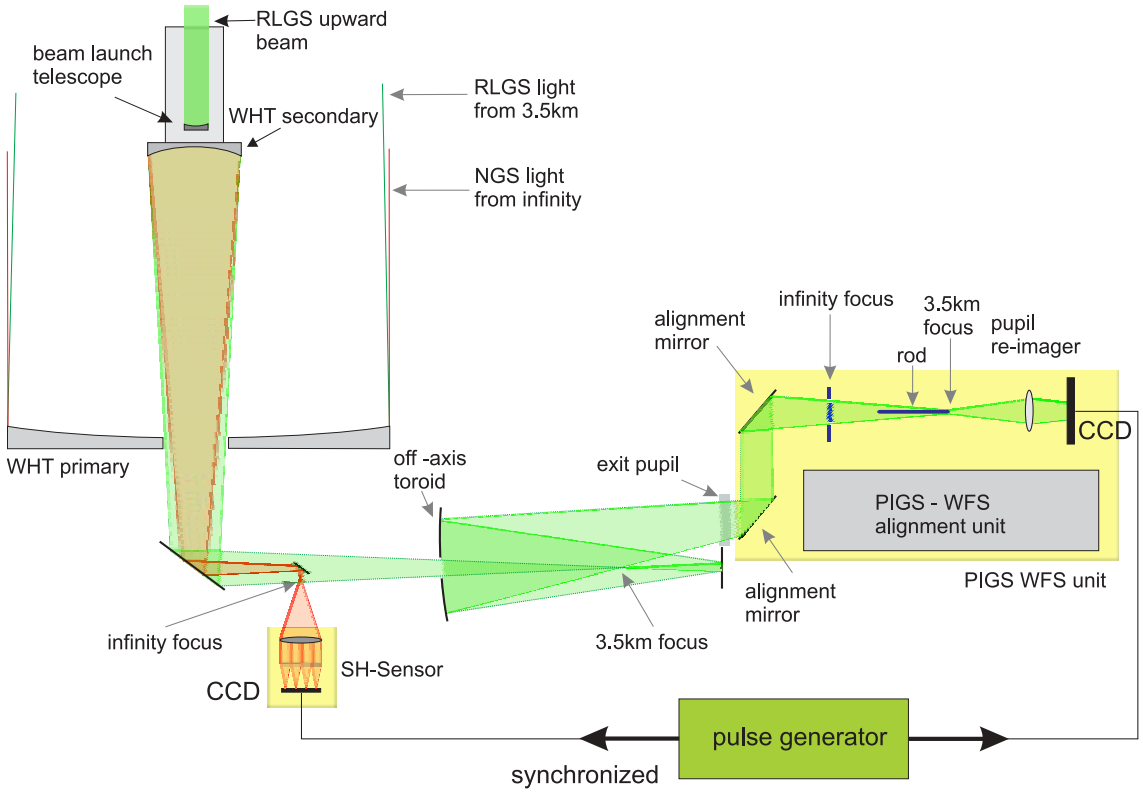

Figure 4.1: Principle layout of the WHT experimental setup. Light of a ND:YLF DPSS laser (P=3W, output wavelength 532nm) forms an artificial guide star in the atmosphere. Backscattered photons are collected by the telescope primary mirror and focussed into the Nasmyth platform laboratory, where the wavefront sensor experimental setup was located. The incoming beam from the LGS is sensed by the PIGS WFS unit, while light of a NGS is sensed by a SHS performing reference measurements. The cameras of both sensors have been synchronized via a pulse generator.

4.1 Principle Layout of the WHT Experimental Setup

Figure 4.1 depicts an overview of the experimental setup. The RLGS was placed in one of the Nasmyth platforms (GRACE). The laser light was relayed over tubes to a beam launch telescope, mounted above the secondary mirror (see Figure 4.3 (left)). Photons of the RLGS originating at the gating height were collected by the telescope optics, and the converging light beam was focussed into the second Nasmyth platform (GRHIL). The incoming light was further processed by an off-axis toroid, which creates with respect to the 3.5km focus an $F/15$ beam. The PIGS WFS-unit was plugged into the system behind an exit-pupil, using the latter as entrance pupil for its own optical system. It included 2 folding mirrors for alignment purposes, the WFS-devices as well as a re-imaging objective and a CCD camera, which was conjugated to the pupil. In order to get reference measurements, a pick-up mirror, placed close to the infinity focus, folded the beam of a NGS to a SHS device. In principle one would prefer also to use photons of the RLGS for reference measurements, but this is hampered by two limitations:

- As verified by radiometric calculations to estimate the expected photon return, the LGS was not bright enough to be fed into both WFS systems via a beam-splitter (see 4.2.2).

- Due to the proper scaling of the sodium LGS-ELT configuration, the SHS, when conjugated to the Rayleigh beacon, will suffer all limitations as described in chapter 2.1. This would lead to a low quality of the reference data.

Therefore the RLGS was positioned as close as possible to a bright star used for reference measurements. An accurate verification of the absolute distance of RLGS and NGS was not possible. Imposed by angular anisoplantatism, both sensors will sample different information about incoming wavefront phase aberrations. Moreover, while the SHS will measure the integrated column of the atmosphere, the RLGS will only probe ground layer turbulence. Hence the PIGS-WFS will only be sensitive to induced phase errors from atmospherical layers at a very low altitude. SLODAR measurements done for the La Palma site confirm that nearly 80% (see Figure 4.2) of the entire turbulence is on average located within the first 2-3 km. Therefore it was assumed to be feasible to obtain an adequate correlation when comparing the data of both sensors. The entire experiment was done in open loop and both CCDs (LGS and NGS CCD) were synchronized in order to provide frames taken simultaneously.

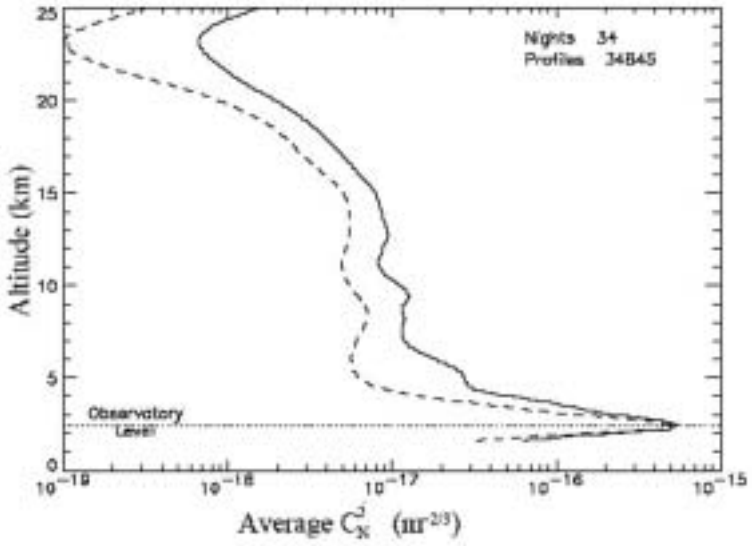

Figure 4.2: Mean C_n^2-turbulence profile for La Palma obtained by averaging 34845 profiles taken over 34 nights. Almost 80% of the turbulence is located in the ground layer within the first few kilometers. This plot was kindly provided by Jimenez and the IAC-team.

4.2 The Rayleigh Laser System

4.2.1 Laser Peculiarities

The laser used to create the RLGS was a frequency doubled solid state ND:YLF DPSS laser. It had a nominal output of 5W at a wavelength of 532nm and a pulse rate of 7kHz. Due to environmental effects at the WHT and limited alignment possibilities of the laser resonator, the maximum achieved output power that has been observed at the telescope was 3W. The light has been directed along the altitude axis of the telescope for entry into the beam relay system and from there into a small beam launch telescope positioned behind the secondary mirror. The laser was aligned to the optical axis of the WHT. The beam launch telescope (BLT, see Figure 4.3) had a simple Newtonian design consisting of a 300mm parabolic mirror

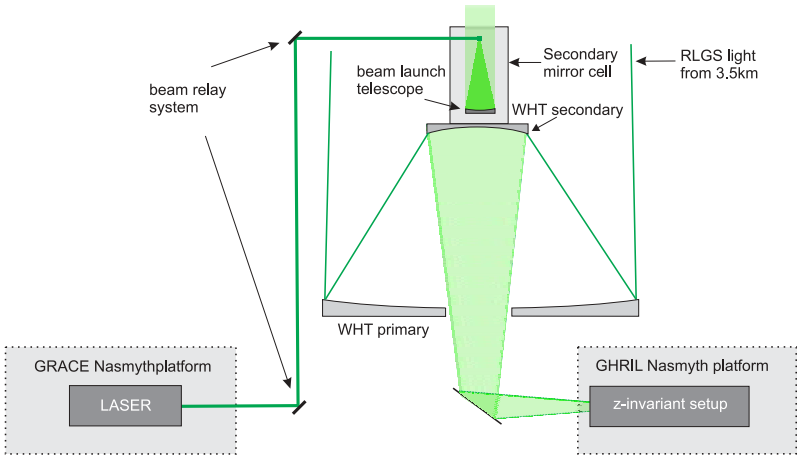

Figure 4.3: Optical layout of the Rayleigh laser system used for the experimental run.

and a 25mm dielectric fold mirror. A focussing lens mounted on a translation stage gave coarse alignment of the focal altitude, while fine beam steering and focussing was achieved by means of three worm drives that allowed the primary mirror to adjust tip, tilt and LGS focal altitude. The launch telescope enclosure was a simple box construction (depicted in Figure 4.4 (left)) wrapped with thin neopren. It prevented too much stray light in the dome, when the laser runs at full power. Moreover the beam relay was enclosed into plastic boxes, this way reducing the stray light further. Several laser diagnostic tools were available for testing and checking beam quality and spot size. To examine the spot elongation and focussing altitude, a simple TV-camera was moved along the optical axis on the bench. When changing the conjugated height of the RLGS, the diameter of the bright central region changes in both intensity and diameter. By locating the conjugate point where the central region was brightest and smallest, the focal altitude of the BLT could be estimated.

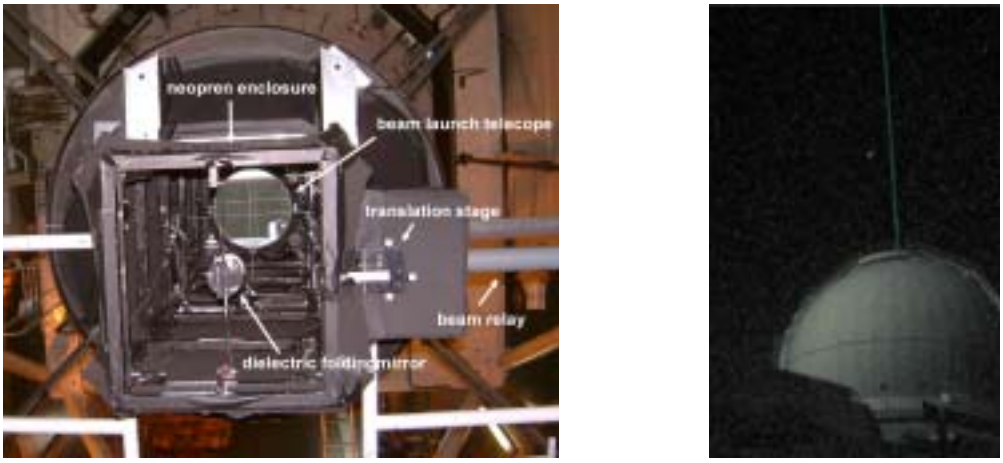

Figure 4.4: **Left:** Picture of the beam launch telescope **Right:** Image of WHT operating RLGS during the observing run in November 2003. The bright spot on the sky is Mars.

4.2.2 Photon Return Estimate

The expected photon return of the RLGS is an important quantity. It has to be estimated before performing the experiment in order to verify that the flux is sufficient for the used CCD detector. The LIDAR (LIght Detection And Ranging) equation provides a formula to compute the expected photon return at a certain range gate height assuming a laser of given output power E_L:

$$N(z) = \left(\frac{E_L \lambda}{hc}\right)(\sigma_b n_{mol}(z)\Delta z)\left(\frac{A_R}{4\pi z^2}\right)\left(T_{opt} T_{atm}^2 \eta\right) + N_B \tag{4.1}$$

$N(z)$ is the number of return photons from a height z, c the speed of light and h Planck's constant. While the first term on the right side describes the initial number of photons, the second term gives the percentage of the beam being scattered, depending on the cross-section σ_b, the molecular density at an altitude $n_{mol}(z)$, and the gating range Δz. The third term comprises the number of backscattered photons, which are collected by the telescope of the area A_R, while the last term takes into account the telescope transmission T_{opt}, atmospherical transmission T_{atm} and detector efficiency η. N_B denotes the contribution of background photons. With a gating height from 3500m to 4000m, an integration time of 30ms per image and taking into account the quantum efficiency of the CCD, equation 4.1 leads to $1.4 \cdot 10^6$ electrons per frame.

As detector for the PIGS-setup a DVC 1412 CCD (resolution 1388x1024px, physical pixel-size 6.5μm) has been used. Readout noise measurements performed in the laboratory confirmed a value of 4 e^- per pixel as stated in the manual. A feature of the CCD is its 8x8 binning capability. Depending on the size of the re-imaged pupil, which is given by the optical design in section 4.3.2, the expected number of electrons per pixel can be estimated. Table 4.1 depicts the final results. In the case of 1x1 binning mode, the number of electrons per pixel is of the order of the readout noise (S/N $\sim$ 1). With a 8x8 binning mode, a sufficient number of 350 electrons (S/N $\sim$ 18) were derived

	No. of pixel in pupil	No. of e^- per pixel	S/N per pixel
1x1 binning	≈ 250000	≈ 5	~ 1.6
8x8 binning	≈ 4000	≈ 350	~ 18.3

Table 4.1: Number of expected resolution elements within a circular pupil image at the CCD and resulting number of photons depending on the used binning mode. The CCD provides 1x1 and 8x8 binning capability.

4.3 Optical Design of the Wavefront Sensor Setup

4.3.1 Defining Critical Design Parameters

Before performing an optical design, one has to define first limiting system parameters and their expected impact on the optical setup. To verify the functionality of the z-invariant sensor, the aim was to have a reasonable number of distinguishable azimuthal sub-apertures (18) for the on-sky experiment. Based on this, one is able to constrain the necessary diameter of the reflective rod. Its value may be deduced following geometrical considerations and by calculating the expected physical size of the LGS spot on the rod. As a result the angular spreading of a point in the re-imaged pupil can be expressed as a function of the rod-diameter.

The physical size u of the LGS spot is defined by the LGS angular spot elongation and the effective focal length of the telescope ($\mathrm{EFL_{WHT}}$):

$$u[\mathrm{mm}] = \frac{\mathrm{LGS}[''] \cdot \mathrm{EFL_{WHT}}[\mathrm{mm}]}{206264[''/\mathrm{rad}]} \tag{4.2}$$

According to section 2.6.2, the angular spreading α is defined by:

$$\alpha = 2 \cdot \frac{u}{d_{rod}} \tag{4.3}$$

Table 4.2 shows the estimated angular spreading of the re-imaged arc and the number of distinguishable sub-apertures as a function of LGS angular size and rod diameter. Even in the case of a moderate angular spot elongation of up to 3", a rod of 4mm in diameter should be able to distinguish at least 18 sub-apertures.

	LGS angular size ["]			
rod diameter	2"	3"	4"	5"
4mm	14°/25	**20°/18**	27°/13	35°/10
5mm	12°/30	17°/21	22°/16	28°/12
6mm	10°/36	14°/25	19°/19	24°/15
8mm	7°/51	11°/32	14°/25	18°/20

Table 4.2: Depending on the LGS spot elongation and rod diameter, the maximum number of distinguishable sub-apertures varies. A rod of 4mm in diameter is able to resolve at least 18 azimuthal sub-apertures (indicated in bold font) assuming a LGS-elongation (at the focussing height) of 3". This value was aimed in the performed experiment.

4.3.2 Optical Design

Based on the optical constraints determined by the telescope optics and initial parameters such as the rod-diameter, one can now work out a suitable system. The telescope fore-optics define position and diameter of the resulting exit pupil, which is used for the PIGS optical design as reference. It determines moreover the absolute focussing positions of incoming beams from altitudes of 4km and 3.5km in the image space (f_{4km} and $f_{3.5km}$). For a proper optical design, the finite rod thickness has to be taken into account. It impacts in various forms on:

- the absolute rod position, defined through the f_{4km} and $f_{3.5km}$ shifts.
- the absolute rod length required.
- the clear aperture of the pupil re-imager.

All these parameters can be calculated following geometrical optics approximations.

Relative Shift of 4km and 3.5km Focus and Rod Length

Figure 4.5 gives an explanation for the necessary shift. Considering only light rays from the exit pupil originating at an altitude of 4km, as long as the rod is placed exactly at the 4km focus (which is indicated in Figure 4.5 by the dotted line), they will not be reflected by the

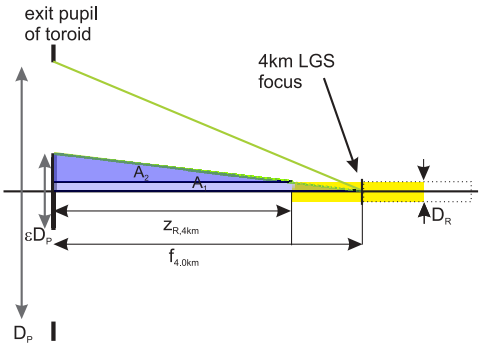

Figure 4.5: The finite rod thickness leads to a shift of the rod relative to the 4km focus.

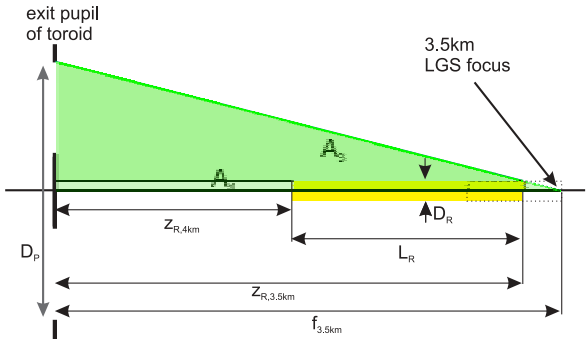

Figure 4.6: The finite rod thickness leads to a shift of the rod with respect to the 3.5km focus.

rod due to its finite thickness. The shift with respect to the exit pupil is analyzed with a ray coming close from the edge of the central obstruction. Using the similarity of the triangles A_1 and A_2

$$\frac{z_{R,4km}}{f_{4km}} = \frac{\epsilon D_P/2 - D_R/2}{\epsilon D_P/2} \tag{4.4}$$

leads to an expression for $z_{R,4km}$:

$$z_{R,4km} = f_{4km}(1 - \frac{D_R}{\epsilon D_P}) \tag{4.5}$$

where f_{4km} denotes the distance of the 4km focus and $z_{R,4km}$ the distance of the shifted rod with respect to the exit pupil. While D_P is the diameter of the exit pupil formed by the off-axis toroid, ϵ is a factor to describe the relative size of the central obstruction. D_R denotes the rod diameter. The situation changes slightly for the 3.5km focus, since in the case of no shift, all light rays from the exit pupil - originating at the conjugated height - will still incident on the rod. As a consequence, a part of the rod, close to the 3.5km focus, will not be illuminated at all (see Figure 4.6) and is hence not necessarily required. In order to estimate this length, one may assume a ray coming from the edge of the pupil. The similarity of the triangles A3 and A4 determine the end position of the rod:

$$z_{R,3.5km} = f_{3.5km}(1 - \frac{D_R}{D_P}) \tag{4.6}$$

Subtracting start and end position gives the required length as a function of the rod diameter (see Table 4.3):

$$L_R = z_{R,4km} - z_{R,3.5km} = f_{4km}(1 - \frac{D_R}{\epsilon D_P}) - f_{3.5km}(1 - \frac{D_R}{D_P}). \tag{4.7}$$

Diameter of pupil re-imager

The required clear aperture of the pupil re-imager D_{PR} is determined by the maximum F-ratio of rays from the exit pupil ($D_P/2f_{4km}$) and the maximum distance between rod and pupil re-imager ($L_R + o$)

$$\frac{y}{L_R + o} = \frac{D_P}{2f_{4km}} \tag{4.8}$$

where y is the height where the reflected ray will incident on the lens with respect to the rod surface, and o the distance between rod and pupil re-imager. With $y = D_{PR}/2 - D_R/2$ one gets:

$$D_{PR} = \frac{D_P}{f_{4km}}(L_R + o) + D_R \tag{4.9}$$

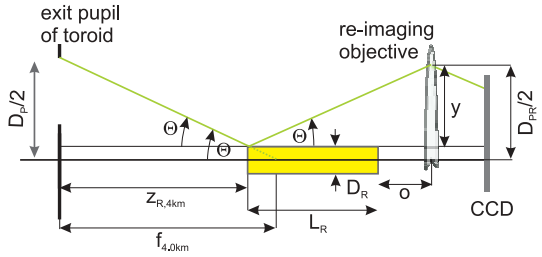

Figure 4.7: The diameter of the pupil re-imager is defined by a ray of maximal slope being reflected at maximum distance from the pupil re-imager.

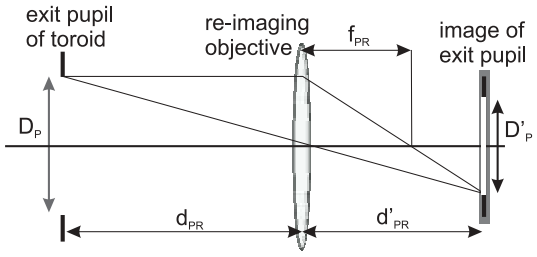

Figure 4.8: Geometrical situation to calculate position d'_{PR} and size of exit pupil image on CCD.

An Edmund Objective with 49.8mm clear aperture and a minimum focussing distance of 1000mm was used for re-imaging purposes. The minimum focussing distance defines o. In addition, as a further limitation the rod could be only aluminized over a maximum length of 250mm. Table 4.3 depicts several configurations calculated depending on the chosen rod-diameter. Obviously only a rod of 4mm in diameter could fulfill all demands.

rod diameter	rod length	distance rod exit pupil	clear aperture of pupil
4mm	**243mm**	**469mm**	**44.8mm < 49.8mm**
5mm	272mm	424mm	46.7mm
6mm	302mm	379mm	50.6mm
8mm	360mm	289mm	58.6mm

Table 4.3: Influence of varying rod diameter on system parameters like re-imaging pupil size and necessary rod length. The finally used configuration for the experiment is set in bold font.

Diameter of exit pupil image

The physical size of the exit-pupil image is not a function of the rod-diameter, but it has to be verified that it fits on the CCD chip (physical size: 8.98mm × 6.71mm). According to Figure 4.8 the magnification factor m between the absolute size of the exit pupil D_P and the exit pupil image D'_P is given by their distances with respect to the re-imaging objective ($m = d_{PR}/d'_{PR}$). d'_{PR} can by determined from:

$$1/d_{PR} + 1/d'_{PR} = 1/f_{PR} \tag{4.10}$$

where f_{PR} denotes the focal length of the pupil re-imager. Combining the upper equations, this ultimately gives for D'_P:

$$D'_P = (\frac{f_{PR}}{d_{PR} - f_{PR}})D_P \tag{4.11}$$

The diameter of the exit pupil was 50.8mm. Taking into account the minimum focussing distance of the re-imaging objective and its focal length of f_{PR}=75mm, the diameter of the re-imaged pupil on the CCD is $D'_P = 4.05$mm.

4.4 Alignment of PIGS WFS Unit

4.4.1 Alignment Strategy

One of the most important points is to find a proper alignment procedure for the rod sensing device with respect to the optical axis of the RLGS. As shown in chapter 3.2.2, already a small mis-alignment leads to severe warping effects, which limit strongly the data quality. The proposed alignment procedure performed for the lab experiments (tracing and minimizing the warping of the spider cross in the pupil) was not executable due to low flux of the RLGS and several practical complications arising at the telescope:

- To form a pupil-image at the CCD-camera, which is created by rays reflected at the rod surface, an already accurate first guess of the final rod position is required. While in the laboratory this can be accomplished by tracing the focus position of the extended light source at different gating altitudes, in the case of the WHT experiment the focussed RLGS spot was too faint and too smoothed to be identified sufficiently.
- To trace the shape of rectangular structures at the re-imaged pupil, a sufficient resolution is required. This premise was not given, since the WFS-camera was operated at 8x8 binning mode.

Hence a different approach for the alignment was followed to ensure correct positioning of the rod. An additional optical auxiliary setup was necessary, which was integrated in the WFS optical setup. Figure 4.9 shows a sketch of the complete auxiliary setup. The system consists of a HeNe-laser, a white light source, a 25micron pinhole, two folding mirrors (to keep the system compact) and a focussing lens with an aperture stop mask. The basic idea was to align the rod to an internally defined optical axis and to adjust the RLGS to this axis by means of two folding mirrors (See Figure 4.12) before the observation.

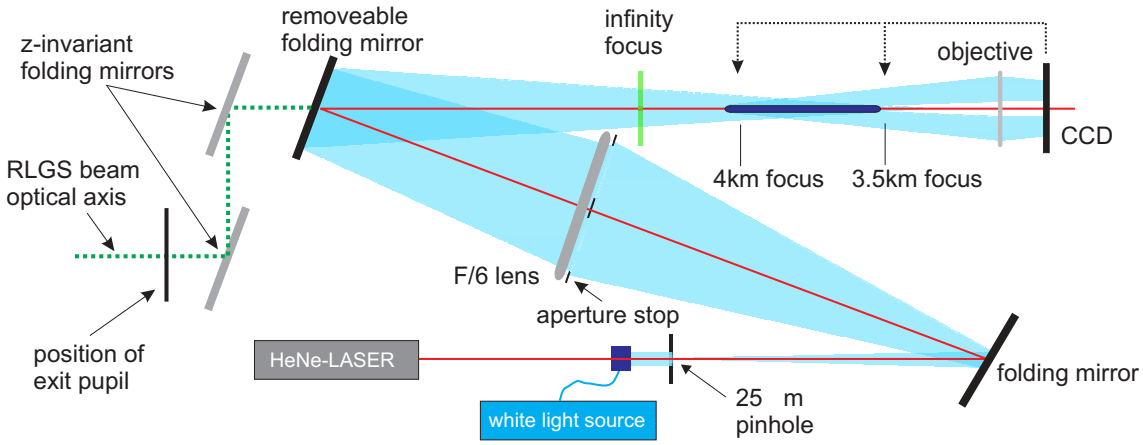

Figure 4.9: Sketch of the alignment setup. By means of a HeNe laser an internal optical axis has been defined relative to which the rod was aligned. The RLGS axis was later aligned to the internal axis by means of two folding mirrors.

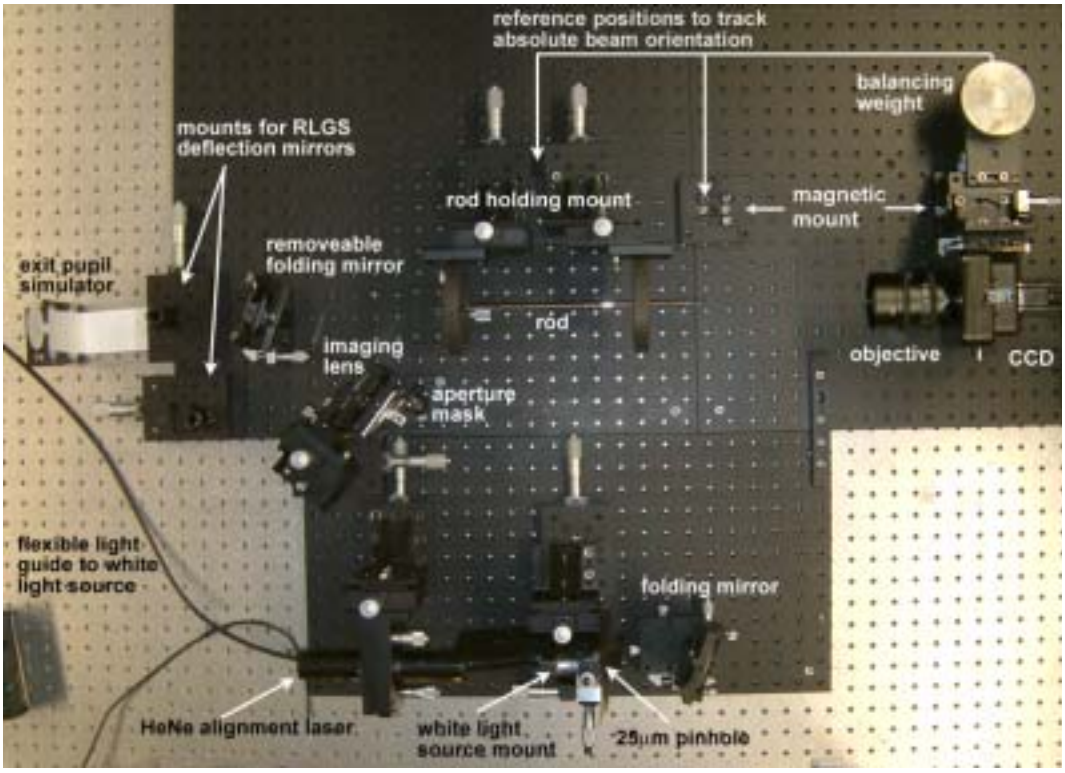

Figure 4.10: Picture of the complete WFS optical setup, including alignment components. To measure the orientation of auxiliary optical axis and RLGS axis, the CCD was placed at different reference positions (indicated by arrows). To guarantee a flexible positioning, the CCD was fixed on a magnetic mount. A balancing weight guaranteed the stability of the CCD.

The alignment procedure defines in a first step the direction of the internal optical axis by means of the HeNe Laser. Its absolute orientation in 3-d space has to be recorded. This was done with placing the CCD at two different positions along the internal optical axis. For this purpose the ∼3.5km focus position and the ∼ 4km focus position have been chosen (in Figure 4.9 and Figure 4.10 indicated by arrows). For each position the centroid of the Laser spot has been recorded. A flexible positioning of the CCD was accomplished with magnetic mounts. The positioning reproducibility was verified by preliminary laboratory tests giving an accuracy in directions perpendicular to the optical axis of $\pm 1.6px$ RMS.

The rod was aligned to the internal defined optical axis following the procedure in section 3.2.2. Therefore a point source (created by a white light source and a $25\mu m$ pinhole) was focussed by means of a F/6 lens at the 3.5km focus. The lens was constraint by a suitable aperture stop (see Figure 4.14 (left)) and defined a pupil the WFS-camera was conjugated to (see Figure 4.11). Obviously, this configuration guarantees an illumination of the reflective rod over its full length with light rays coming from the pupil. The rod can be aligned by adjusting the spider cross of the aperture stop at the re-imaged pupil. This is possible since the white light source is bright enough to operate the CCD at 1x1 binning mode.

Finally the incoming RLGS optical axis has to be superimposed with the internal optical axis defined by the HeNe-Laser. In order to position a line in 3d-space, one needs at least 4 degrees of freedom. The 3-d orientation of the RLGS was controlled by 2 folding mirrors implemented directly after the exit pupil (see Figure 4.9 and Figure 4.10). After removing the rod-mount, the spot positions of the RLGS were measured placing the CCD at defined refer-

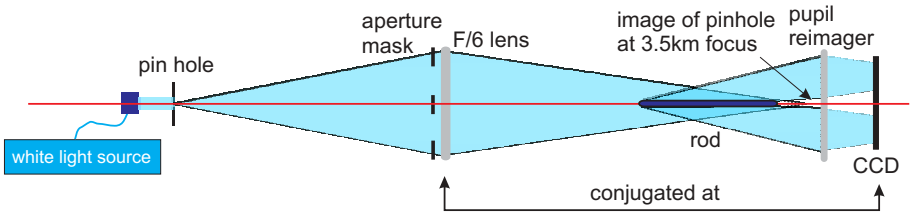

Figure 4.11: Rod alignment with respect to the internal optical axis. The light source is focussed by a proper lens at the 3.5km focus. A cone of light rays will illuminate the entire rod.

ence marks (∼3.5km focus and ∼ 4km focus) along the internal optical axis. In an iterative way the mirrors were adjusted (see Figure 4.12) until the beam of the RLGS superimposed the previously defined center positions of the HeNe Laser.

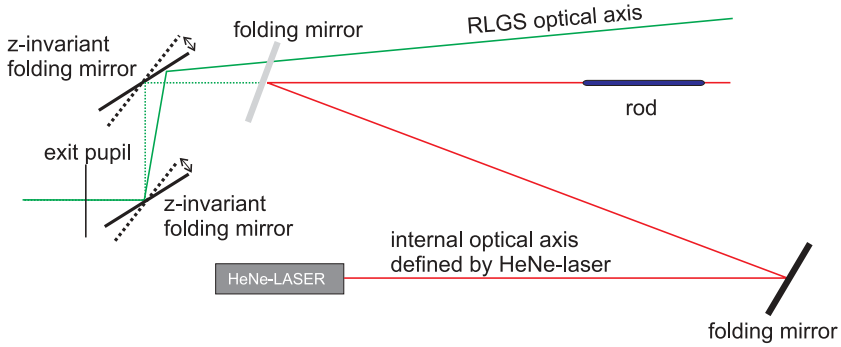

Figure 4.12: The optical axis of the RLGS can be superimposed with the internal optical axis by means of two folding mirrors.

4.4.2 Evaluating the Alignment Quality

The quality of the alignment procedure with respect to the RLGS axis was verified by means of a hole mask (see Figure 4.14 (right) and section 3.3). It has been placed at the exit pupil, to trace the conversion of points into arcs at the re-imaged pupil, when illuminating the system with the RLGS. Figure 4.13 shows the recorded point-arc pattern. Residual alignment errors become visible by comparing intersection and enclosed angle of lines fitted to the arcs/dot pattern. The pupil center of the exit-pupil is shifted by 3px with respect to the re-imaged pupil. This shows that the rod was positioned slightly off axis. Moreover an azimuthal modulation of the re-imaged pupil can be encountered. Hence it is doubtful if such alignment procedure gives sufficient accuracy.

4.5 Data Acquisition

The data sets discussed below have been taken from 11/10/2003 23:54 (UT) to 11/11/2003 00:05 (UT) according to the time stamp given by the internal clock of the z-invariant WFS personal computer. Out of the four half nights of the second experimental run, only within the last two nights the laser was fully adoptable to perform the experimental runs. In total 20 runs at different configurations were done. One run consists of a series of 512 images

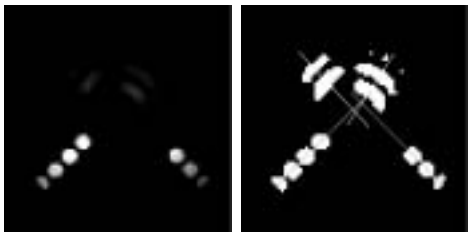

Figure 4.13: Resulting point-arc conversion pattern by inserting at the exit pupil a suitable pupil mask as shown in Figure 4.14 (right). To estimate warping effects due to rod misalignments both pattern have been fitted by lines. To enhance the signal, both images are composed out of a set of 40 single frames taken with the WFS-camera.

Figure 4.14: Pupil masks used for the experiment. From left to right: Aperture mask to perform rod alignment according to section 3.2.2. Pupil half mask to block light coming from non gated altitudes. Hole mask to estimate alignment accuracy

obtained with each sensor. The exposure-time per frame was set to 30ms and the time lag between two successive frames to 100ms.

4.5.1 Shack-Hartmann Reference Measurements

Reference measurements of wavefront phase aberrations have been obtained by sensing an on-axis NGS. Its light rays have been folded (see Figure 4.1 and Figure 4.15) by means of a pick-up mirror (FoV of 2") into a standard SHS. It was composed of a 10×10 rectangular gridded lenslet array, leading to 78 effectively used sub-apertures in the telescope pupil. The resulting spot array was imaged with a RETIGA 2000 camera. The wavefront phase errors were reconstructed by a standard method:

The relative offset of each spot centroid from a 'null' position is a measure for the local wavefront gradient within the investigated sub-aperture. To reconstruct the wavefront OPD over the pupil, one needs for each spot reference zero-positions indicating the non aberrated wavefront. The spot 'null' position is obtained by averaging over all centroids for each sub-aperture of one run. To get the local wavefront tilts, the resulting null position frame is subtracted from each single centroid frame. By looking for individual centroids that are noisy, spots at the edge of the pupil, which are suffering from vignetting (see Figure 4.16), can be removed in order to avoid their contribution to the reconstructed wavefront. By means of an open loop reconstructor Z^{-1}, slopes are converted into amplitudes of Zernike modes. Starting from

$$W(x_j) = \sum_i a_i Z_i(x_j) \tag{4.12}$$

Figure 4.15: Image of the SHS reference setup. From left to right: Pickup mirror collimator lens, SH-lenslet and objective with Retiga 2000 CCD-camera.

where x_j denotes the absolute null position x_i, y_i of each sub-aperture combined in a single vector and assuming that the absolute angular spot movement of each sub-aperture α_{x_j} is proportional to the first derivative of the local wavefront, one can write:

$$\alpha_{x_j} = \frac{\partial W(x_j)}{\partial x_j} = \sum_i a_i \frac{\partial Z_i(x_j)}{\partial x_j} \tag{4.13}$$

The angular movement of each SH-spot can then be calculated from the measured spot movement c_{x_j} on the CCD, by following $\alpha_{x_j} = c_{x_j}/f_{SH}M$. f_{SH} denotes the focal length of the SH-lenslets and M the magnification factor between the pupil plane and the micro-lens plane (see equation 1.33). Equation 4.13 may be re-written in a more compact matrix notation:

$$\overrightarrow{\alpha} = Z \cdot \overrightarrow{a} \tag{4.14}$$

where $\overrightarrow{\alpha}$ denotes the combined slope vector of the spot movements in both directions. Z is a matrix, given by inserting the absolute null positions of each sub-aperture x_j into $\sum Z_i(x_j)$. By multiplying with the inverse matrix Z^{-1}, one can deduce directly from the slope measurements the Zernike coefficients, since:

$$\overrightarrow{a} = Z^{-1}\overrightarrow{\alpha} \tag{4.15}$$

A standard method to calculate the reconstructor Z^{-1} is by means of singular value decomposition, which gives automatically a least square solution of the considered set of equations. Based on that, wavefronts composed of the first 28 Zernike polynomials have been reconstructed out of the SH-spot pattern.

4.5.2 CCD-synchronization

To record wavefront phase deformations with the SHS and PIGS/z-invariant CCD-camera simultaneously, they have to be synchronized. A pulse generator, creating a series of suitable 5V TTL pulses to define integration time and time lag between two successive frames, was used to operate both CCDs via their external trigger capability. The camera synchronization in all experimental runs has been monitored by shadowing the pupil for several exposure cycles at every 100 frames. Figure 4.17 depicts a plot to investigate the timing accuracy within four typical runs. Each plot was deduced by summing all counts within each raw image of the SHS-data and the z-invariant data, respectively. Then both sets were normalized to this frame in the SH-data set of maximum total intensity. While for run 2 and 3 the timing is stable within the given resolution of 100ms, it is varying in run 4 and 5. Figure 4.18, which

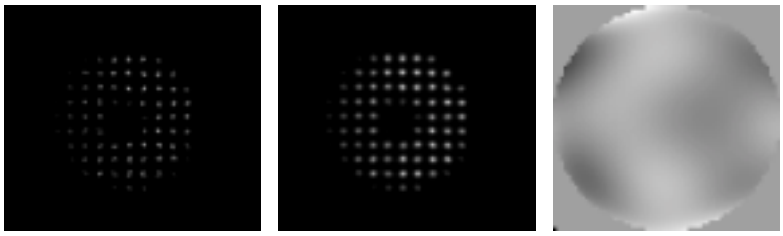

Figure 4.16: Reference data from the SHS conjugated to a NGS. **Left:** Resulting SH spot pattern of a single exposure. **Middle:** "null position" frame, obtained by averaging all centroids of one single run. Sub-apertures close to the left edge of the pupil are vignetted. **Right:** Reconstructed wavefront composed out of Zernike polynomials up to the 28th mode. The sampling of the wavefront is 64px × 64px.

zooms in the sequence of synchronization marks of run 5, shows an increasing relative shift of up to 3 frames between the relative synchronization markers. Comparing the evolution of the relative shift, one encounters a systematic scheme, since in both cases (run 4 and run 5) the shading event is recorded later by the SHS-CCD. Hence, for the further data evaluation a high synchronization accuracy cannot taken for granted. A deeper investigation and a more accurate tracking of this effect in order to counteract it, was due to the limited temporal resolution between two successive images not possible.

4.5.3 Relative Pupil Orientation

Incoming light rays from the RLGS and the NGS are processed via two different optical paths, which contain a different number of reflective surfaces (see Figure 4.1). Additionally, both CCDs-cameras are rotated randomly with respect to each other. This results in a different orientation of the recorded pupil-images. For a proper evaluation and a final comparison of reference data and z-invariant data, one needs to trace this effect by further calibration measurements in order to counteract it properly. To determine the relative orientation between two pupil images, one needs at least two distinguishable reference positions. This can be ensured, e.g by placing an arrow into a pupil plane before the beam is split in the respective optical systems. This results in pupil images, characteristically shaded at corresponding areas (see Figure 4.19). While Figure 4.19 (left) shows frames obtained with the PIGS/z-invariant WFS camera for two different arrow positions (A and B), Figure 4.19 (middle) depicts corresponding images taken with the SHS camera. The arrow position in both sets will coincide (see Figure 4.19 (right)) when the SH images become transposed followed by a rotation of 180°. For a final comparison of z-invariant and SH-data, one has to consider that arrows visible in the z-invariant pupil images are formed by light rays, not reflected by the rod (see section 4.6). Hence to ultimately superimpose both data sets, a further rotation by 180° has to be taken into account.

4.6 Limitations of the PIGS On-sky Experiment

This section wants to give a complete overview about differences and further complications between the laboratory and on-sky experiment. It summarizes already mentioned issues but focusses also on problems not discussed so far.

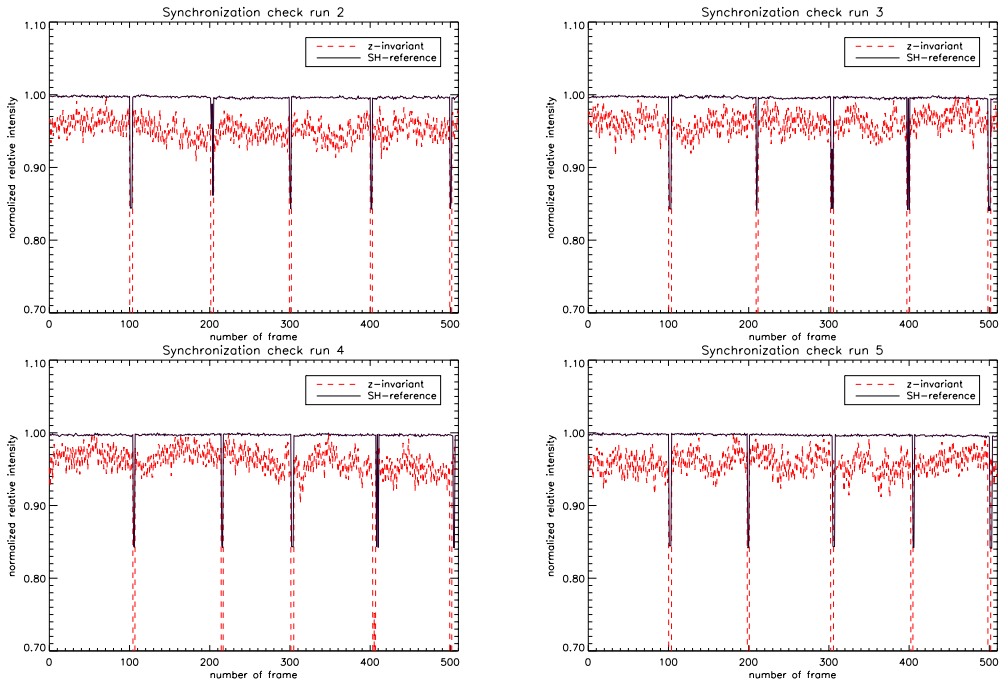

Figure 4.17: Results of CCD synchronization measurement for 4 runs (temporal resolution 100ms). While run 2 and run 3 show a stable synchronization within the sampling accuracy, run 4 and run 5 are characterized by systematic de-synchronization. Hence a stable synchronization cannot be taken for granted in the further data evaluation.

4.6.1 Limited Photon Return of the RLGS:

The limited output power of the RLGS resulting in low guide star brightness is one major limitation. It impacted the experiment negatively in multiple ways:

- **Long exposure time:** To accumulate enough photons in order to reach a sufficient signal to noise ratio, a minimum integration time of the PIGS/z-invariant WFS-camera of at least 30ms was required. This quantity may be compared with the atmospherical coherence time τ_0, which gives a measure for the temporal de-correlation of an induced wavefront phase error by the ground layer turbulence. It can be estimated following the Taylor hypothesis. Evaluating $\tau_0 = r_0/v_{wind,GL}$ by inserting for r_0 the recorded median seeing during the runs (≈ 1.0") and for the wind speed values according to Table 4.4, one gets $\tau_0 \approx 10ms$. As a result, the required integration time of the CCD exceeds by far the atmospherical coherence time τ_0 for the ground layer. A strong smoothing of high order spatial frequencies within a single frame has to be taken into account for the further data analysis. Thus both WFSs are only sensitive to the lowest order Zernike modes.

- **Rod alignment** To obtain sufficient S/N on the detector, the sampling of the z-invariant CCD was decreased by applying an internal 8x8 binning mode. While this does not affect the sensing process itself, it induced a necessary change in the performed alignment strategy. This yields a less accurate positioning of the rod with respect to the optical axis and leads to non negligible distortions of the re-imaged pupil. In principle this effect may be counteracted by estimating induced warping effects due to mis-alignment as it was done in the laboratory. This, however, was not possible for

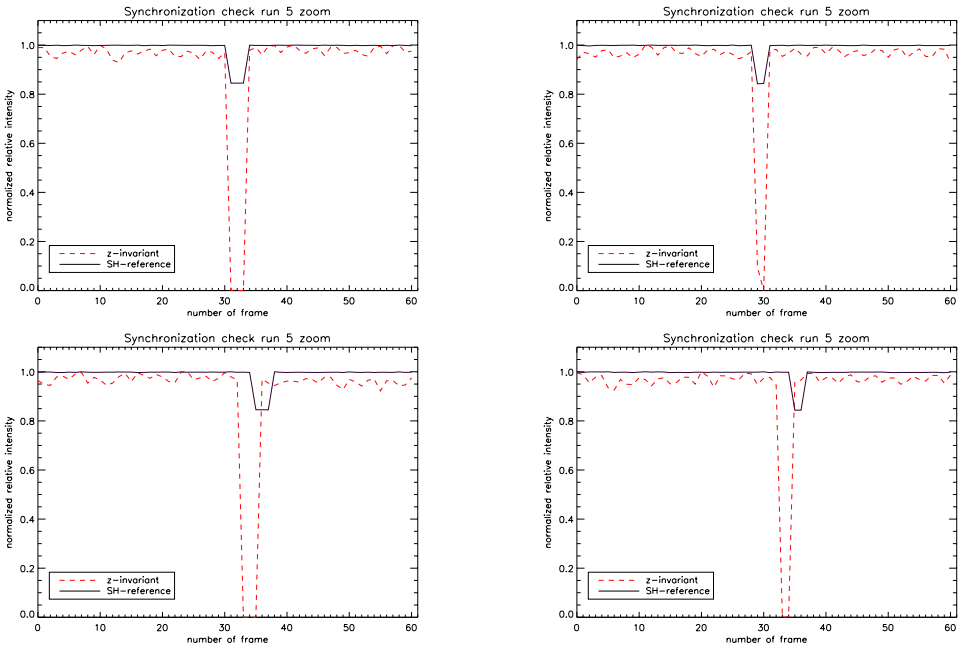

Figure 4.18: Zoom into four synchronization reference marks of run 5: The SHS-camera is characterized by a systematic synchronization error up to three images. This corresponds to 300ms.

the on-sky experiment, due to the insufficient number of reference marks available to compute the warping parameters imposed by the limited resolution (see Figure 4.16).

4.6.2 Accuracy of Camera Synchronization

The inconsistent synchronization between the two WFS cameras in combination with the low temporal resolution of the performed synchronization reference measurements are a further limitation. Their low temporal resolution is explained by the not fast enough read-out capability of SHS-camera. For a future PIGS experimental run, a shorter temporal lag of the order of the atmospherical coherence time has to be aspired. Moreover a different approach to measure the synchronization accuracy at much higher temporal resolution is strongly recommended to trace any systematics of synchronization errors.

4.6.3 Anisoplanaticity Effects

The low focussing altitude of the RLGS impacts in two ways the experimental run limiting the expected correlation:

- **Angular anisoplanatism:** Imposed by a low focussing height, there was no possibility to check in a reliable way the angular separation of the RLGS with respect to the NGS reference source. The RLGS in all previous test runs was exclusively operated at a focussing altitude of $20km$. In this case, scientific cameras, optimized for an imaging of infinite distant objects, still can be used to check the angular separation of NGS and RLGS. In the case of a focussing altitude of 4km, the RLGS was blurred to an angular spot size of 10" (in accordance to the expected perspective elongation discussed in section 2.1). This even exceeded the size of the isoplanatic patch. Therefore the RLGS

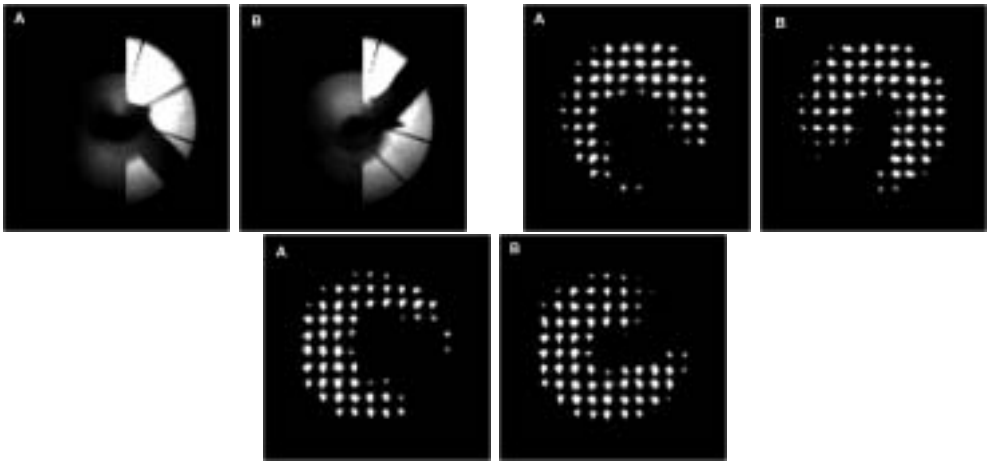

Figure 4.19: Pupil images showing two different marking points (A,B) on the pupil. While the first two sets depict the initial positions of the marking arrow on the z-invariant and SH-data, the third set shows the position of the marking arrows in the SHS-data after performing a suitable transformation

has been positioned with respect to the NGS by eye using a d=30mm binocular. This offered a maximal angular resolution of 3". Although this approach gave a better positioning accuracy, it still implies a non negligible angular anisoplanatism.

- **Conical anisoplanatism:** Caused by the low focussing height, light rays originating at the RLGS, exclusively probe the lowest parts of the atmosphere. Although different C_n^2 profiles of La Palma verify (see Figure 4.2) that the turbulence is mostly (up to 80%) concentrated close to the ground, there is no guarantee that this is true for the observing night. The SLODAR facility close to the WHT was not in operation and hence no turbulence profile measurements are available taken during the experimental run.

4.6.4 Absolute Angular Spot Size of the RLGS

Preliminary tests done by the WHT group predicted an upper limit of the angular elongation of the RLGS at the sky of 3" (remark: as seen in the conjugated height and not in the infinity focus). Based on that, the used rod diameter and the optical system of PIGS was designed to guarantee sufficient angular resolution. As shown, in the case of a spot size of 3", the sensor offers a sensing capability of 18 distinguishable azimuthal sub-apertures (Table 4.3.1). Unfortunately, due to several technical problems, the laser could not be properly focussed. During the operational run the RLGS exceeded at least an angular spot size of 4". This implies a stronger smoothing and less sub-aperture resolution than expected.

4.6.5 Light from non Gated Heights

A further drawback of the system was a strong light pollution by photons from lower altitudes. These superimposed the sensor signal reflected from the rod. The problem becomes obvious following Figure 4.20. A certain point located at the exit pupil will emit a bundle of light rays, each associated with a certain height emerging from the RLGS. Assuming now a point Q at the re-imaged pupil, it will not only be composed of rays coming from P. Also rays originating at lower heights below the gating altitude (coming from P', a point symmetric

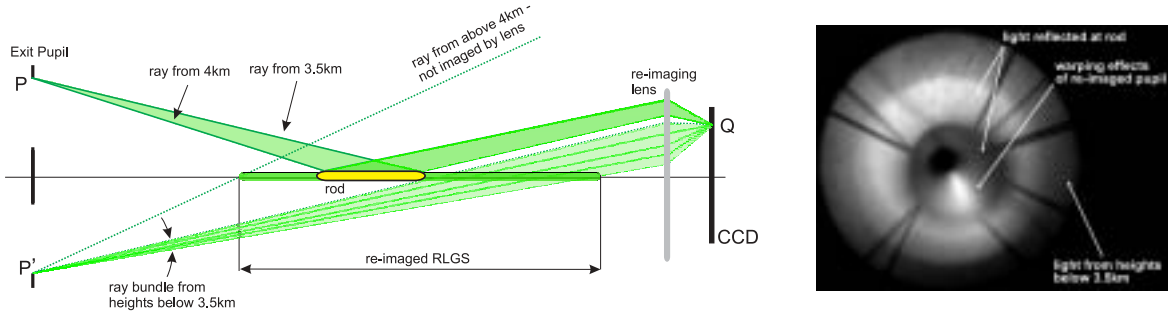

Figure 4.20: Effect of a Rayleigh Laser guide star: Light rays from non gated lower altitudes below 3.5km enter the optical system and will be re-imaged by the camera optics. Such rays superimpose the signal reflected from the rod, as it is shown in a typical pupil image obtained with the CCD (right).

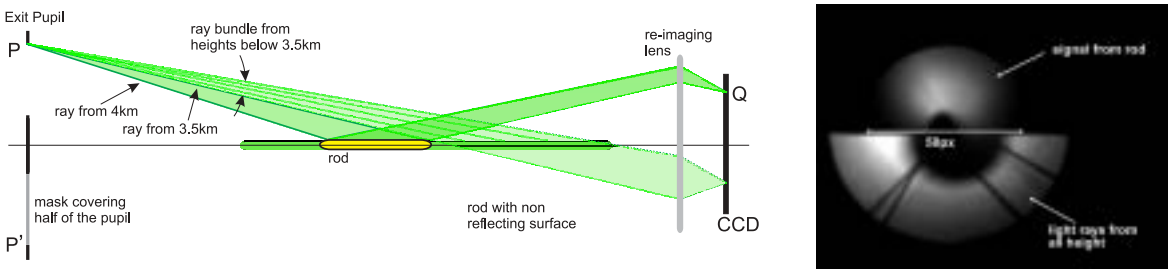

Figure 4.21: Effect of a mask placed at the exit pupil blocking light from half of the pupil. Rays from lower altitudes can no longer superimpose the reflected rays from the rod. As a penalty one looses the information over half of the pupil.

to point P) will contribute to its illumination. While the gating range of the rod was at least several 100 meters, this is a factor 10 lower than the focussing altitude of the RLGS. Thus, rays from non gating heights will dominate the signal recorded on the detector. This amount is further increased, assuming a higher cross-section in lower atmospheric altitudes. Ultimately this leads to an illumination pattern at the re-imaged pupil as depicted in 4.20 (right). Light rays of altitudes above the gating range are a minor threat, since they are eliminated by choosing a proper diameter of the re-imaging lens.

In principle there exist two ways to counteract this issue. Both solutions are depicted in Figure 4.21 and Figure 4.22. One way to block light rays from non-desired heights is by conjugating a rod with non reflective surface to such altitudes. This is an ideal solution, since it guarantees that exclusively light rays from the gated height form the signal recorded by the detector. Due to time constraints during the experimental run at La Palma, a manufacturing of such a blocking device was not feasible and an alternative method has been pursued.

Photons from lower altitudes may also be blocked by placing a mask in the exit pupil, which is covering half of the pupil (see Figure 4.14, (middle)) but this leads to a loss of information of the phase error over half of the pupil as shown in Figure 4.21 (right).

4.7 Data Reduction and Results

Most preferable is an evaluation in analogy to the laboratory experiment, where phase aberration of simultaneously recorded reference data and z-invariant data have been directly

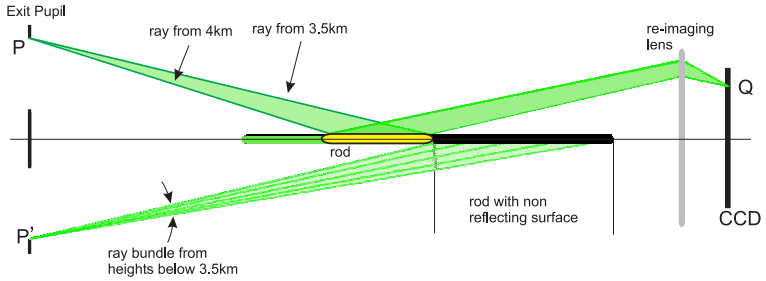

Figure 4.22: Principle setup of a system in order to avoid light from non gating height entering re-imaging optics

cross-correlated. However, as intensively discussed, the on-sky experimental data suffers from strong limitations and uncertainties. In comparison to the laboratory experiment three major differences may be encountered:

- **Evaluation of a dynamical system**: While the laboratory experiment was performed in a static approach, on-sky measurements are characterized by a dynamical evolution of induced phase errors. Thus, for a proper evaluation, a reliable and accurate timing of reference and z-invariant CCDs would be required.
- **Anisoplanaticity effects**: Provoked by anisoplanatism effects, reference and z-invariant WFS cameras do only partially see the same wavefront errors.
- **Proper tracing of warping effects**: Induced warping effects due to mis-alignment could not be properly measured and were therefore not accurately traced and compensated.

Summing up all temporal and spatial limitations, one expects a rather weak correlation for a direct comparison of wavefronts.

Hence a different approach to evaluate the data has been followed. An ideal way to overcome all discussed limitations is to trace the movement of the turbulent ground layer, which should be visible in both data sets. As a result, both are treated in this way as to be quasi-static, since dynamical effects are visualized. A quasi-static approach imposes further advantages such as:

- Timing errors of the WFS-camera do not play a role anymore.
- Complexity of the entire data reduction process is reduced.
- Additional error sources resulting from uncertainties in the measurement process or anisoplanaticity effects can be neglected.

Moreover both data sets can be processed independently, since no direct cross-correlation is done. However - as a major limitation of this approach - only a somewhat more qualitative confirmation of the functionality of the z-invariant sensing device can be given.

4.7.1 The Taylor Hypothesis

But how can the movement of the ground layer be extracted from both data sets? The idea was to disentangle the complex structure of turbulent atmosphere by assuming that it is

composed out of several thin layers. Each layer is inducing independently phase errors on the incoming wavefront. Moreover the validity of the Taylor hypothesis is assumed, which states the "Frozen Flow" model. "Frozen Flow" is a static approach and means that each turbulent layer is treated as to be infinitely extended having a well defined spatial energy spectrum of phase fluctuations. The spectrum does not vary in time. For an observer located at the telescope, it seems that the wavefront moves over the telescope pupil (of diameter D) according to its wind speed v_{wind} and wind direction φ (see Figure 4.23). If one compares now two pupil images (each recording the current shape of the wavefront) taken with a time lag $\Delta t < v_{wind}/D$, they will be characterized by a similar pattern shifted with distance $s = v_{wind} \cdot \Delta t$ (see Figure 4.23 (right)). The total wavefront phase error is a

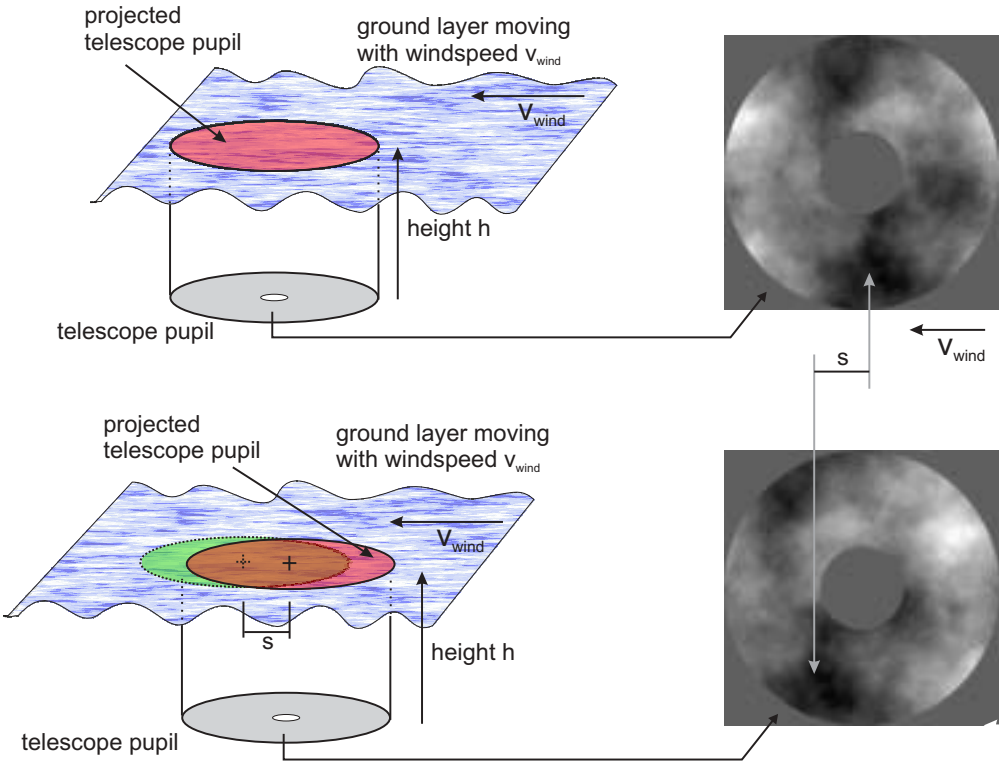

Figure 4.23: Taylor hypothesis and "frozen flow": A phase error as seen from the telescope pupil is generated by a single static turbulent layer of infinite extent (left). Such a layer moves over the telescope pupil with wind speed v_{wind}. This leads to a shift s of the recorded wavefront OPD. Two pupil images taken with time lag Δt show this shift.

result of an integration over all turbulent layers. Hence, the generated spatial structure of the wavefront phase error is a superimposition of all layers weighted with their turbulence strength, moving in different directions and at different wind-speeds. In general as shown by almost all turbulence C_N^2 profiles (see for instance Figure 1.3 or Figure 4.2) the ground layer incorporates the main amount of turbulence and will therefore feature the dominating contribution to the resulting wavefront phase error. Additionally, as a rule of thumb, the ground layer wind speed is by a factor 2-3 lower than the speed of high altitude turbulent layers. Hence it is easier to detect and clearly distinguishable.

4.7.2 Tracing the Movement of the Ground Layer

Ground Layer Movement in the SHS-Data

Investigations were first focussed on the reference SH-wavefront data. Since the SHS is conjugated to a NGS and hence sensitive to all turbulent layers, its data provide a way to verify if the ground layer is dominating. As a reference, independently recorded wind speed data (taken by a weather station at the roof of the WHT-dome) has additionally been evaluated. Table 4.4 depicts the obtained wind-speed data confirming quite stable wind conditions during the considered experimental runs.

date	time [UT]	wind speed [m/s]	wind direction φ [°]
2003-11-10	23:45:00	8.90	247.10
2003-11-10	23:50:00	9.20	234.90
2003-11-10	23:55:00	9.60	237.30
2003-11-11	**00:00:00**	**9.80**	**249.20**
2003-11-11	**00:05:00**	**10.70**	**242.20**
2003-11-11	**00:10:00**	**9.10**	**239.90**
2003-11-11	00:15:00	10.20	235.60
		9.9 ± 0.8	**244 ± 4.84**

Table 4.4: Wind data obtained from a weather station at the roof of the WHT. The data verifies that conditions during the observing run remained stable. Rows denoting relevant wind-speed and wind direction, as measured during the experimental run, are marked in bold font. The last line gives the average values all three experimental runs.

Each turbulent layer, moving with a speed $v_{wind,i}$, impacts independently on the dynamical phase error evolution within the pupil. To make this visible, two consecutive wavefront images (reconstructed from the SH-data) of one run have been shifted over a defined range of spatial offsets $\Delta x, \Delta y$ with respect to each other. The intersecting area (See Figure 4.24) of both pupils has then been correlated (see section C). To reduce computational time, the necessary spatial range to correlate was estimated from the wind speed data. The cross-correlation procedure results in a set of n-1 frames, which were averaged, to obtain the averaged wind speed and wind direction characteristics for one run. At first glance one would expect a pattern as depicted in Figure 4.24 (lower right), which is immediately characterized by intensity maxima, determined by the intrinsically hidden wind characteristics.

However, the resulting cross-correlation pattern (see Figure (4.25 (left)) is obviously dominated by an almost Gaussian shaped intensity distribution localized around the center of the image. This does result from the autocorrelation of the intrinsically hidden circular shape of the pupil, which becomes maximized at a spatial lag 0. In order to remove it, the autocorrelation pattern of all n frames of one run has been computed and all resulting frames have been averaged (Figure 4.25 (middle)). Before the autocorrelation pattern finally can be subtracted, it has to be normalized to the central peak intensity of the cross-correlation pattern. A subtraction ultimately results in the characteristic wind-speed pattern as seen in Figure 4.25 (right).

Figure 4.26 presents the resulting intensity distribution patterns obtained from three SH-data sets. In accordance to previous expectations all sets show a strong peak, which originates in the movement of ground layer turbulence. Moreover, occasionally several weak and strongly smoothed side peaks can be encountered (one is marked with a red arrow in

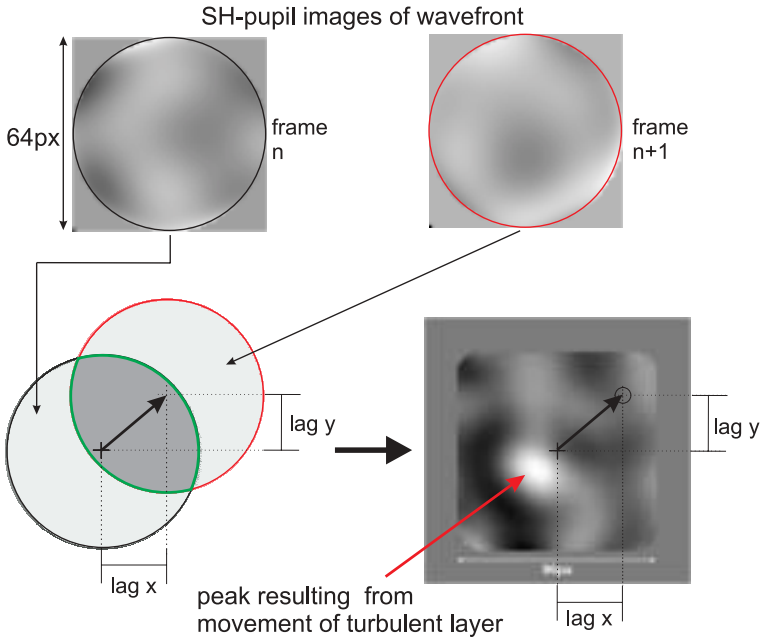

Figure 4.24: Tracking the ground layer movement. A moving wavefront can be made visible by correlating the intersection of two successive wavefront images over a given range of spatial offsets Δx, Δy. Maxima within the resulting intensity pattern (lower right) give a measure of the wind speed and wind direction of corresponding layers.

Figure 4.26 (left)) originating from turbulent layers located at higher altitudes. In the cross-correlation frames, the distance of each peak from the center is an absolute measure for the wind speed and can be recomputed into units of m/s. The absolute distance and its angular position has been computed by determining the vector of the center of gravity of the peak with respect to the image center (at an accuracy of roughly one pixel RMS). The reconstructed wavefronts of the SH reference data set were sampled over a 64 $px \times 64$ px grid. Hence, the maximum reachable resolution over the pupil is: $4.2m/64px = 0.066$ m/px. The temporal lag between two frames was fixed to 100ms, which finally leads to a wind speed resolution of 0.66 $m/s/px$. Following Table 4.5 the deduced values for wind speed and wind direction in all three runs are in good agreement to values determined at the weather station of the WHT. The slight systematic discrepancy of 18° of both measured wind directions may be understood considering the limited angular positioning accuracy of the SHS camera.

Ground-layer Movement in PIGS/z-invariant Data

In a next step it was investigated if the z-invariant sensor is able to track the ground layer turbulence movement. Caused by practical limitations (as discussed in section 4.6.5) the z-invariant setup provided only a sensing capability over roughly 60% of the entire pupil (see Figure 4.27 (left)). Hence, to extract the useable signal reflected by the rod, a proper mask has been created (see Figure 4.27 (middle)). To retrieve information about the second azimuthal derivative, according to equation 2.21, the ratio $(I - I')/I$ for each frame of a run has been calculated and multiplied with a suitable radial weighting function ϱ. While I' is the measured intensity distribution of the re-imaged pupil in each single frame, the reference intensity I was estimated by computing the average of all frames of one run. Although the measured intensity pattern of the z-invariant sensor is proportional to the second azimuthal derivative of the wavefront phase error, this does not affect the resulting correlation pattern. This may

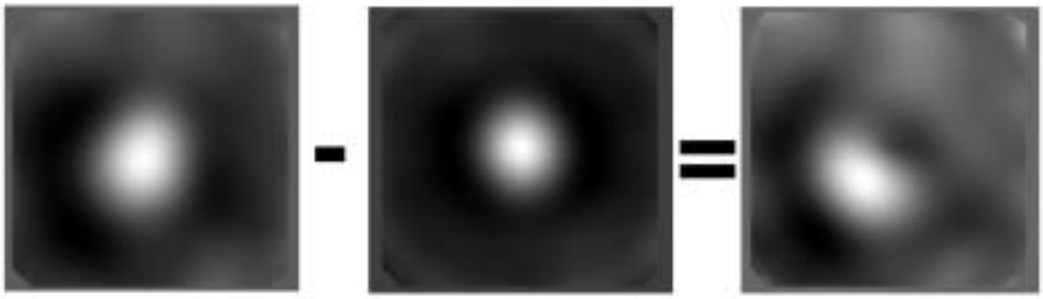

Figure 4.25: Procedure to extract the signal of turbulent layers out of a cross-correlation pattern. The resulting cross-correlation pattern is dominated by the autocorrelation of the intrinsic hidden circular shape of the pupil (left image). In order to counteract this effect, the autocorrelation (middle) has been calculated. After normalizing it to the cross-correlation pattern it has been subtracted from the latter leading to the right pattern.

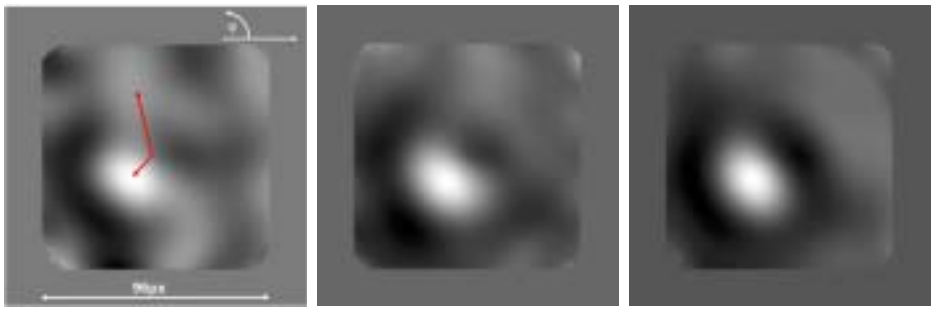

Figure 4.26: Cross-correlation pattern to track wind speed and direction of turbulent layers as derived from SH-reference data. Although the SHS is sensitive to all turbulent layers along the line of sight, the strong dominance of the ground layer is remarkable.

be understood following the principle of operation of correlation analysis, which is sensitive to similarities of patterns. Since the second azimuthal derivative is computed from the wavefront phase error pattern by a set of linear operations, the resulting shape of the second azimuthal derivative pattern is unique. To extract now from the deduced $\Delta I/I$-intensity pattern the correlation peaks induced by the movement of the ground layer turbulence, the data has been processed as in the case of SH-data sets. The resulting correlation peak-pattern for the corresponding three runs are depicted in Figure 4.28. They show dominating peaks originating from the ground layer. Their elongated shape in comparison to the corresponding SH-data (Figure 4.26) is explained by residual azimuthal warping effects due to the rod misalignment. In order to compute from the peak position absolute values for wind speeds, in a first step the size of the re-imaged pupil was determined in pixels. Therefore an artificial ideal circular-shaped pupil has been created and superimposed with the resulting z-invariant pupil (see Figure 4.27 (right)). The sampling grid of the pupil defined by the z-invariant WFS camera data could be determined as $50\ px \times 50\ px$, which leads to a resolution of $0.084\ m/px$ and ultimately to a wind speed resolution of $0.84\ m/s$. Deduced wind-speed and angular orientation for the z-invariant data is listed in Table 4.5. Both, the derived wind-speed and direction is in very good agreement with the reference measurements performed with the weather station and with the SHS.

Figure 4.27: Left: Resulting signal in the PIGS/z-invariant WFS-camera after placing a half mask into the exit pupil. The upper half shows flux resulting from reflections by the rod. Middle: Binary mask to highlight parts of the re-imaged pupil, which are suitable for further data processing. Right: The diameter of the re-imaged pupil was estimated in pixel by superimposing a circular pupil.

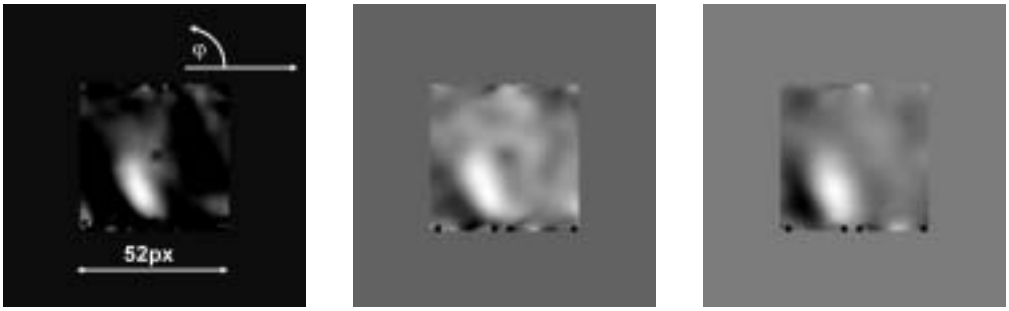

Figure 4.28: Cross-correlation pattern to track wind speed and direction of the ground layer in the z-invariant data. The data is already properly oriented in order to superimpose it with the SH data. The elongated shape of the correlation peaks may be induced by incorrect azimuthal warping effects.

	SH-reference		**z-invariant**	
run	windspeed[m/s]	direction φ[deg]	wind speed[m/s]	direction φ[deg]
A	8.7	217	10.3	244
B	9.6	220	8.8	236
C	10.4	228	10.2	243
avg	**9.6 ± 0.85**	**222± 5.6**	**9.7± 0.84**	**241± 4.3**

Table 4.5: Resulting windspeed and wind direction of ground layer derived from SH data and z-invariant data set. Both are in good agreement to independently obtained wind measurements done at the top of the WHT dome.

Chapter 5

The PIGS WFS Concept - Conclusions

PIGS is a novel wavefront sensor optimized for next generation AO-facilities at ELTs, operated with sodium laser guide stars. Due to the finite distance and vertical extent of the laser beacon, conventional WFS techniques (without any upgrade) will be limited by severe constraints such as for instance perspective elongation. This leads to a dramatic loss of correction quality and hence overall AO-performance.

The PIGS sensor is a pupil plane WFS concept, measuring the second derivative of atmospherically induced wavefront phase errors. It consists of two independently working sensing devices, which overcome by different approaches the problems mainly linked to the vertical extent of the LGS. A mask composed of concentric slits is able to synthesize wavefront aberrations in the radial direction. In this way the LGS is projected virtually to infinity. For the sensing process only rays originating from a certain direction are used. As a 3-d z-invariant sensing device, the reflective rod is able to measure simultaneously distortions of incoming light rays from different altitudes.

Due to its design as pupil plane wavefront sensor, PIGS can be implemented or later upgraded within each AO-instrument with low technical efforts. Hence it is a real alternative to engineering approaches such as temporal gating. This is even more the case since the PIGS sensor is in terms of light-throughput at least a factor of 4-10 more efficient than temporal gating. In this context and induced by the selection characteristic of the slit-mask, angular gating as a novel gating technique has been introduced. Although the light-throughput in the temporal gating approach may be increased by applying fast re-focussing techniques, this attempt implies huge technical and engineering challenges, which are not required for the angular gating.

Although PIGS is able to counteract limitations such as perspective elongation and defocussing issues, several other problems pointed out in section 2.1 like ray skewness, FoV limitations and conical anisoplanatism effects, are not solved. Such effects arise mainly due to the proximity of the LGS with respect to the telescope and can only be overcome by increasing the focussing altitude of the laser beacon.

According to the results obtained in chapter 3, the principle of the z-invariant concept, as one part of the PIGS wavefront sensing concept, has been proven under laboratory conditions. In chapter 4 the z-invariant concept was qualitatively verified under realistic conditions "on-sky". Since more quantitative results were limited by a number of constraints induced by the operational status of the RLGS and several further practical limitations, another open loop experiment is recommended. The WHT will be equipped in the near future with a by far

improved laser system (a solid state disk laser from ELS, Darmstadt) providing as nominal output 30W leading to a 9th magnitude guide star at a focussing height of 20km. Such a guide star will be up to 3 magnitudes brighter as the present RLGS, relaxing constraints imosed by limited photon throughput. This enables:

- shorter integration time of the WFS camera
- an adoption of a more simplified and accurate alignment procedure as discussed in 3.2.2
- an on-sky test of the sensing capability of the slit mask as radial WFS
- reference measurements with the LGS

The latter is possible since the laser can be focussed to higher altitudes. Hence, effects such as perspective elongation are reduced. Since conical anisoplanatism would be reduced, this would also be a method to improve the expected cross-correlation in the case of comparing the NGS reference measurement with PIGS data. Although a higher focussing altitude would not conserve completely the geometrical ratio given at an ELT, this could be counteracted by an increase of the gating depth, leading to a further gain in terms of light throughput.

In a follow-up run, all complications encountered during the last WHT observational run, such as backscattered light from non-gated heights, can be eliminated by using proper auxiliary components. For instance according to section 4.6.5, one can block light from not gated heights below the conjugated gating altitude of the rod by introducing a non-reflective rod painted black behind the rod-sensor. This guarantees a re-imaging of the signal reflected by the rod exclusively.

Following the theoretical considerations in chapter 2, the slit mask is limiting the light efficiency of the PIGS sensor, since it rejects most of the incoming photons. A further disadvantage is that the gain of the slit mask is a fixed, non-adjustable quantity leading to less flexibility of the overall sensing concept. Furthermore the gain is a function of parameters, which can vary within an observation night. Hence it has to be pointed out that the mask and at least also the reflective rod have to be seen as representatives of two novel WFS-classes, where mask and rod are at least *one* possible practical solution. For sure there exists a variety of different ways to adopt both the z-invariant and Inverse Bessel Beam concept for WFS purposes in more optimized ways. This implies also a further investigation of several important quantities like scintillation or error propagation. Both could influence the sensing capability of the PIGS sensor.

Chapter 6

Direct Imaging of Exo-planets with NACO-SDI

6.1 Introduction

Exactly 10 years have passed since Michel Mayor announced the first detection of an extra-solar planet orbiting 51 Pegasi, a G5V star (Mayor and Queloz (1995)). This was the discovery of the first planet, around another star. Up to now 167 exo-planets (August 2005) in 136 systems have been detected. The detection of a possible planetary mass companion to a young brown dwarf (Chauvin et al. (2004)), as well as the detection of planets in at least 18 multiple systems (Marcy et al. (2001)) implies that planets exist in a huge variety of configurations.

6.2 Definition of a Planetary Object

But when is a planet a planet? While the boundary between stars and sub-stellar objects like brown dwarf is quite well defined, the exact definition of when an object can be called a planet was lacking in the past. The Working Group on Extrasolar Planets (WGESP) has developed a Working Definition of a "planet", subject to change as we learn more about the population of very low mass companions. A planet is defined as follows:

- Objects with true masses below the limiting mass for thermonuclear fusion of deuterium (currently calculated to be 13 Jupiter masses for objects of solar metallicity) that orbit stars or stellar remnants are "planets" (no matter how they formed). The minimum mass/size required for an extrasolar object to be considered a planet should be the same as that used in our Solar System.
- Substellar objects with true masses above the limiting mass for thermonuclear fusion of deuterium are "brown dwarfs", no matter how they formed nor where they are located.
- Free-floating objects in young star clusters with masses below the limiting mass for thermonuclear fusion of deuterium are not "planets", but are "sub-brown dwarfs" (or whatever name is most appropriate)

6.3 Indirect Measurement Techniques

In recent years, several techniques have been established in order to track planets around their host stars and determine basic physical parameters. Up to now almost all suspected planetary mass companions have been detected by indirect methods. This section gives a brief introduction on the most common techniques like Doppler-shift based radial velocity measurements or transit events, but mentions also some of the less common, but also already successful techniques like microlensing or pulsar timing.

6.3.1 Radial Velocity Measurements

The by far most common approach to search for exoplanets is by radial-velocity measurements. Planetary companions leave behind a tellable trace when orbiting their host stars, which originates in Newton's 3rd law. Both, the planet and its host star orbit around their common center of mass. Hence the star oscillates along the line of sight, which can be recorded by evaluating the change in radial velocity via Doppler-shift as derived from high resolution spectra. A relation between the radial velocity and the physical parameters like planetary mass follows from Kepler's 3rd law:

$$(a_{star} + a_{companion})^3 = GT^2(M_{star} + M_{companion})/4\pi^2 \tag{6.1}$$

where M denotes the mass, a the semi major axis, T the orbital period and G the gravitational constant. The barycenter-equation gives:

$$M_{star} \cdot a_{star} = M_{companion} \cdot a_{companion} \tag{6.2}$$

and the orbital velocity v_{star} can be expressed as:

$$v_{star} = 2\pi \cdot a_{star}/T \tag{6.3}$$

Considering moreover that one is only able to measure the projected radial movement of the star, namely:

$$v_{star} sin(i) = v_{radial} \tag{6.4}$$

one can deduce a relation for the lower limit of the companion mass:

$$M_{companion} \sin(i) = v_{radial} \left[\frac{M_{star}^2 \cdot T}{(2\pi) \cdot G} \right]^{1/3} \tag{6.5}$$

Equation 6.5 shows that the radial-velocity increases for more massive companions in a close orbit.

In order to detect the weak radial velocity signal resulting from companions, radial velocity measurements have to be taken at a very high precision. This is achieved for instance by using Iodine absorption cells. When the light of the target passes the cell, the inserted gas leads to additional absorption lines, which are used as wavelength reference. This results in a stability of the spectrograph corresponding to velocities of the order of 2m/s. Jupiter leads to a radial-velocity signal of 12.5 m/s for the sun, and hence is relatively easy to detect. Earth, however, leads to a signal of only 0.04m/s, which is way below the detection limit of radial velocity surveys. Although almost all exo-planets have been found via this technique, it is limited to massive companions with relative short orbital periods. Moreover according to equation 6.5, a direct mass determination is not possible, as the method gives only a lower limit. Recently, Gliese 876 d, an earth like planet ($M \sin(i) = 8M_{Earth}(\pm 0.003)$) has been discovered by Rivera et al. (2005). It is the least massive exo-planet identified thus far around another star.

6.3.2 Transit Measurements

Monitoring transit events is another possibility to search for extra-solar planets. If a companion passes in front of the star within the line of sight with respect to an observer, this results in a gentle dimming of the host star, corresponding to a drop in the light curve. As the planetary system has to be seen edge on, the probability for a transit event is small. The probability of a transit event is a function of stellar radius and distance of the companion for a random distribution of orbits: $p = r_s/a_{comapanion}$. Transit measurements are an interesting detection method, since in addition to the orbital period of the companion, also its radius can be derived. The drop in flux in the light curve yields:

$$\frac{\Delta F}{F_s} = \frac{A_{companion}}{A_{star}} = \frac{r^2_{companion}}{r^2_{star}} \tag{6.6}$$

Here F_s and ΔF denotes the average flux of the target and the decrease during the transit. A and r define visible surface and radius of companion and star. Additionally the orbital velocity of the companion can be deduced from the duration of the transit event to: $v_{planet} = 2r_s/t_0$. Flux decrease $\Delta F/F$, transit duration t_0 and transit probability p for Earth and Jupiter are listed in Table 6.1. The combination of transits and radial-velocity measurements yields

	Earth	Jupiter
$\Delta F/F$	$8 \cdot 10^{-5}$	10^{-2}
t_0	13h	30h
p	$5 \cdot 10^{-5}$	10^{-5}

Table 6.1: Typical parameters (Flux decrease $\Delta F/F$, transit time t_0 and transit probability p) for Jupiter and Earth transits

in addition to orbital parameters also physical quantities like the absolute mass (since the inclination is $\sim 90°$), or the average density of the companion. Moreover one might be able to detect tracers of the exo-planet atmosphere (Charbonneau et al. (2002)). However, due to the small transit probability, up to now only five transit events has been confirmed (for instance HD 209458, Charbonneau et al. (2000)). Transit events can be mimicked by instabilities in the stellar atmosphere or rotating star-spots. This leads to a high rate of false detections. To minimize these error sources, mainly FGM stars are monitored, which are supposed to be "quiet". Although in principal jovian transits can be detected with small telescopes below 1m (TRES-I, Alonso et al. (2004)), photometric accuracies limit observations to $\Delta F/F \geq 10^{-3}$, mainly due to the temporal variability of the atmospheric extinction coefficient. Therefore space missions like COROT and KEPLER are planned with the aim to reach a photometric accuracy of $\Delta F/F = 10^{-5}$. Early 2005 the Spitzer space telescope detected light from two exo-planets by inverting the transit method. Here the light of a hot exo-planet orbiting around a host star (Charbonneau et al. (2005), Deming et al. (2005)) was measured by comparing the integrated flux of the system before and during a secondary eclipse (planet behind star).

6.3.3 Astrometry

The induced movement of the host star by a companion around the common barycenter can also be detected by astrometric techniques. For an observer located at a distance of 10 pc, Jupiter for instance causes an astrometric oscillation of the Sun of 500 μas over 12 years. This requires high astrometric accuracy, which from the ground can only be achieved using interferometry or else with dedicated space observatories. The PRIMA facility, a long base

interferometer instrument for the VLTI, will be able to achieve an astrometric accuracy in the mircoarcsecond regime. It will carry out an astrometric search program for planetary companions. For comparison, the ESA satellite HIPPARCOS achieved an astrometric accuracy of up to 1mas, while the future space mission GAIA (which is planned to be launched in 2011) will be able to get an accuracy of 20 μas at V=15 mag and 200 μas at V=20 mag. Astrometric observations will directly yield the mass of the orbiting companion. Up to now GL 876b is the only planetary companion with a firm mass determination based on astrometric measurements (Benedict et al. (2002)).

6.3.4 Microlensing

"Normal Lensing" is a well known method to detect faint objects on the cosmological scale. Similar to an optical lens, light may also be focussed by gravity. Its focussing quality depends on the "Einsteinradius", which is a measure composed of the mass of the focussing object and the distance between observer and the lens as well as the lensed object. A maximized Einstein radius leads to optimized efficiency of the lens. Let us consider a star, which acts as a gravitational lens: An observer located close to the focus will detect an increase of flux, when the star passes the lensed object. The shape of the light-curve depends on the exact path and the mass distribution of the lens. If the star is orbited by a companion, this leads to strong secondary peaks in the light curve. Mircolensing has the potential to detect planets down to several earth masses (Wambsganss (2004)). Although at least two planetary companions have already been detected (Bond et al. (2004)), the detection of such events requires long term and continuous monitoring of a large number of stars. Unfortunately microlensing events are "one time events", which do not repeat.

6.3.5 Pulsar Timing

Surprisingly, the first planetary mass companions with 2.8 and 3.5 Earth masses have been found orbiting the pulsar PSR 1257+12 (Wolszczan et al. (1992)). Pulsar timing follows the same idea as radial velocity measurements and astrometry. It is based on the wobble of the host object around the common barycenter due to a planetary companion. This leads to periodic fluctuations in the arrival time of the pulsar signals. Such fluctuations can be recorded with high precision, in particular since pulsars are highly stable clocks.

6.4 Direct Imaging and the Limitations

As a major limitation, all techniques described above provide only rather indirect information on the planetary companions. The indirect methods yield orbital parameters and in the case of transits basic physical quantities like average density, mass or chemical properties. A direct imaging detection is highly desired, in order to directly analyze photons originating from the planet. Direct imaging detections yield:

- Absolute mass of the companion in systems with arbitrary orientation, by tracking the orbital movement of the planet.
- Properties of the planetary surface and its atmosphere from polarimetric measurements.
- Chemical composition of atmosphere and planetary temperature from spectroscopy and photometry.

Such studies will provide answers to the question if our solar system is unique. Moreover by tracing the atmospheres of exo-planets for biomarkers like O_3, humans will achieve the ultimate goal to search for life outside the solar system. However, the large contrast ratio between host star and planetary companion, and their small angular separation as seen by an observer are the main obstacles for direct detections.

6.4.1 Distance between Companion and Star

Since planets are expected to have formed in protoplanetary disks with typical diameters $\sim$ 100 *A.U.* (Brandner et al. (2000)), planets are expected to orbit their host stars with semi-major of at most several tens of A.U. E.g Jupiter, as observed from a nearby star at a distance of 10 pc, would never be more than 0.5" from the sun. Close the diffraction limit, observations (as e.g provided by a high order AO-system) yield angular resolutions of $\sim$ 50 mas at 8m class telescopes in the H-band. Hence two objects of the same brightness, separated by $\sim$ 5 *A.U.*, could be resolved out to a distance of $\sim$ 100 pc

6.4.2 Contrast ratio between companion and star

Planets are in general both smaller and cooler than their host. As a first estimate, their flux can be derived using Stefan-Boltzmann's law:

$$F = 4\pi\sigma R_p^2 T_{eff}^4 \tag{6.7}$$

Here σ denotes the Stefan-Boltzmann constant, R_p the radius of the radiating spherical black body and T_{eff} the effective temperature. With an equilibrium temperature of 279 K and a radius of 6373 km, Earth emits about $2 \cdot 10^9$ less flux than the Sun, whereas Jupiter ($T_{eff} = 152$ K, $\mathrm{r_P} = 143,000$ km) is about $2 \cdot 10^8$ fainter than the sun. For rather old planets T_{eff} is the equilibrium temperature, resulting from the balance between stellar radiation absorbed on the day side of the planet and flux re-emitted by the whole planetary surface. It is defined by:

$$T_{eq} = 279 \cdot L_*(1-A)^{1/4} d_p^{-1/2} \text{ [K]} \tag{6.8}$$

where L_* denotes the luminosity of the central star in solar units, A the Bond albedo of the planet and d_p the distance between the star and planet in AU. Since the planet remains always cooler than the host star, the contrast between star and planet is larger at shorter wavelength. This explains why the contrast ratio decreases from 10^9 in the visible to 10^6 in the infrared for a star and gaseous planetary companion. Fortunately the situation is better for young terrestrial and gas giant planets. Internal energy originates in residual fusion processes for brown dwarfs and/or excess from gravitational contraction energy or earlier stages of jovian planetary evolution (Black (1980)). For instance, Jupiter's internal energy can be computed from: $T_{int} = T_{eff}^4 - T_{eq}^4 \cong 95°$K. In the case of brown dwarfs, the internal energy is higher, which improves the contrast to 1:1000 making direct detection much easier. For example GL 229B ($T_{eff} < 1200K$), the first brown dwarf companion found around a nearby star, was already detected 10 years ago by Nakajima et al. (1995) and Oppenheimer et al. (1995). In the H-band it is 8.9mag fainter than its host star GL 229A (M1V). The detection was facilitated by the relatively large angular separation of 7.6" (44 A.U. at a distance of 5.8pc)

6.5 Why Simultaneous Differential Imaging?

According to the previous section, direct imaging detection imposes severe constraints in terms of resolution and contrast capabilities of the used instrument. Endeavors to prove

the existence of planetary companions with direct ground based observation methods have been carried out even before the invention of AO. NIR speckle interferometry for instance is a technique offering resolving capabilities beyond atmospherical limitations (Henry and McCarthy (1990)), where one can reach contrast ratios up to $\Delta m_H \sim 4mag$ for a 7mag bright star at the diffraction limit. This technique is limited to very bright targets and rather modest contrast ratios. The most promising approach to image planetary companions from the ground is by modern AO-based NIR-cameras at $8 \ldots 10$m class telescopes. While higher mass sub-stellar companions like brown dwarfs have already been directly detected, the imaging of planetary mass objects ($m < 13M_J$) remains still a major technological challenge. Assuming a perfectly correcting AO-system at such a telescope facility and imposing data quality only limited by photon noise, simulations verified that one would easily detect the Jupiter-Sun-system at a distance of 10pc (see Figure 6.1). Although AO attenuates aberrations of an incoming wavefront, the resulting images still suffer under the imperfectness of correction leading to residual speckles. Several papers were dedicated to discuss the significance of speckle noise in (partially corrected) AO-PSFs (Angel et al. (1995), Langlois et al. (1998), Racine et al. (1999)). Angel for instance commented that - assuming an AO system delivering almost aberration-free PSFs close to a Strehl-ratio of 1 - a 8 m class telescope is able to reach a contrast ratio of $\Delta m \sim 20$ for an integration time of 1hr. Racine et al. (1999) discussed the reachable S/N ratio in the case of AO-Systems providing a moderate correction with Strehl-ratios below 70% in the H-Band. In such case the S/N of a faint companion depends on following residual noise components:

$$(S/N)^2 \simeq (S^2 F_c^2)/var(\text{halospeckle} + \text{halophotons} + \text{corephotons} + \text{readnoise} + \text{skynoise}) \tag{6.9}$$

Here $S^2 F_c^2$ denotes the ratio of the companion signal. It has been shown that speckle noise - due to the nature of its origin - is correlated noise and therefore has to be investigated and treated differently as for instance photon noise. Furthermore, the contribution of residual speckle noise in partially corrected AO images was estimated by simulations (see Figure 6.2). According to these, depending on the brightness of the host star, speckle noise can dominate the variance of the shot noise by several magnitudes within the non-corrected seeing halo of bright stars. This leads to severe limitations, since a faint companion cannot be distinguished or identified within such a pattern and hence has to be brighter than this noise level. One possibility to reduce speckle noise and increase the contrast is by suppressing light from the host star using coronographs (Sivaramakrishnan et al. (2001)). Diffraction limited coronographs covering the inner $\sim 3-4$ Airy rings are, however, only effective for high Strehl-ratios ($> 80\%$). Another technique to suppress the contribution of halo speckles was proposed by Racine. By subtracting two frames taken simultaneously in two narrow-band filters closely adjacent in wavelength, speckles automatically cancel out, since both images exhibit similar speckle features. This technique is ideally suited for direct imaging of faint giant exo-planetary companions, since cool ($T_{eff} < 1500$ K) (Fegley et al. (1996)) sub-stellar objects show strong methane absorption bands (see Figure 6.3 and (Rosenthal et al. (1996)). Hence assuming over the total wavelength regime an almost constant flux of the host star, the companion will provide a signal in a frame taken outside the band, while a second frame taken within the band is almost flux-free. Since both data-sets were obtained at slightly different wavelength bands, before subtraction, they have to be re-scaled to a common λ/D scale in order to remove first order chromatic effects, which lead to residual RMS wavefront phase errors given by:

$$\sigma_W = 2\pi\delta(1/\lambda_1 - 1/\lambda_2) \tag{6.10}$$

Here δ denotes the residual RMS wavefront error in nm and λ the corresponding wavelengths. In principle the subtraction process should also cancel out all flux from the host star and make the companion visible. The prospects for a detection become optimized by concentrating on

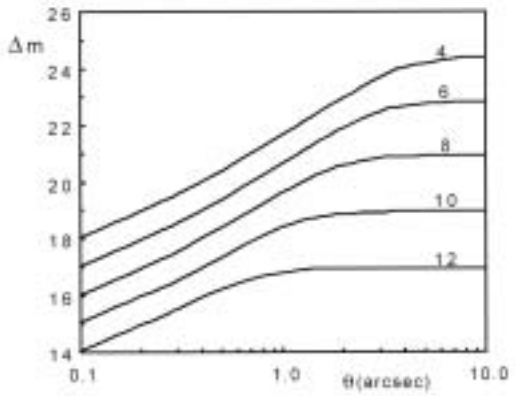

Figure 6.1: Simulation showing the theoretical achievable contrast ratio in magnitudes at an 8 m telescope as a function of angular separation. The detection thresholds are computed for a 3σ significance assuming an integration time of 10000 seconds. A Sun-Jupiter system at 10pc distance ($m_* \simeq 4$, $\Delta m \approx 20$ and separation $\simeq 0.5$" could just be detected. The graph has been taken from Racine et al. (1999)

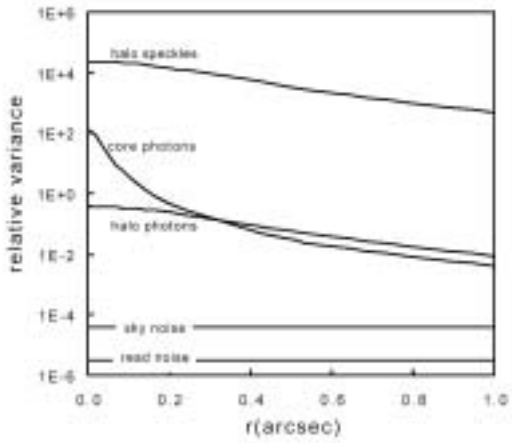

Figure 6.2: Relative importance of different noise components assuming a partial correcting (Strehl-ratio=0.5, $\lambda = 1.6\mu m$) AO-system at a 3.6m telescope for good atmospherical conditions. Obviously the residual noise is still strongly dominated by halo speckles, which hampers the identification of potential candidates. Graph has been taken from Racine et al. (1999)

close ($< 50pc$), young stars where the companion is still self-luminous. In practice, however, Simultaneous Differential Imaging only attenuates speckle noise, but does not remove it completely. A possible reason for this effect has been discussed in Marois et al. (2000). To achieve image quality close to the photon noise limit it was proposed to extend the SDI method by a double subtraction. The latter removes second order speckle noise originating from chromatic effects and leads to an additional speckle noise attenuation of a factor of 100. Hence one needs a third image recorded at a further wavelength band to give:

$$dd = d_{12} - kd_{13} = (I_1 - I_2) - k(I_1 - I_3) \tag{6.11}$$

It is assumed that the three images I_1,I_2 and I_3 are taken at wavelengths $\lambda_1 < \lambda_2 < \lambda_3$. d_{12} and d_{13} denotes the single SDI for two different wavelength bands, respectively. k is a scaling factor to weight each pixel with the mean ratio of d_{12}/d_{13}

6.6 Simultaneous Differential Imaging with NACO

6.6.1 NACO-SDI Instrumental Design

To provide Simultaneous Differential Imaging at the VLT, the high resolution camera NACO has recently (2003) been upgraded with this mode. The SDI mode (see Figure 6.4) consists of a F/40 camera system offering a plate scale of 17.25mas/px to provide Nyquist sampling at $1.6\mu m$. It is equipped with a special 4-quadrant filter placed directly in front of the focal plane. The entire filter is composed of three adjacent narrow band filters each of 25nm FWHM, which are transmissive at center wavelengths of $1.575\mu m$, $1.60\mu m$ and $1.625\mu m$, respectively. Two quadrants cover the edge of the methane absorption band at $1.6\mu m$ (see Figure 6.3). Two Wollaston prism rotated by 45° with respect to each other are mounted

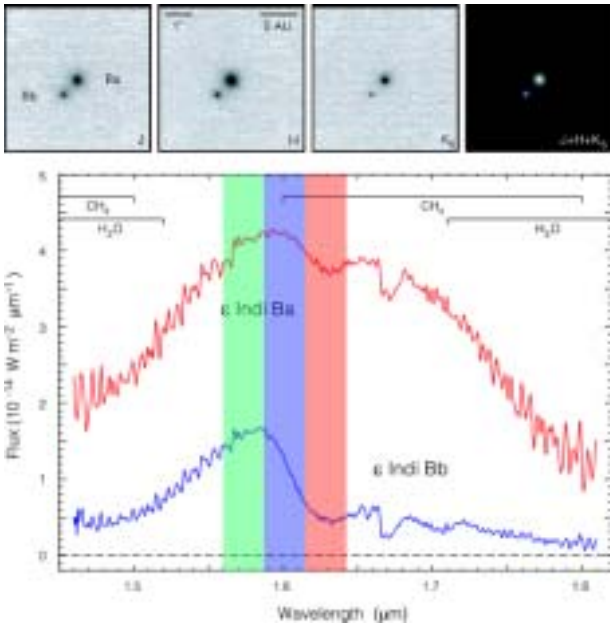

Figure 6.3: Images in J, H and K-band (top) and H-band spectra of Eps Ind Ba (red curve) and Eps Ind Bb (blue curve) a T1-T6 binary dwarf system superimposed with the NACO-SDI filter-set (Filter FWHM 25nm). While Eps Ind Ba remains almost constant in flux, Eps Ind Bb shows a strong methane absorption leading to a drop in flux of 90%. This image was taken from McCaughrean et al. (2004)

in the CONICA Grism/polarizer wheel. They split the incoming light of the NACO pupil into 4 independent beams. This way frames at different wavelength bands are obtained simultaneously. In order to fit the complete setup into the given space, the pupils are focussed by a lens triplet. The optical components were optimized to introduce only imaging errors within the diffraction limit. This ensures that differential static aberrations between the four channels do not dominate. To constrain the FoV and avoid overlap of the different FoV of each filter, a 5" × 5" mask has been placed in the focal plane wheel before the pupil is divided. The SDI focal plane mask did rotate by 43° relative to its nominal position during the complete P74 observing run (see Figure 6.5). As a consequence of the rotation, the effective FoV was limited to 2.7" × 3.7" (Lenzen et al. (2004)).

Since August 2004, CONICA is equipped with a detector array (Aladdin3 InSb $1024px \times 1024px$, physical pixel size $27\mu m$, $4e^-$ readout noise) sensitive over a wavelength range from $0.8\mu m$ to $5.5\mu m$. The detector supports a hardware-based on board-averaging of images. The user has the possibility to define the integration time for a frame (DIT). A second parameter (NDIT) allows to define the number of images to be averaged. Hence the ultimate S/N-ratio of the final image is defined by the total integration time of $DIT \cdot NDIT$. A typical resulting NACO-SDI raw-image is depicted in Figure 6.6. This image has been contrast enhanced in order to make the edges of the focal plane mask visible.

6.6.2 Double SDI with NACO

NACO-SDI was originally designed to follow the idea by Marois of a double subtraction. This approach, however, is based on assumptions valid only for high Strehl-ratios in the H-band, where second order chromatic effects may become dominant. Marios neglected effects like

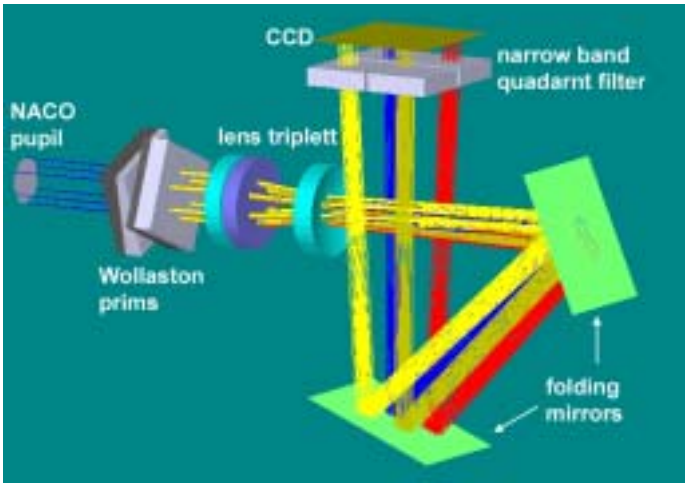

Figure 6.4: NACO-SDI principle of operation. Light from the NACO pupil is split by two 45°-rotated Wollaston prisms into 4 beams of full aperture. A lens triplet focusses the light on the detector through a 4-quadrant filter. Not shown here is the foal plane mask, inserted in an intermediate focal plane within NACO, to constrain the FoV .

non common path aberrations. The latter play in the case of NACO-SDI a major role and dominate by far the residual speckle noise after performing single SDI. This can be shown by estimating the resulting RMS wavefront phase error for both effects. NAOS typically provides in the H-band a Strehl-ratio of $25\% - 30\%$, resulting in a residual RMS of the OPD of $300nm$. According to equation 6.10 this can be recomputed to a residual chromatic RMS phase error in radians of $\sigma_{chrom} = 3.7 \cdot 10^{-2}\ rad$ for $1.625\mu m$ and $1.575\mu m$.

Zernike mode	4	5	6	7	8	9	10	11	12	13	14	15
RMS error[nm]	15.7	1.2	1.4	18.0	9.0	0.5	1.9	8.7	4.2	4.0	3.6	6.7

Table 6.2: RMS of non common path aberrations between the filter images for $1.575\mu m$ and $1.625\mu m$ for each Zernike coefficient given in nm. The data was kindly provided by Markus Hartung.

To estimate the induced non common path aberrations, results from the NACO-SDI commissioning report have been evaluated. In this context, non common path aberrations between the different filters have been measured for the Zernike modes 4 to 15. Table 6.2 depicts the relative aberrations between filters for $1.575\mu m$ and $1.625\mu m$ in terms of RMS. According to equation 1.21 the total induced RMS of the residual phase error can be estimated as $0.113\ rad$. Interestingly, this is already almost a factor 3 higher than first order chromatic effects. A detailed calculation of the residual wavefront phase RMS of second order chromatic effects has never been done, but might be quite useful. Its contribution to the total phase error can be estimated following Racine et al. (1999). The median of radial PSF intensity fluctuations induced by first order chromatic effects is determined by:

$$\frac{\Delta I}{I} \simeq 2\sigma^2 \frac{\Delta\lambda}{\lambda} \tag{6.12}$$

while second order effects are approximated via:

$$\frac{\Delta I^2}{I} \simeq (3 - 2\sigma^2)\sigma^2 \frac{\Delta\lambda_{12}\Delta\lambda_{23}}{\lambda^2}. \tag{6.13}$$

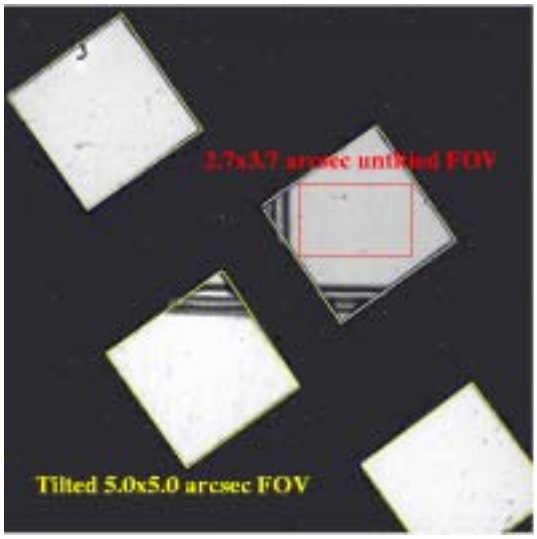

Figure 6.5: NACO raw image superimposed with focal plane mask the FoV. For the P74 observing run the 5" × 5" mask was tilted for 43° restricting the FoV to 2.7" × 3.7". With the focal plane mask the detector flat field has been inserted. This image was kindly provided by ESO.

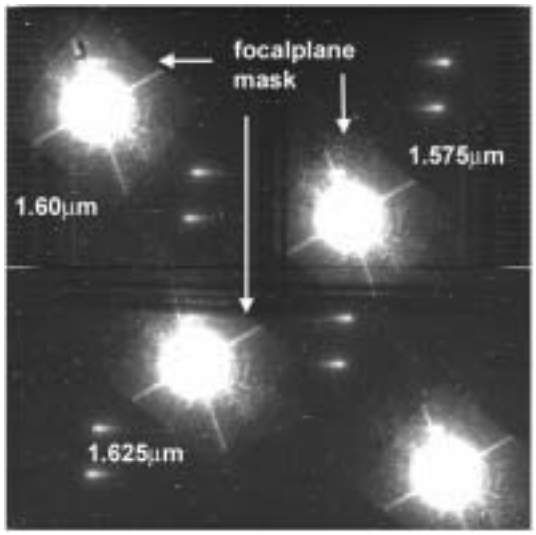

Figure 6.6: NACO-SDI raw image of Eps Eri. The image has been contrast enhanced to visualize to focal plane mask. Also visible are the borders of the quadrants of the filter. Shown are also the corresponding central wavelengths of the filter for each image of the star

In the case of NACO-SDI $\Delta\lambda_{12} = \Delta\lambda_{23}$. By inserting equation 6.12, equation 6.13 can be re-written in terms of first order effects:

$$\frac{\Delta I^2}{I} \simeq (3/2 - \sigma^2) 2\sigma^2 \frac{\Delta\lambda_{12}\Delta\lambda_{23}}{\lambda^2} = (3/2 - \sigma^2)\frac{\Delta I}{I}\frac{\Delta\lambda}{\lambda} \tag{6.14}$$

Assuming now $0 < \sigma < 1$ as the usual limit for the Maréchal approximation and inserting for $\Delta\lambda$ and λ typical values of 25 nm and 1600 nm, it becomes obvious that second order effects are much smaller than first order chromatic aberrations. This is true as long as the filter bandwidth is much smaller than the imaging wavelength (as it is the case for NACO-SDI). Hence, the double subtraction for NACO-SDI has been optimized to eliminate residual non-common path aberrations. Practically it is performed by subtracting two frames taken at different rotation angles of the instrument. While speckles as residuals from static non common path aberrations remain at the same position, a companion rotates on the detector according to the defined rotation angle. In this way non-common path aberrations are removed, while the signal of the companion is still conserved. Moreover this method offers the possibility to identify potential candidates more easily, since in the resulting difference image a companion should be visible as a bright and a dark peak separated by the chosen offset angle of the instrument.

6.7 Epsilon Eridani

The Main scope of the astronomical work in this thesis was in implementing a complete data reduction pipeline to process NACO-SDI data. The pipeline was calibrated by means of a particular target in order to estimate and verify the capability (in terms of reachable detection limit) of the SDI method. The target - Epsilon Eridani (Eps Eri) - is regarded as

one of the most promising candidates for a direct detection of a planetary companion. Hence its observation can be considered as a benchmark for the science potential of NACO-SDI.

Eps Eri (V=3.73mag) is a K2V star located at a distance of 3.22pc. Infrared excess detected with IRAS traces the presence of circum stellar material (Aumann (1988)) and a dust ring centered on Eps Eri with a radius of 18" (60 AU) was detected by SCUBA 850μm observations (Greaves et al. (1998)), which is interpreted as a young analog to the Kuiper belt. Its major/minor axis ratio indicates an inclination $\approx 25°$, which is in good agreement with the 30° inclination of the stellar equator deduced from the radiation transfer analysis of high resolution optical spectra (Saar and Osten (1997)). The age of Eps Eri has been estimated to less than 1 Gyr based on the high level of stellar activity (Soderblum and Dappen (1989)). More recently, Ammler et al. (2003) analyzed high resolution spectra of the partially filled in H_α line of Eps Eri and concluded that Eps Eri is a likely member of the Ursa Major Association with an age of only $\approx 200\ Myr$. In 2000, Hatzes et al. (2000) reported the radial velocity detection of a long-period planet orbiting Eps Eri. The analysis of their 20yr monitoring campaign indicates the presence of a companion in a 6.9 yr orbit with a semimajor axis of 3.4 A.U., an eccentricity of 0.6, and $M \sin i = 0.86\ M_J$. If one assumes that the companion is orbiting in the plane of the disk, the mass of the exo-planet is $M = 2\ M_J$. Astrometry with HIPPARCOS and ground based observations also indicate the presence of a giant planet in orbit around EpsEri. Based on statistically significant differences between long term proper motion as derived from ground based astrometry over the past 200 years, and the short term proper motion as measured by HIPPARCOS over a 3yr period centered around 1991, Wielen et al. (1999) identified a group of so called "$\Delta\ \mu$" binaries. A plausible fit to the astrometric data for Eps Eri indicates an objects in a $\approx 10yr$ orbit with a mass of $\approx 4M_J$, albeit with relatively large uncertainties since HIPPARCOS observations only covered a fraction of the orbit. Re-analysis of the HIPPARCOS data, taking the radial velocity observations into account (Frink et al. (2003)) yield an upper mass limit of $2.5M_J$ for the giant planet around Eps Eri. Black et al. (2000) report on the results of 13yr of ground based monitoring with the Multichannel Astrometric Photometer, indicating the presence of a giant planet with a mass of $\approx 1.4 \pm 0.5M_J$. Hence both radial velocity and astrometric measurements provide strong and rather independent evidence for the presence of a giant planet in orbit around Eps Eri in the mass range of 1.4 to 4 M_J. Because of its young age, proximity to the Sun (3.22 pc), and the relative wide orbit, the giant planet around Eps Eri is the prime candidate for the direct imaging detection of a planet orbiting another star. The direct detection of a sub-stellar companion around EpsEri has previously been attempted by the Hubble Space Telescope (HST) (Schroeder et al. (2000)) and with ground based telescope equipped with AO, but without differential imaging (Oppenheimer et al. (2001), Luhman and Jayawardhana (2003). Both observing strategies were not successful.

6.8 Data Acquisition Sets on EpsEri

All results concerning EpsEri, which are shown and discussed in the following sections, are based on data sets taken on 19/09/2004 between 07:56 UT to 09:35UT. They contained in total 40 images, which were split up in two sets of 20 frames each, taken at instrumental rotation angles of 0° and 33°. Each set consisted of a sequence of 5 dithered frames. After the dithering sequence, the instrument was pointed to an empty region on the sky to obtain sky-frames. The integration time per frame was 0.6s (DIT) and 160 frames (NDIT) were averaged per position leading to a total exposure time of 96s per position. This results in a final exposure time of 32min per rotation angle, and hence is one of the deepest high contrast images ever taken of Epsilon Eridani. The exposure time was chosen such that the

resulting central 8 *px* (0.14") of the resulting PSF of Eps Eri were saturated. This method increases further the signal from the companion. Moreover for IR-observations one desires to be limited by the noise from background photons and not by readout noise. Finally, the potential planet would be too faint for a direct detection in the innermost part of the stellar PSF in any reasonable amount of observing time.

6.9 Data Reduction Pipeline

The pipeline has been developed in IDL following a modular approach, which aims at guaranteeing a clear structure and minimizing maintenance efforts. In this way it is also possible to keep it user friendly and easily accessible for future upgrades. But nevertheless the pipeline offers for the experienced user also the possibility to change and optimize various parameters and gives in this way enough flexibility. In the following a compact overview on the main features of the software and a detailed discussion of the most critical issues of the implementation is given.

6.9.1 The Data Reduction - An Overview

In a first step and quite straight forward, a standard data reduction of each frame is done, performing subtraction of sky-frames, a flat-fielding and multiplication by a defined badpixel mask. Then rectangles are cut around each star and re-scaled to a common λ/D scale. All frames containing images of the target in one filter are arranged into a stack and sorted in ascending order beginning with the image with the highest Strehl-ratio. This is chosen as reference image for the shift and add algorithm, which calculates with sub-pixel accuracy the relative shift between two frames of the same wavelength and registers them. To increase the resulting S/N ratio, an averaging of all frames within one wavelength stack is done. Since the flux of the resulting PSFs is not conserved after the re-scaling procedure, the images additionally become flux calibrated. To remove low spatial frequency modes, all averaged images are filtered by an unsharp-mask filter. Then again the shift and add algorithm is applied in order to subtract one wavelength frame from the other to obtain a single SDI frame. A double subtraction is done by performing single SDI for two different instrument angles (typically 0 and 33 degrees) and subtracting the results from each other in the next step.

6.9.2 Scaling to same Plate-scale

To remove first order chromatic effects and to ensure an accurate subtraction of PSF-core and residual speckles noise, the images at different wavelength have to be re-scaled to the same λ/D-scale. According to diffraction optics the location of the Airy-rings of a PSF and hence also of each speckle is a function of wavelength, which scales with λ/D (where λ is the observing wavelength and D the pupil diameter). This means that at longer wavelengths, flux is spread over a wider area, leading to different shape and smaller peak intensities. This effect has been corrected by performing a geometrical transformation in analogy to equation 3.2 and equation 3.3. Assuming pure radial expansion with a factor k, the resulting transformation can be written as:

$$\rho' = \rho_0 + k\rho \quad \text{and} \quad \theta' = \theta \tag{6.15}$$

ρ and θ denote cylindrical coordinates and ρ_0 the radial offset. By performing a back-transformation to a cartesian coordinate system, the k-dependence of the parameters a_i and

b_i can be defined. By means of cubic convolution interpolation the scaling procedure achieved the highest accuracy. The pipeline scaling algorithm uses as reference the shortest wavelength ($\lambda_{1.575nm}$-image), to which images at all other wavelengths are scaled. Hence, the scaling factors are fixed and defined by the ratio $\lambda_{1.575nm}/\lambda_{1.60nm}$ or $\lambda_{1.575nm}/\lambda_{1.625nm}$ depending on the considered wavelength bands, respectively. Since this performs a pure radial scaling in a second step, flux conservation has to be ensured. Assuming that all flux is distributed within the area of the first Airy-ring, whose radial extent is determined by $1.22\lambda_i/D$, one can deduce the scaling factor for flux-normalization as: $(1.575/1.625)^2$ and $(1.575/1.60)^2$.

6.9.3 Shift and Add Algorithm

Required Shift Accuracy

In order to add up as accurate as possible the peak flux of a companion one has to minimize shift errors, since already small uncertainties in the shift accuracy lead to a further decrease of the already rather weak signal from the companion. A high accuracy is also needed when performing the final Single and Double SDI, to properly cancel out residual speckles. In order to estimate the percentage loss of peak signal in the case of an inaccurate shifting, simulations have been carried out. Hereby an ideal NACO-PSF for a wavelength of $1.6\mu m$ has been used. It was scaled according to the data of Eps Eri to reasonable intensity values of potential planetary objects and several noise sources like photon noise, background and readout noise were added. Repeating this n times (see Table 6.3) leads to a stack of frames, which have been added up in two different ways. In one case all frames were accumulated introducing no shifting error. In the other case, a shift uncertainty s has been simulated by shifting all frames of the stack randomly with a radial shift-error according to a set n of normally distributed random numbers with a FWHM s. Then the ratio between the resulting peak-intensity of shifted and unshifted co-added images has been computed. This procedure has been repeated 50 times and averaged in order to increase the statistical significance. The results of the simulation done according to the parameters listed in Table 6.3 are plotted in Figure 6.7 It shows that a shift accuracy of one pixel would lead to a decrease of peak

n	readout noise	companion peak intensity	sky background
20	4 counts	7 counts	3 counts

Table 6.3: Input parameter for shift accuracy simulations

intensity by 27.1%. In order not to loose too much flux due to shifting errors, the goal of the pipeline was to to reach at least 95% of the maximum peak intensity. This is achieved by a shift precision of 0.2 px.

Accuracy Estimate of Shift and Add Algorithm

For the SDI pipeline, the relative image shift between two selected PSF images has been calculated by computing their respective cross-correlation (see section C). Such an approach is ideal in order to determine a proper shift, since besides the PSF-structure also residual speckles are taken into account when the relative shift is calculated. When correlating two PSFs, the resulting cross correlation pattern features a Gaussian distribution sampled on a grid with one pixel accuracy. To reach sub-pixel accuracy the pattern is fitted by a 2d-Gauss function, where the location of the maximum defines the relative shift.

In order to check whether such a procedure leads to sufficient accuracy or not, a test has been performed using dithered data. A dithering sequence, as performed during the observational run, will lead to a constant offset between two successive frames in all four quadrants. In the case of SDI raw images, the object should, according to the defined offset, show in all filters an equivalent relative shift. Therefore all frames of one wavelength have been cut out in respect to a common center. The relative shift of the PSF between two successive frames has been monitored for different filters by computing the shift via the techniques explained above. The difference between the shifts computed for two different wavelength bands gives a measure of the accuracy of the shift algorithm. The results for the Eps Eri data set, which contains 40 frames in total, are plotted in Figure 6.8. The mean shift error in pixel was deduced as: $0.12px \pm 0.05px$. This verifies that the shift algorithm performs with an accuracy better than the required 0.2px. The fractional shift of the images

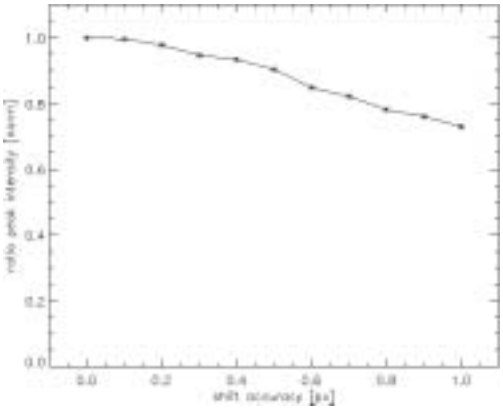

Figure 6.7: Limited shift accuracy results in a decrease of accumulated peak intensity compared to the ideal case. As criteria for the required shift accuracy within the data reduction, at least 95% of the intensity of an companion has to be accumulated coherently. This is achieved with a shift accuracy of 0.2 px.

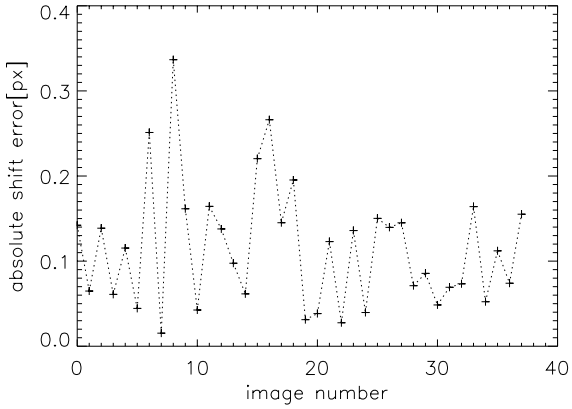

Figure 6.8: Obtained accuracy of the shift-computation algorithm adopted on Eps Eri data sets. It is verified that the shift algorithm performs with an accuracy better than the required 0.2 px.

was performed by cubic convolution interpolation, in order to achieve high accuracy in the sub-pixel regime. To optimize further the shift and add procedure, images were ordered in descending Strehl-ratio to verify that the frame providing the best Strehl-ratio is taken as reference.

6.9.4 Unsharp-Masking

Unsharp-masking is a technique well known for many years in imaging processing. A strongly blurred version of an image is subtracted from the original image in order to enhance local small scale features. This technique is also applicable for exoplanet search, since the signal of the companion "sits" in the wings of the PSF of the host star. In order to increase the detectability of a companion, it is desirable to remove the low order spatial frequency contribution of the AO-PSF. To smooth an image, its high frequency contributions have to be removed by a proper mask. Hence, unsharp-masking in the digital image processing environment is ideally performed in the Fourier domain, since this way the user can exactly determine the shape of the filtering function. Depending on the chosen function, one may damp or completely remove high order spatial frequencies. In this case a Gaussian-

distribution with a FWHM of 1/10px in spatial frequency was used as filter function. The effect of unsharp-masking on an AO-PSF is illustrated in Figure 6.9. As depicted in Figure 6.10, unsharp-masking improves the detection limit by up to 2mag.

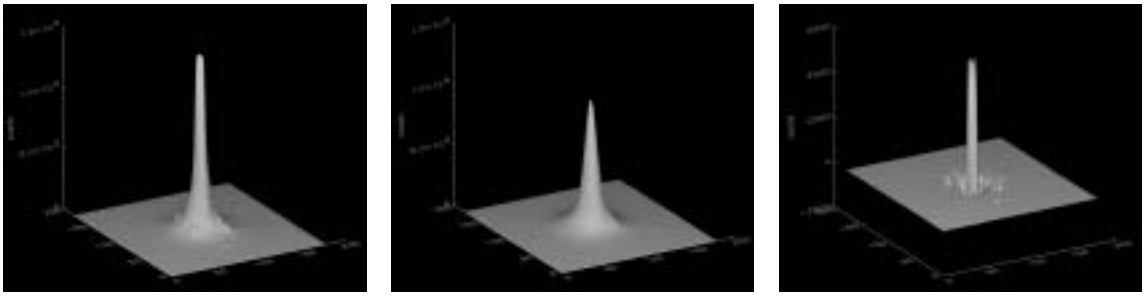

Figure 6.9: Effect of unsharp-masking: By using in the Fourier domain a Gaussian shaped frequency filter, it is possible to generate a smooth PSF composed of low order spatial frequencies. By subtracting the latter (middle image) from the original AO-PSF (left image) high spatial frequency signals, like e.g., the contribution from a planetary mass companion can be enhanced (right image)

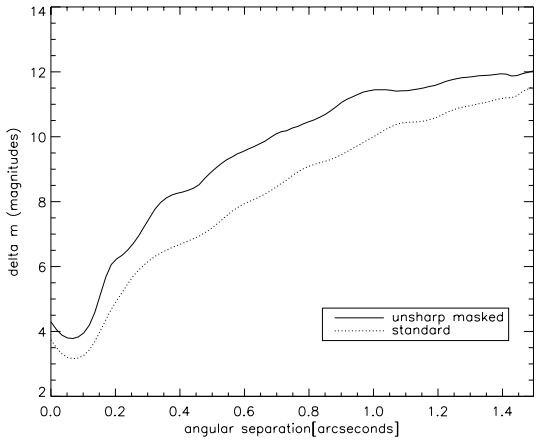

Figure 6.10: Comparison of achievable 3σ detection limits by applying a standard reduction (averaging frames for one filter-band) and a further image optimization by applying an unsharp-masked filter. The latter results in significant improvement of the detection limit within the inner ≤ 1.4" around the star.

6.9.5 Single and Double Simultaneous Differential Imaging

The added frames of the two different wavelength stacks are all registered to the first frame. In order to perform the subtraction between frames of two different filters, their relative shift is determined according to section 6.9.3. Then the image at the longer wavelength is subtracted from the image at shorter wavelength. The latter serves as a reference to define the absolute position of the PSF within the SDI-frame. As discussed above, non-common path aberrations are removed by a second subtraction process. An equivalent number of frames of the target have been taken at two different instrumental rotation angles. For each angular orientation the data has been reduced as described above to provide single SDI images. Both resulting images are still shifted in respect to each other and one needs again the information about their relative shift before performing the double subtraction. Figure 6.11 shows a

typical single SDI frame (left) and two double SDI frames, which were averaged (middle) and median combined (right). From that the importance of double SDI becomes obvious, since speckles resulting from non common path aberration (marked with circles) are eliminated or minimized. The images shown were contrast enhanced by setting the cut levels to ±30 counts.

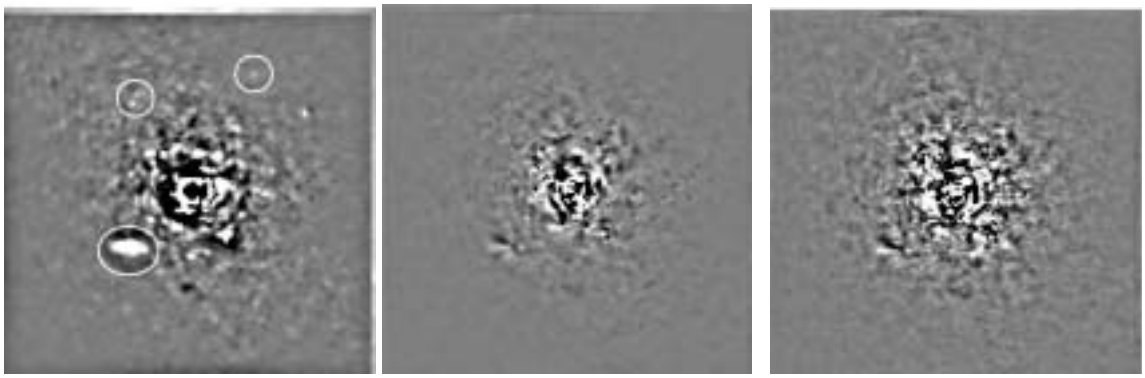

Figure 6.11: Completely reduced single subtracted SDI (left) and double subtracted SDI for averaged (middle) and median case (right). Speckle noise resulting from non common path aberrations (see marked speckles in the single SDI frame) are damped or completely removed by double SDI. While in the averaged double SDI from hot pixels may hamper the detectability, they can be removed by median-averaging the data. This, however, reduces the achievable detection limit. The FoV of all images is 2.8" × 2.8"

The resulting single and double SDI images can now be evaluated by eye to search for any potential candidates. An appropriate method is by displaying the images at sequentially decreasing cut levels. According to Figure 6.13 this techniques leads to an optimized contrast at a certain annular region around the center. In the single subtracted SDI, possible candidates may only be encountered when showing a S/N well above the speckle noise. If not, a definite verification of a potential companion cannot be ensured, since speckle noise exists at all scales as shown in Figure 6.12. In the case of double SDI the search seems to be

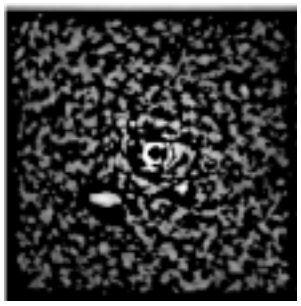

Figure 6.12: Logarithmic scaled Single Differential Imaging frame with cuts set to ±200 counts. Speckle noise is visible at all intensity scales limiting this way the detectibility of companions. The FoV within the image is 2.8" × 2.8"

simplified. Due to the double subtraction, the signal of the companion shows a characteristic double peak in the sense that it is visible at two peaks of inverse sign separated by an angle corresponding to the instrumental rotation with respect to the primary star.

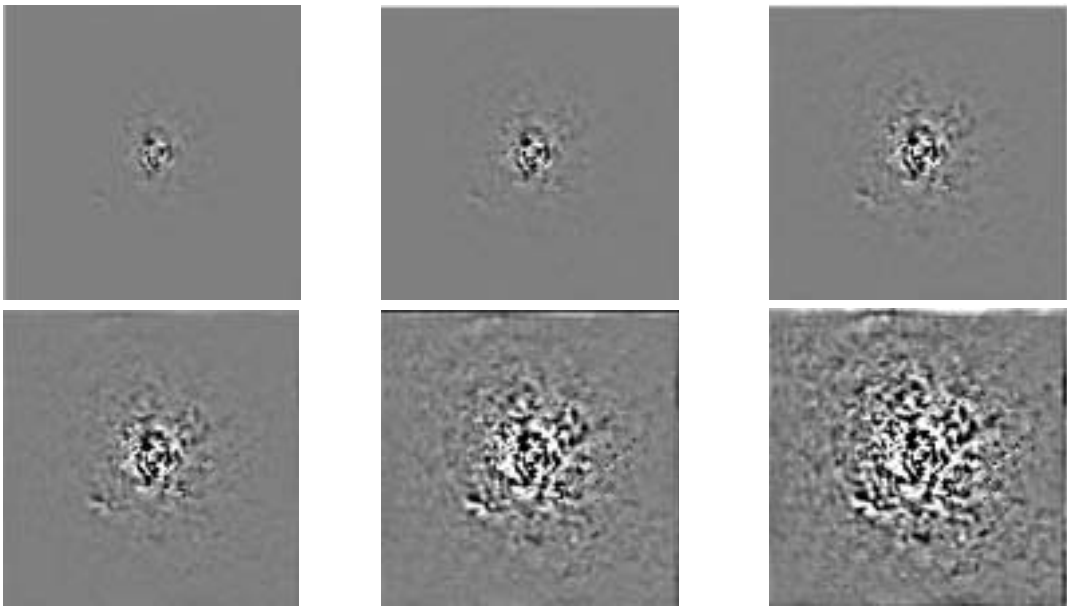

Figure 6.13: Scanning sequence to search for extra-solar planets in double SDI frames. By decreasing sequentially the upper and lower cut levels, it is possible to optimize contrast at certain annular regions. From upper left to lower right the cut in theses images (FoV 2.8" × 2.8") were set to ±200, ±100, ±50 , ±20, ±10 and ±5 counts.

6.10 Achieved Detection Limits for Epsilon Eridani

6.10.1 Estimate EpsEri's Peak Intensity

To estimate the absolute performance of the SDI method and compare it with other techniques, it has to be calibrated first. For this the contrast ratio, i.e the difference in magnitudes between the peak intensity of the potential companion and the host star, has to be estimated. To compute accurately the radial dependency of contrast in respect to the host star, one needs an accurate knowledge of its absolute peak intensity. Unlike one might think at first glance, this is a non trivial issue, since all recorded PSF become only partially corrected by the AO-system and are moreover strongly saturated in the peak. To reconstruct the peak intensity of such a PSF, one has to extrapolate additionally taken images of a non-saturated PSF of the observed star or a different point source. The peak intensity can then be extrapolated by scaling the non saturated PSF according to:

$$I_{p,sat} = I_{p,nonsat} \cdot \frac{DIT_{sat}}{DIT_{nonsat}} \cdot 10^{-0.4(m_{H,obj}-m_{H,ref})} \cdot \frac{S_{I_{p,sat}}}{S_{I_{p,nonsat}}} \tag{6.16}$$

where $I_{p,nonsat}$ denotes the peak intensity of the non saturated PSF and DIT_{sat}/DIT_{nonsat} the ratio of integration times between saturated and non-saturated PSF. When evaluating a non saturated PSF of a different point source, one has additionally to consider the difference in relative brightness of the objects and the peak intensity has to be scaled by $10^{-0.4(m_{H,obj}-m_{H,ref})}$. The factor $S_{I_{p,sat}}/S_{I_{p,nonsat}}$ takes into account that the peak intensity is a function of the Strehl-ratio, which may vary between the saturated and non saturated exposures. However a proper scaling according to the Strehl-ratio is a critical issue, since this requires an accurate knowledge of the correction quality in all data sets. In the case of NACO data, the average correction quality (obtained by monitoring the AO-performance over the last minutes) is recorded by the NAOS real time computer and stored in the header of each frame. It is given in units of coherent energy normalized to K-band. Coherent energy

is as Strehl-ratio a measure of the correction performance and over a wide range (within the Maréchal approximation) equivalent to the Strehl-ratio. Only for small values it differs. Strehl-ratio (and also coherent energy) is a function of wavelength but does not scale linearly. Considering that r_0 is a function of wavelength according to

$$r_0(\lambda_1) \propto \left(\frac{\lambda_1}{\lambda_{ref}}\right)^{6/5} \tag{6.17}$$

and combining this with the Maréchal approximation:

$$E_c \approx S_{\lambda_1} \approx \exp(-\sigma^2) \propto \exp(-(D/r_0(\lambda_1))^{10/3}) \tag{6.18}$$

yields:

$$S_(\lambda_1) = S_{\lambda_{ref}}^{(\lambda_1/\lambda_{ref})^2} \tag{6.19}$$

To estimate the peak intensity in the case of Eps Eri, 8 non saturated PSFs obtained within the same observing run have been scaled according to equation 6.16. Four data sets exhibit moderate to high coherent energy values ($> 20\%$), as recorded by the AO-system, and the Strehl-ratio scaling was applied by taking corresponding values from the image header. The resulting peak intensities are denoted in Table 6.4. For low coherent energy a different ap-

	peak intensity
ref 1	$2.18 \cdot 10^5$
ref 2	$2.33 \cdot 10^5$
ref 3	$2.25 \cdot 10^5$
ref 4	$2.20 \cdot 10^5$
mean	$2.26 \pm 0.06 \cdot 10^5$

Table 6.4: Peak intensities obtained by scaling non saturated PSFs according to equation 6.16. Non-saturated PSFs of moderate to high Strehl-ratio have been used as reference.

proach has been followed by computing the Strehl-ratio numerically from the data. Therefore the enclosed flux, within the non saturated PSF, over an increasing annular region varying from 0.5 to 1.5 arcseconds has been calculated. Then an ideal normalized NACO-PSF was scaled according to the obtained encircled flux resulting in an ideal reference PSF with a Strehl-ratio of 1. The ratio between the peak flux of the non saturated and the ideal PSF gives the Strehl-ratio. The in that way estimated peak intensities for Eps Eri are denoted in Table 6.5

	peak intensity
ref 5	$2.54 \cdot 10^5$
ref 6	$2.15 \cdot 10^5$
ref 7	$1.92 \cdot 10^5$
ref 8	$2.18 \cdot 10^5$
mean	$2.20 \pm 0.25 \cdot 10^5$

Table 6.5: Peak intensities obtain by scaling non saturated PSF according to equation 6.16. Non-saturated PSFs of low Strehl-ratio have been used as reference.

6.10.2 Determining the Residual Noise Level

To compute ultimately the detection limit, one needs an estimate of the residual noise level versus position on the SDI frame. Hence, for each pixel the standard-deviation over a box of $4\ px \times 4\ px$ has been computed, resulting in a 2d pattern which is - in a further step - radially averaged to determine the mean amplitude of the residual noise $I_n(r)$ in radial direction. The 1σ detection limit Δm depending on the peak intensity of the star can then be deduced as:

$$\Delta m = -2.5 \log \left(\frac{I_n(r)}{I_p} \right) \tag{6.20}$$

I_p is the deduced peak intensity and $I_n(r)$ the averaged noise amplitude.

6.10.3 Detection Limits for Epsilon Eridani

Figures 6.14 and 6.15 visualize the final detection limits for Epsilon Eridani by applying single SDI and double SDI. According to Figure 6.14 already the single SDI results in a clear improvement relative to an optimized standard reduction using unsharp-masking. Within the seeing halo of the PSF (< 1"), speckle noise can be reduced by up to 2 magnitudes. According to Figure 6.15 the detection limit improves by an additional magnitude with the double subtraction SDI technique. In both cases, the advantage of the SDI disappears for angular distances greater than the seeing halo, since the speckle noise as dominating error source is replaced by photon noise. Depending on the chosen averaging technique, the detection

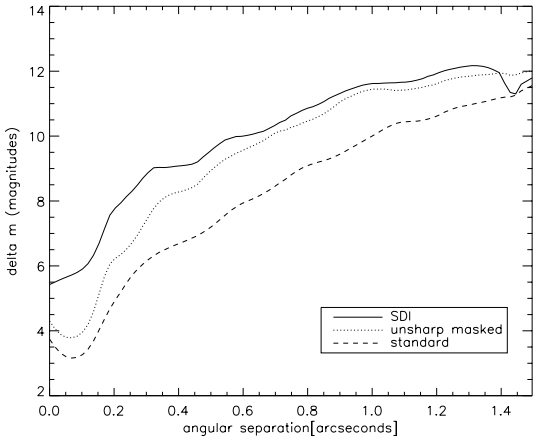

Figure 6.14: Resulting 3σ detection limit for Eps Eri applying single SDI. In comparison to optimized standard reduction techniques such as unsharp masking, speckle noise can be reduced up to 2 magnitudes within the seeing halo of the PSF.

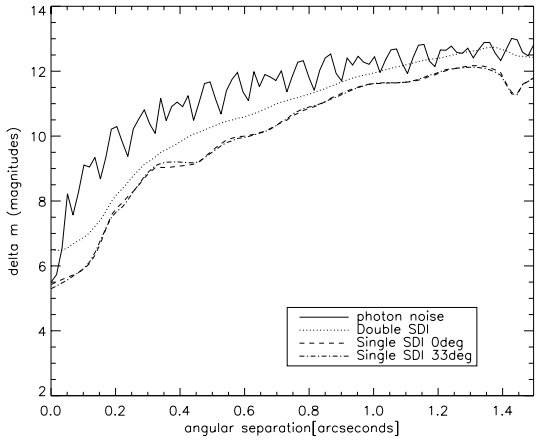

Figure 6.15: Resulting 3σ detection limit for Eps Eri applying double SDI. Double SDI leads, in comparison to single SDI, to a further boost of up to 1 magnitude in terms of detection limit. Additionally inserted is a curve indication the photon noise regime as the ultimate upper limit.

limit can - as expected - vary. Hence, although an averaging of the data set by calculating the median removes hot pixel and simplifies the identification of companion candidates on the resulting images, the detection limits may drop by up to 0.5 *mag*. As a result objects marginally detectable within the averaged frame, fall below the detection limit in the median combined frame (see Figure 6.16).

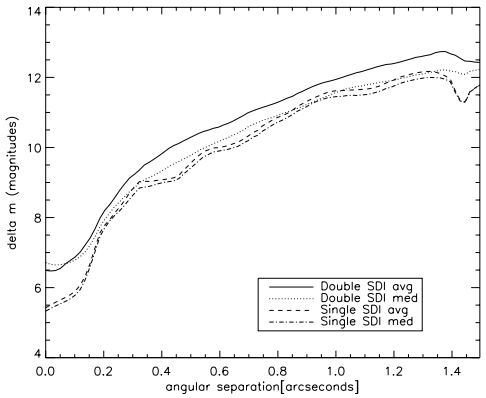

Figure 6.16: Resulting 3σ detection limits using median and average filtering techniques. Although median averaging is able to remove more effectively the impact of hot or bad pixel, it results also in a slight decrease of the achievable detection limit.

6.11 How would planets look like

To check the validity of the obtained detection limits and moreover the reliability of the data reduction pipeline, artificial companions are introduce in the raw data-sets. Then their detectability is verified in the pipeline reduced frames. For this purpose a standard pre-reduced (flat-fielded, sky-subtracted) stack of frames for each filter has been used. Since the methane atmosphere of the companion is much brighter in the 1.575 micron band, artificial companions were only inserted in this stack. The relative shift between each PSF within this data stack has been eliminated by applying the described shift algorithm. This method guarantees an accurate positioning of the "fake" companion at a fixed distance within all frames of a stack and guarantees so a proper adding of the flux. Both, the modified and non modified data sets were then passed into the pipeline and the resulting SDI images were investigated for the companions. Figures 6.17 and 6.18 depict two different simulations for a set of companions at different brightness levels. First, according to the obtained detection limit at a distance of 0.5 arcseconds for averaged double subtracted SDI, a set of three artificial planets was created, with a peak intensity of 5 σ at the residual noise level. The "companions" have been placed at distances of 0.5", 0.75" and 1", respectively. In the second case two sets of artificial companions at a significance of 5 σ according to the averaged double subtracted SDI detection limit at 1" were inserted at a distance of 1" and 1.25". For all these cases, the corresponding planetary mass of the artificial companions can be estimated following the evolutionary models of Baraffe et al. (2003). Theses simulations predict several physical parameters like mass, T_{eff}, radius, gravity and absolute brightness magnitude for different wavelength bands. Dust opacity is neglected in the radiative transfer equation, which is appropriate for objects with effective temperature $T_{eff} < 1300K$ like methane dwarfs or extra-solar giant planets at larger orbital separation. Starting from the computed detection limit one is able to estimate the expected absolute brightness of the introduced "fake" companion. By determining first the absolute H magnitude of the host star

$$m_H - M_H = 5\log(d[pc]/10) \tag{6.21}$$

which translates in the case of Eps Eri, whose H-Band magnitude is (according to the 2MASS catalog) given by $m_H = 1.88mag$, to $M_H = 4.34mag$. Adding now to the absolute brightness of Eps Eri the brightness difference in magnitudes of the introduced companion, one obtains the absolute brightness of the companion with respect to the $1.575\mu m$ filter. To estimate

the corresponding absolute H-band magnitude, the flux of the methane feature emitted by the planet has to be re-distributed over the complete H-band. The ratio of H-band width ($\sim 300nm$) and of the methane absorption-band width ($\sim 200nm$, see Figure 6.3) yields a drop in absolute H-band magnitude of roughly 1mag. Table 6.6 lists the deduced mass-ranges for the introduced "fake" companions. Due to the uncertainty in the age estimate of Eps Eri, the values vary up to a factor 2.3.

	Δ mag ($\lambda = 1.575\mu m$)	M_H	mass for 0.1 Gyr	mass for 0.5 Gyr
5 σ at 0.5"	9.7mag	15.1	$9M_J$	$21M_J$
5 σ at 1"	11.6mag	17.0	$5M_J$	$12M_J$

Table 6.6: Limiting masses of artificially inserted companions in Eps Eri datasets, detectable with a significance of 5 σ. Their masses have been deduced based on evolutionary models by Baraffe et al. (2003). Note that M_H has been corrected for the fact that methane objects are about 1mag fainter in broad H-band compared to their brightness at $\lambda = 1.575\mu m$.

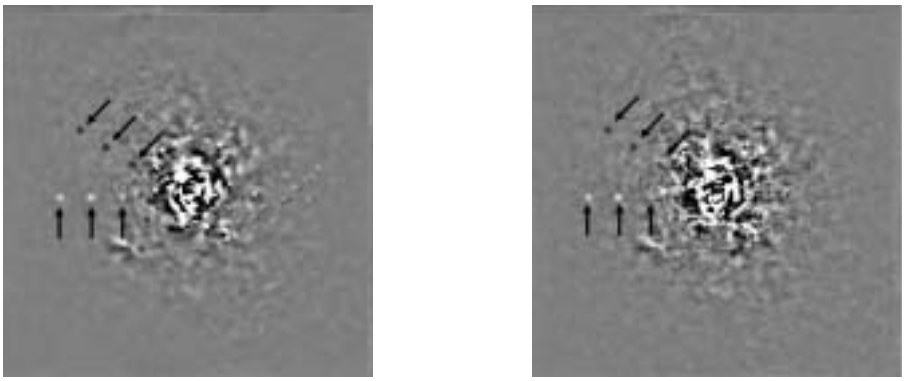

Figure 6.17: Reduced double SDI data with artificially inserted companions. While the left image depicts the averaged case, the right image shows a medianed image. The planets (characterized by a brightness level according to a 5 σ detectability at 0.5") were inserted at a distance of 0.5", 0.75" and 1" (indicated by arrows). The signal in the double SDI is seen twice. Assuming evolutionary models of Baraffe et al. (2003), the estimated mass of the planets is - depending on the age of Eps Eri - between $9M_J$ and $21M_J$. In accordance to to the deduced detection limits, in the medianed frame the inner planet is hardly detectable. The FoV for both images is 2.8 " $\times$ 2.8"

Following Figure 6.17 and Figure 6.18, all introduced companions can be identified in the averaged double subtracted SDI frame (in both cases the left image) showing the expected behavior of a positive and a negative intensity peak separated by 33°. According to the subtraction and rotation direction, the peaks have to change from positive to negative sign in clockwise direction. It is pointed out that the power of this technique is not purely in terms of improved detection limited, but also due to the much easier visual verification. This, however, depends also on the relative position of the companion, since the residual speckle noise can strongly vary within a defined radial distance. Hence, if the companion is close to a strong speckle the identification may become tricky as it is seen in Figure 6.17, where the innermost planet hardly can be visualized. Moreover the loss of detection performance, using the median method for averaging the frames, is validated, as a companion at 0.5" cannot be identified any more in Figure 6.17 (right) and in Figure 6.18 (right).

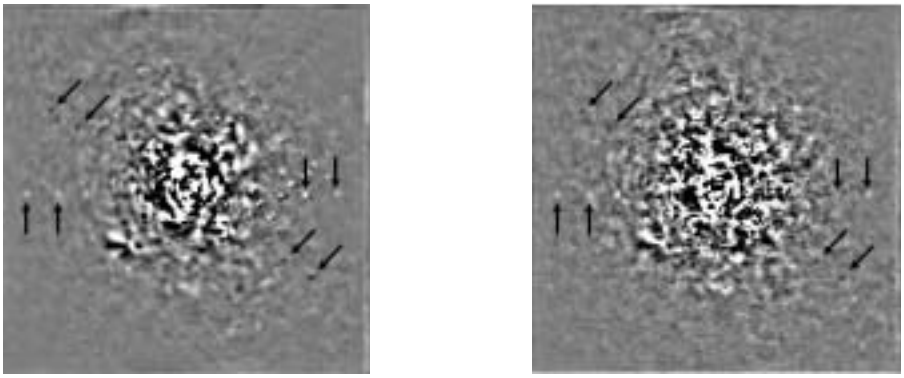

Figure 6.18: Reduced double SDI data with 2 sets of artificial planets (indicated by arrows) characterized by a brightness-level according to a 5 σ detectibility at 1", were inserted at a distance of 1" and 1.25". Assuming evolutionary models of Baraffe et al. (2003), the estimated mass of the planets is between 5 M_J and 12 M_J.

6.12 Companions around EpsEri? Limitations of SDI

Although SDI increases the possible detection limit within the seeing halo by up to several magnitudes, it suffers nevertheless from limitations. These are discussed in this section by evaluating the final results of the obtained SDI data from Eps Eri. Although this data set comprises the deepest high contrast images ever taken for this target, the $\sim 2M_J$ companion, which has been found via indirect methods, is expected to have a peak intensity a factor 5 below the deduced 5σ detection limits. It should be noted that this factor is quite uncertain, since theoretical models have not been calibrated against observations for these low masses and young ages. Recently, e.g., the absolute mass of a companion around AB Dor (age $\sim 40Myr$) has been measured, showing that evolutionary models may underestimate companion masses for objects in the range $40-90M_J$ (Close et al. (2005)). On the other hand, the planet around Eps Eri might be subject to an additional heating by frequent (one per day) cometary impact events (similar to the Shoemaker-Levy impact on Jupiter in 1994, Grady et al. (2005)). The actual mass of a still detectable planetary companion could then be even lower.

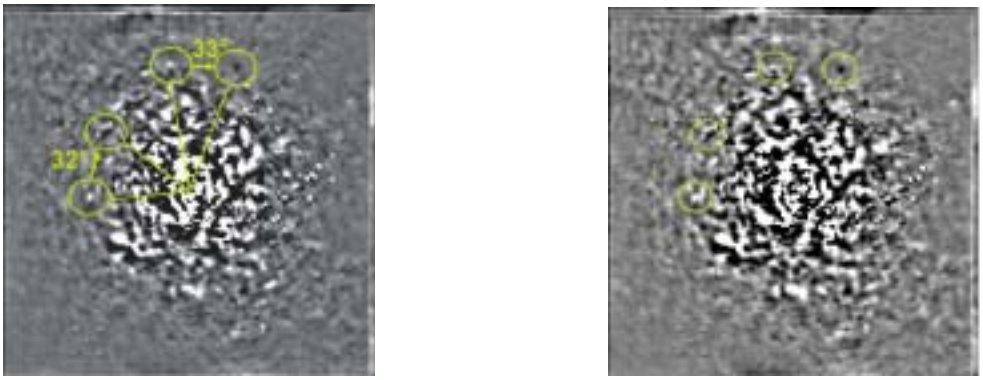

Figure 6.19: Double subtracted SDI data sets after reducing all data sets (left) and reducing the best 66% .

The averaged double subtracted SDI frame depicted in Figure 6.19 (left) contains two interesting candidates, which have been further investigated. Both are marked with circles and arrows (indicating the rotational direction of the instrument). Both candidates satisfy

basic requirements suc as:

- They are bright at 1.575 μm and fainter at longer wavelengths
- They show a correct rotational pattern and angular separation according to the instrumental rotation, since positive and negative peaks follow a clockwise rotational scheme and are separated by 32° and 33°.
- All peaks are significant at the 4 to 4.7 sigma level.

Several additional test were carried out like reducing only the 66% best data in terms of Strehl-ratio in order to verify if the signal is still detectable (see Figure 6.19 (right). A summary of the measured parameters and deduced masses are can be found in Table 6.7: The obtained intensity translates for both cases into a H-band magnitude of 17.0 mag and

candidate	separation in "/A.U.	DA[◦]	$\Delta m/\ M_H$	mass range
A	1.05"/3.4 A.U.	33	11.8 mag/17.1mag	$5M_J - 12M_J$
B	0.84"/2.8 A.U.	32	11.7mag/17.0 mag	$5M_J - 12M_J$

Table 6.7: Deduced orbital parameters and mass of both candidates. Orbital parameters of candidate A would match the indirectly detected companion by Hatzes et al. (2000)

17.1 mag, respectively, which may, according to evolutionary models by Baraffe et al. (2003), recalculated into absolute a mass ranging from 5 M_J to 12 M_J. For candidate A the projected separation is in relatively good agreement with the orbital parameters as deduced from the astrometry of Eps Eri (see section 6.7). Although the deduced planetary mass still seems to be too high, the additional flux could be, as already mentioned, be explained by frequent cometary impacts.

Although its brightness and hence the encountered companions in the double SDI image fulfill several consistency checks, further investigations of the Single SDI data sets show that the authenticity of both candidates is still somewhat uncertain. By investigating the speckle pattern around all 4 peak positions in the single SDI data sets, no clear signals arising from the candidates are visible. According to the chosen rotational direction of the instrument, one expects that a peak has to be visible in the single SDI 0° frame, which may be associated with a 33° rotated counterpart in the 33° single SDI frame. The images depicted in Figure 6.20 show both single SDI frames contrast enhanced by selecting cut levels of ±10 counts. Only a rectangular box of 60 $px \times 180\ px$ around the candidate is shown. A clear detectibility of, according to the upper assumption, all peaks cannot be confirmed when comparing the two left single SDI frames. While the 33° image shows the expected peak, the in the double SDI resulting 0° peak seems to be a composite of not perfectly cancelled out speckles within the single SDI frames. This might arise from not corrected high order effects, which slightly changes the λ/D-scale at two different wavelength band images. Hence, the double subtraction may sometimes, instead of attenuating the speckle pattern, lead to an amplification. Candidate B could to have the same origin. Moreover it looks like, another effect also plays a role, which should be subject of a further investigation. According to Fusco et al. (2002), a rotation of the instrument leads to a shift of the SHS-lenslet with respect to the DM. This causes a different response function of the DM, resulting in a slight change of the speckle pattern and loss in Strehl-ratio. This might explain the slightly shifted speckle visible in both 0° and 33° images. A quantification of all such high error sources is quite tricky, since the entire system works close to the photon noise limit and is so subject to high order aberrations, whose origin is not well understood. Hence, an ultimate confirmation

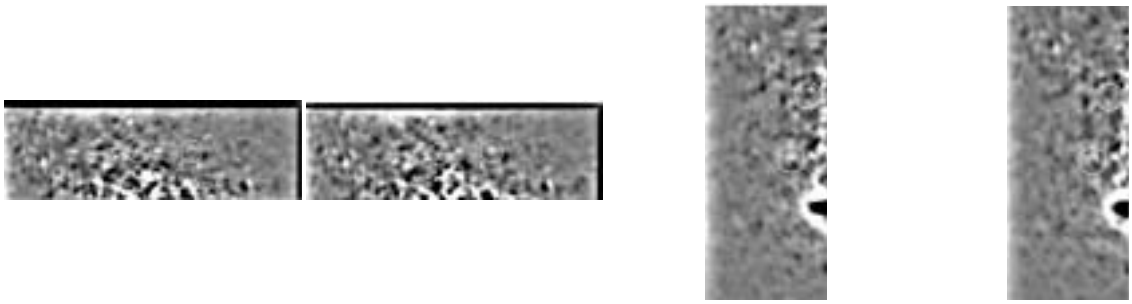

Figure 6.20: Rectangular cutout of Single SDI data sets. From left to right candidate A 0° and 33° and candidate B 0°, 33° images are shown. All images show a cut of ±10 counts in order to enhance the signal at the level of planetary companions.

whether either of the signals results from an orbiting companion or still comes from residual speckle noise, can only be obtained by second epoch data. This is anyway the only way - assuming either of the peaks is a real signal - to verify a co-moving companion. Else the signal might be from a background object showing similar spectral properties as a cool brown dwarf or giant exo-planet. Observing Eps Eri within a second epoch is a proper tool, since Eps Eri exhibits a high proper motion of roughly 1" per year, as measured by HIPPARCOS. Moreover a second epoch with longer integration time can increase the signal to noise ratio.

6.13 Conclusion

AO-aided direct imaging offers an immense potential to detect the faint signal of an orbiting planetary companion around its host star. This technique, however, still performs below the photon noise limit close to the center of the host star (< 1"), since residual halo speckles are by far the dominant noise source. This leads to a loss of achievable contrast and hence non optimal detection limit. Via optimized subtraction techniques like Simultaneous Differential Imaging, such disturbing speckles can be reduced. The SDI method, operating at a wavelength of $\sim 1.6\mu m$, is optimized for detecting cool brown dwarfs and giant exo-planets, which both exhibit methane features in their atmospheres. High contrast is achieved by subtracting two frames of adjacent wavelength located at the edge of the methane absorption band.

As a part of this thesis, a data reduction pipeline to process SDI data has been developed. Its performance has been calibrated on Eps Eri, one of the most promising candidates for a direct detection of orbiting companions. It could be verified that contrast ratios in the halo region can be increased by more than 3 magnitudes compared to conventional (unsharp-mask) techniques.

The ultimate goal, which is to reach the photon noise limit, is still missed. This leaves space for further optimizations of this new technique. SDI is in the moment limited by practical constraints like:

- Candidates close to the detection limit still cannot be distinguished from residual speckle noise without doubt
- Simultaneous Differential Imaging, in order to minimize chromatic effect, needs quite narrow band filters. This implies long integration times due to the rather inefficient use of photons.
- By focussing on physical properties of methane dwarfs, a SDI-instrument is only adoptable to search for a subcategory of extra-solar planets. Hence an extended filter set

would be advantageous

Benefited by the long exposure time, the obtained SDI data for Eps Eri represents the by far deepest high contrast image ever taken for this target. Previous AO-aided NIR direct imaging surveys incorporating Eps Eri (Luhman and Jayawardhana (2003)) achieved detection limits at a distance of 0.5" and 1" from the host star of $\Delta m = 7.5$mag and $\Delta m = 11$ mag, respectively. SDI results in a further increase of Δm of 3mag at 0.5" and Δm of 1mag at 1", i.e. a companion $\sim 6 \cdot 10^4$ times fainter than EpsEri at a wavelength of 1.575 μm could have been detected at a separation of 3.4 AU. Translating now these detection limits by means of evolutionary tracks of Baraffe et al. (2003) into corresponding absolute planetary masses of 5 to 12 M_J, it becomes clear that obviously SDI is indeed able to detect giant exo-planets close to EpsEri. Although, the (by indirect methods found) companion orbiting EpsEri still could be too faint, an interesting object has been encountered in the double SDI data, which may be nevertheless associated with the star. As shown, the candidates pass several tests. One even matches the deduced relative distance. Its visibility in the data sets may be explained by frequent cometary impacts leading to additional heating of the planet resulting in an increase of its luminosity. However, a careful visual investigation of all obtained double and single SDI data sets still leaves some doubts on the authenticity of the signal. Hence second epoch data with increased integration time will be taken in order to confirm or disprove the companion candidate.

Appendix A

Acronyms

AO	Adaptive Optics
BLT	Beam Launch Telescope
CCD	Charge Coupled Device
CWFS	Curvature Wavefront Sensor
DM	Deformable Mirror
ELT	Extremely Large Telescope
ESO	European Southern Observatory
FoV	Field of View
FT	Fourier Transform
FWHM	Full Width Half Maximum
GLAO	Ground Layer Adaptive Optics
IBB	Inverse Bessel Beam
LBT	Large Binocular Telescope
LGS	Laser Guide Star
MCAO	Multi Conjugated Adaptive Optics
MFoV	Multiple Field of View
NACO	NAOS-CONICA
PSF	Point Spread Function
OTF	Optical Transfer Function
OPD	Optical path Difference
OWL	Overwhelming Large Telescope
PIGS	Pseudo Infinite Guide Star Sensor
PSD	Power Spectral Density
PTV	Peak To Valley
PWFS	Pyramid Wavefront Sensor
RLGS	Rayleigh Laser Guide Star
RMS	Root Mean Square
SDI	Simultaneous Differential Imaging
SHS	Shack-Hartmann-Sensor
S/N	Signal to Noise
SOR	Starfire Optical Range
VLT	Very Large Telescopes
WFC	Wavefront Computer
WFS	Wavefront Sensor
WHT	William Herschel Telescope

Appendix B

Zernike Polynomials

Zernike polynomials represent a series of orthogonal modes of ascending order (Hardy (1998)). Due to their orthogonality on a unit circle they are mostly expressed in polar coordinates ρ and θ as a function of azimuthal frequency and radial degree n, where $m \leq n$, and n-m is even. For statistical analysis, it is convenient to order the polynomials in a sequence j in such a way that even values of j correspond to the symmetric modes in $\cos(m\theta)$, while odd values of j correspond to the antisymmetric modes in $\sin(m\theta)$. This set of polynomials is defined as:

$$Z_{even} = \sqrt{n+1} R_n^m(r) \sqrt{2} \cos(m\theta), \qquad m \neq 0 \tag{B.1}$$

$$Z_{odd} = \sqrt{n+1} R_n^m(r) \sqrt{2} \sin(m\theta), \qquad m \neq 0 \tag{B.2}$$

$$Z = \sqrt{n+1} R_n^m(r) \qquad m = 0 \tag{B.3}$$

where

$$R_n^m(r) = \sum_{S=0}^{(n-m)/2} \frac{(-1)^S (n-S)! r^{n-2S}}{S![(n+m)/2 - S][(n-m)/2 - S]} \tag{B.4}$$

The normalization is such that each polynomial has a root mean square value of 1 over the unit disk.

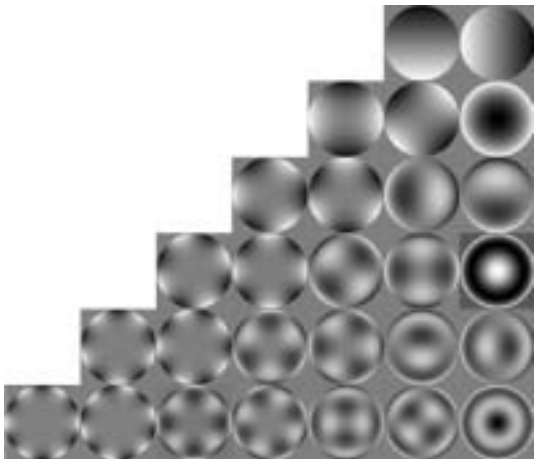

Figure B.1: Zernike polynomials from 1th to 6th radial order. From top to bottom: radial order. From right to left: Corresponding azimuthal order. The plot was kindly provided by Sebastian Egner.

Appendix C

Correlation analysis

Correlation is widely adapted in the context of image pattern matching where one is interested, if and how well certain regions within one image (auto correlation) or two different frames (cross correlation) do match. Mathematically the cross correlation of two 2-dimensional functions $f(x, y)$ and $g(x, y)$, each of size M x N, can be expressed in the discrete case by (see for instance Jaehne (2005) or Gonzales and Woods (2002):

$$c(x,y) = f(x,y) \circ h(x,y) = \frac{1}{MN} \sum_{m=0}^{M-1} \sum_{n=0}^{N-1} f^*(m,n) h(x+m, y+n) \tag{C.1}$$

where f^* denotes the complex conjugate of f, which is practically f, since one deals with real functions. Correlation has a very similar form to convolution, but differs by the sign in the summation of the second term and the complex conjugate. Equation C.1 leads to a pattern where each pixel in the spatial domain denotes the relative displacement between the considered frames. The position of the maximum intensity in this pattern denotes the relative shift for which both frames match best. Depending on the size of the compared images this approach can be very computational intense. Taking into account the correlation theorem

$$f(x,y) \circ h(x,y) \Longleftrightarrow F^*(u,v) H(u,v) \tag{C.2}$$

where correlation translates in the Fourier domain into a simple multiplication of the Fourier Transform of $f(x, y)$ and $g(x, y)$, such computations can be considerably fastened.

One disadvantage of the formalism is that the resulting intensity value gives no absolute measure of the similarity between two frames, since the result is still amplitude sensitive. For instance doubling the values of $f(x, y)$ leads to a doubling of $c(x, y)$. Therefore correlation is often given in a normalized metric according to:

$$c_n(x,y) = \frac{\sum_{m=0}^{M-1} \sum_{n=0}^{N-1} [f(m,n) - \bar{f}(m,n)][h(x+m, y+n) - \bar{h}]}{\left\{ \sum_{m=0}^{M-1} \sum_{n=0}^{N-1} [f(m,n) - \bar{f}(m,n)]^2 \sum_{m=0}^{M-1} \sum_{n=0}^{N-1} [h(x+m, y+n) - \bar{h}]^2 \right\}^{1/2}} \tag{C.3}$$

While for perfect correlation $c_n(x, y)$ is 1, for perfect anti-correlation $c_n(x, y)$ is -1. Is the data completely de-correlated, $c_n(x, y) \to 0$.

Bibliography

Alonso R., Brown T., Torres G., Latham D., Sozzetti A., Mandushev G., Belmonte J., Charbonneau D., Deeg H., Dunham E., O'Dononvan F., Stefanik R. (2004), ApJ, Vol. 613, p. 153

Ammler A., Fuhrmann K., Guenther E., König B., Neuhaeuser R. (2003), Astronomische Nachrichten, Vol. 324, p. 38

Andersen T., Ardeberg A., Beckers J. M., Flicker, R., Jessen, N. C., Gontcharov A., Mannery E., Owner-Petersen M., Riewaldt H. (2000), Proc. *Workshop on Extremely Large Telescopes*, Backaskog Castle, Sweden, p. 72

Angel J.R.P. (1994), Nature, Vol. 368, p. 203

Angel J.R.P. (1995), ApJS, Vol. 223, p. 136

Aumann H.H (1988), ApJ, Vol. 96, p. 1415

Babcock H.W. (1953), PASP, Vol. 65, p. 229

Bahcall J.N., Soneira R.M. (1980), ApJS, Vol. 44, p. 73

Baraffe I., Chabrier G., Barman T.S., Allard F., Hauschildt P.H. (2003), A.&A., Vol. 402, p. 701

Bähr J., Brenner K.H., Sinzinger S. (1994), Appl. Opt., Vol. 33, p. 5919

Beckers J.M. (1988), Proc. *Very Large Telescopes and their Instrumentation*, ESO, Garching bei Muenchen, p. 693

Beckers J.M., Owner-Petersen M., Andersen T. (2004), Proc. *2nd Workshop on Extremely Large Telescopes*, Backaskog Castle, Sweden, p. 123

Benedict G. F., McArthur B. E., Forveille T., Delfosse X., Nelan E., Butler R. P., Spiesman W., Marcy, G., Goldman B., Perrier, C., Jefferys W. H., Mayor M. (2002), ApJ, Vol. 581, p. 115

Black D.C., Han I., Gatewood G. (2000), DPS, Vol. 32, p. 3106

Black D. (1980), Icarus, Vol. 43, p. 293

Bond I.A., Udalski A., Jaroszynski M., Rattenbury N.J., Paczynski B., Soszynski I., Wyrzykowski L., Szymanski M.K., Kubiak M., Szewczyk, O. and 22 coauthors (2004), ApJ, Vol. 606, p.155

Bouchez A.H., Le Mignant D., van Dam M.A., Chin J., Hartman S., Johansson E., Lafon R., Stomski P., Summers D., Wizinowich P.L. (2004), SPIE, Vol. 5490, p.321

Brandner W., Sheppard S., Zinnecker H., Close L., Iwamuro F., Krabbe A., Maihara T., Motohara K., Padgett D. L., Tokunaga A. (2000), A.&A., Vol. 364, p.13

Brunetto E.,Dierickx P., Gilmozzi R., Le Louarn M., Koch F., Noethe L., Verinaud Ch., Yaitskova N. (2003), Proc. *2nd Workshop on Extremely Large Telescopes*, Backaskog Castle, Sweden, p. 159

Butler D. J., Davies R. I., Redfern R. M., Ageorges N., Fews H. (2003), A.&A., Vol. 403, p. 775

Butler D., Hippler S., Davies R.I. (2002), Proc. *Beyond Conventional Adaptive Optics bcao.conf*, Venice, Italy, p. 349

Burrows A., Liebert J. (1993), RvMP, Vol.65, p. 301

Charbonneau D., Allen L.E., Megeath S.T., Torres G., Alonso R., Brown T.M.; Gilliland R.L., Latham D.W., Mandushev G., O'Donovan F.T., Sozzetti A. (2005), ApJ, Vol. 626, p. 523

Charbonneau D., Brown T.M., Noyes R.W., Gilliland R.L. (2002), ApJ, Vol. 568, p.377

Charbonneau D.,Brown T.M., Latham D.W., Mayor M. (2000) ApJ, Vol. 529, p. 45

Chauvin G., Lagrange A.-M., Dumas C., Zuckerman B., Mouillet D., Song I., Beuzit J.-L., Lowrance, P. (2004) A.&A., Vol. 425L, p.29

Chelli A. (2005), A.&A., not submitted yet

Close L.M., Lenzen R., Guirado J.C., Nielsen E.L., Mamajek E.E., Brandner W., Hartung M., Lidman C., Biller B. (2005), Nature, Vol. 433, p. 286

Conan J.-M., Rousset G., Madec P.-Y. (1995), JOSA, A 12, p. 1559

Conan, R., Ziad A., Borgnino J., Martin F., Tokovinin A. A. (2000), SPIE, Vol. 4006, p. 963C

Costa J. (2005), *Development of a new Infrared Pyramid Wavefront Sensor*, PhD thesis, University of Heidelberg

Deming D., Seager S., Richardson L. J., Harrington J. (2005), Nature, Vol. 434, p. 740

Dessenne C., Madec P., Rousset G. (1998), Applied Optics IP, Vol. 43, Issue 29, p.5458

Dierickx P., Brunetto E., Comeron F., Gilmozzi R., Gonte F., Koch F., Le Louarn M., Monnet G., Spyromilio J., Surdej I., Verinaud C., Yaitskova N. (2004), SPIE, Vol. 5489, p. 391

Durnin J. (1987), JOSA, Vol. 4, p. 651

Durnin J., Miceli J.J.Jr., Eberly J.H. (1987); Ph. Rev. L., Vol. 58, p. 1499

Ellerbroek B. L., van Loan C., Pitsianis N.P., Plemmons R.J. (1994), SPIE, Vol. 2201, p. 935

Egner S. (2003), *Optical Turbulence Estimation and Emulation*, Diploma thesis, University of Heidelberg

Espoisto S., Riccardi A., (2001), A.& A., Vol. 369, p. 9

Farinato J., Ragazzoni R. (2005), A.&A., in submission

Fegley B.Jr., Lodders K. (1996), ApJ, Vol. 472, p. 37

Feautrier P., Kern P.Y., Dorn R.J., Rousset G., Rabou P., Laurent S., Lizon J.L., Stadler E., Magnard Y., Rondeaux O., Cochard M., Rabaud D., Delboulbe A., Puget P., Hubin N. (2000), SPIE, Vol. 4007, p.396F

Flicker R.C., Rigaut F., Ellerbroek B.L. (2003), A.&A., Vol. 400, p. 1199

Foy R., Labeyrie A. (1985), A.& A., Vol. 152, p. 29

Foy R. Migus A., Biraben F., Grynberg G., McCullough P. R., Tallon M. (1995), A.&AS., Vol. 111, p. 569

Fried D., Belsher J.F. (1994), JOSA, Vol. 11, p. 277

Feldt M., Turatto M., Schmidt H.M., Waters R., Neuhaueser R., Amorim A. (2003), Proc. *Towards other earths: DARWIN/TPF and the Search for Extrasolar Terrestrial Planets*, MPIA, Heidelberg p. 99

Toraldo di Francia G. (1952), Nuovo Cimento, Vol. 9, p. 426

Fried D. (1965), JOSA, Vol. 55, p. 1427

Frink S., Mitchell D.S., Quirrenbach A., Fischer D.A., Marcy G.W., Butler R. (2003), Astronomische Nachrichten, Vol. 324, p.6

Fugate R. Q., Wopat L. M., Fried, D. L., Ameer G. A., Browne S. L., Roberts P. H., Tyler G. A., Boeke B. R., Ruane, R. E. (1991), Nature, Vol. 353, p. 144

Fugate R.Q. (1994), JOSA, Vol.11, p. 310F

Gaessler W., Ragazzoni R., Herbst T. M., Andersen D. R., Arcidiacono C., and 24 co-authors (2004), SPIE, Vol. 5490, p. 527

Gilmozzi R., Delabre B., Dierickx P., Hubin N. N., Koch F., Monnet G.; Quattri M., Rigaut F. J., Wilson R. N. (1998), SPIE, Vol. 3352, p. 778G

Grady C.A., Sitko M.L., Bjorkman K, S., Perez M,R., Lynch D.K., Russell R.W., Hanner M.S. (1997), ApJ, Vol. 483, p. 449

Greaves J.S., Holland W.S., Moriarty-Schieven G., Jenness T., Dent W.R.F., Zuckerman B., McCarthy C., Webb R.A., Butner H.M., Gear W.K., Walker H.J (1998), ApJ, Vol. 506, p. 133

Greenwood D.P (1977), JOSA, Vol. 67, p. 390

Gonzales R.C., Woods W.E. (2002), *Digital Image Processing*, Pearson Education International

Hartmann J. (1900), Zeitschr. f. Instr., Vol. 24, p.1

Happer W., MacDonald G.J., Max C.E., Dyson F.J., (1994), JOSA, Vol.11, p. 263

Hawarden, T. G., Gilmozzi R, Hainaut O. (2003), ASPC, Vol. 294, p.581H

Hatzes A.P., Cochran W.D., McArthur B., Baliunas S.L., Walker G.A.H., Campbell B., Irwin A.W., Yang S., Kürster M., Endl M., Els S., Butler R., Marcy G.W (2000), ApJ, Vol. 544, p. 145

Hecht E. (1998), *Optics*, Addison Wesley Longman

Henry T.J., McCarthy D.W.Jr. (1990), A.&A., Vol. 350, p. 334

Hermann R.M,Wiggins T.A., (1991), JOSA, Vol. 8, p. 932

Hubin, N., Le Louarn, M., Conzelmann R., Delabre B., Fedrigo E., Stuik R. (2004), SPIE, Vol. 5490, p. 846H

Jaehne B. 2005, *Digitale Bidverarbeitung*, Springer Verlag, Berlin

Johnston D.C., Welsh B.M (1994), JOSA, Vol A11, p. 394

Noll R. (1976), JOSA, Vol. 66, p. 207

Kaper M. (2000), *Optimization of an adaptive optics system and its application to high-resolution imaging spectroscopy of T Tauri*, PhD thesis, University of Heidelberg

Labeyrie F. (1970), A.& A., Vol. 6, p.85

Langlois M., Sandler D., Ryan P., McCarthy D. (1998), SPIE, Vol. 3353, p. 189

Laurent S., Deron R., Rousset G., Molodij G. (1995), Proc. ESA/ESO conf: *Topical meeting on Adaptive Optics*, ESO, Garching bei Muenchen

Le Louarn, M.; Hubin, N.; Sarazin, M.; Tokovinin, A., (2000), MNRAS, Vol. 317, p. 535L

Leinert, C.; Haas, M.; Weitzel, N. (1993), A.& A., Vol. 271, p.535

Lenzen R., Close L., Brandner W., Biller B., Hartung M. (2004), SPIE, Vol.5492, p. 970

Lloyd-Hart M., Baranec C., Milton M.N., Stalcup T., Snyder M, Putnam N., Angel J. R. P. (1994), astro-ph/0508402

Luhman K.L, Jayawardhana R. (2003), ApJ, Vol. 566, p. 1132

Hardy J.W. (1991), *Adaptive Optics for Astronomical Telescopes*, Oxford University Press

Marcy G., Butler P., Fischer D., Vogt S., Lissauer J., Rivera E. (2001), ApJ, Vol. 556, p. 296

Maréchal A. (1947), Rev. d'Opt, Vol. 26, p. 257

Marois Ch., Doyon R., Racine R., Nadeau D., (2000), PASP, Vol. 112, p. 91

Masciadri E., Feldt M., Hippler S. (2004), AJ, Vol. 613, p. 572

Mayor, M.; Queloz, D. (1995), Nature, Vol.378, p. 355

McCaughrean M.J., Close L.M., Scholz R.-D., Lenzen R., Biller B., Brandner W., Hartung M., Lodieu N. (2004), A.&A., Vol. 413, p. 1029

Morris T.J., Berry P., Butterley T., Clark P., Dunlop C. N., Myers R.M., Saunter C.D., Wilson R.W. (2004), SPIE, Vol. 5490, p. 891M

Mountain M. (1997), SPIE, Vol. 2871, p. 597

Nakajima T., Oppenheimer B.R., Kulkarni S.R., Golimowski D.A., Matthews K., Durrance S.T. (1995), Nature, Vol. 378, p. 463

Nicolle M. Fusco T., Michau V., Rousset G. Blanc A. Beuzit J.-L., (2004) SPIE, Vol. 5490, p.858

Obukhov A.M. (1949), Izv., Akad., Nauk. S.S.S.R., Ser. Geograf. Geofiz., Vol 13, p. 318

Oppenheimer B.R., Golimowski D.A., Kulkarni S.R., Matthews K., Nakajima T., Creech-Eakman M., Durrance S.T. (2001), ApJ, Vol. 121, p. 2189

Oppenheimer B.R., Kulkarni S.R., Matthews K., Nakajima T. (1995), Science, Vol. 270, p. 1478

Patience J., Ghez A. M., Reid I. N., Weinberger A. J., Matthews K. (1998), AJ, Vol. 115, Issue 5, p. 1972

Pilkington J. D. H., Thompson L., Gardner C. (1987), Nature, Vol. 330, p. 116

Pope S.B. (2000), *Turbulent Flows*, Cambridge University Press

Quattri M, Koch F., Noethe L., Correal Bonnet A., Nölting S. (2003), SPIE, Vol. 4840, p. 459

Rigaut F., Rousset G., Kern P., Fontanella J.-C., Gaffard J.-P., Merkle F., Lena P. (1991), A. & A., Vol. 250, p. 280

Rigaut F., Gendron E. (1992), A.&A., Vol. 261, p. 677R

Rigaut F. (2002), Proc. *Beyond Conventional Adaptive Optics bcao.conf*, Venice, Italy, p. 11R

Rigaut F. J., Ellerbroek B. L., Flicker R. (2000), SPIE, Vol. 4007, p. 1022

Rabien S., Davies R., Ott T., Li J., Abuter R., Kellner S., Neumann U. (2000), SPIE, Vol. 5490, p. 981

Racine R., Walker G.A.H., Nadeau D., Doyon R., Marois C. (1999), PASP, Vol. 111, p. 587

Racine R., Walker G.A.H., Nadeau D., Doyon R., Marois C. (1999), PASP, Vol. 111, p. 587

Ragazzoni R. (1996), Journal of Modern Optics, Vol. 43, p.289

Ragazzoni R., Farinato J., (1999), A.& A., Vol. 350, p. 23

Ragazzoni R. (1996), A.& A., Vol. 305, p. 13

Ragazzoni R. (1997), A.&A., Vol. 319, p. 9

Ragazzoni R., Marchetti E., Valente G. (2000), Nature A.&A., Vol. 403, p. 54

Ragazzoni R., Marchetti E., Rigaut F. (1999) A.&A., Vol. 342, p.53R

Ragazzoni R., Farinat J., Marchetti E., (2000) SPIE, Vol. 4007, p. 1076

Ragazzoni R., Diolaiti E., Farinato J., Fedrigo E., Marchetti E., Tordi M., Kirkman D., (2002), A.&A., Vol. 396, p. 731R

Ragazzoni (1999), A.&A., Vol. 136, p. 205

Ragazzoni R., Tordi M., Diolaiti E., Kirkman D. (2001), MNRAS, Vol. 327, p. 949

Rivera E., Lissauer J., Butler P., Marcy G., Vogt S., Fischer D., Brown T., Laughlin G., (2005), ApJ, in submitted

Riccardi A., Bindi N., Ragazzoni R., Esposito S., Stefanini P. (1998), SPIE, Vol. 3353, p. 941

Roddier F. (1981), Prog. Opt., Vol. 19, p. 281

Roddier F. (1999), *Adaptive Optics in Astronomy*, Cambridge University Press

Roddier F. (1988), Appl. Opt., Vol. 27, p.1223

Rosenthal E. D., Gurwell M.A., Ho P.T.P. (1996), Nature, Vol. 384, p.243

Rousset G., Fontanella J.-C., Kern P., Gigan P., Rigaut F., Lena P., Boyer C., Jagourel P., Gaffard J.-P., Merkle F. (1990), A. & A., Vol. 230, p. 29

Saar S.H., Osten R.A. (1997), MNRAS, Vol. 284, p. 803

Schroeder D.J., Golimowski D.A., Brukardt R.A., Burrows C.J., Caldwell J.J., Fastie W.G., Ford H.C., Hesman B., Kletskin I., Krist J.E., Royle P., Zubrowski R.A. (2000), ApJ, Vol. 119, p. 906

Sivaramakrishnan A., Koresko C.D., Makidon R.B., Berkefeld T., Kuchner M.J. (2001), ApJ, Vol. 552, p. 397

Soderblom D.R., Dappen W. (1989), ApJ, Vol. 342, p. 945

Strehl K. (1902), Zeitschr. Instrum., Vol. 22, p. 214

Tallon M., Foy R., (1990), A.&A., Vol.235, p. 549

Thom A. (1951), *The solar observations of megalithic man*, Journal of the British Astronomical Association

Thompson L.A., Gardner C.S. (1987), Nature, Vol. 328, p. 229

Thompson L.A., Wilks S. C., Brase J. M., Young R.A., Johnson, G.W.; Ruggiero A.J. (2002), SPIE, Vol. 4494, p. 89

Thompson L.A., Teare S.W. (2002), PASP, Vol.114, p. 1029

Tokovinin A. (2004), PASP, Vol. 116 p. 941T

Tubbs R. N. (2003), *Lucky Exposures: Diffraction limited astronomical imagig through the atmosphere*, PhD-thesis, Cambridge University

van Dam, M. A., Le Mignant, D., Macintosh, B. A. (2004), Applied Optics IP, Vol. 43, Issue 29, p.5458

Veran J.P., Rigaut F., Maitre H., Rouan D. (1997), JOSA, Vol. A14, p. 3057

Vernet E., Ragazzoni R., Diolaiti E., Farinato J., Baruffolo A., Arcidiacono C., Crimi G., Ghigo M., Tomelleri R., Rossenettini F.,(2002), ESO-Doc. No.: OWL-TRE-INA-60000-0054

Vernin J., Caccia J.-L., Weigelt G., Mueller M. (1991), A.&A., Vol. 243, p. 553

Viard E., Delplancke F., Hubin N., Ageorges N., Davis R. (2001), Exp.Astr. Vol. 10, p. 123

von der Luehe O. (2001), *Interferometrie in der Astronomie*, Albert-Ludwig Universitaet Freiburg im Breisgau

Wambsganss J. (2004), ASPC, Vol. 321, p. 47

Wang J.Y., Markey J.K. (1978), JOSA, Vol. 68, p. 78

Weigelt G. (1991), Progress in Optics Vol. 29, Wolf E. (ed), North Holland Amsterdam, p. 293

Weigelt G., Balega Y, Bloecker T, Fleischer A. J., Osterbart R., Winters J. M. (1998), A.& A., Vol. 333, p.L51

Welsh B.M., Gardner C.S. (1991), JOSA, Vol A8, p. 69

Wielen, R.; Dettbarn, C.; Jahreiß, H.; Lenhardt, H.; Schwan, H. (1999), A.&A., Vol. 346, p. 675

Wolszczan A., Frail D.A. (1992), Nature, Vol. 355, p. 145

Yaitskova N., Doehlen K., Dierickx P., (2002), SPIE, Vol. 4840, p. 171

D A N K E . . .

Am Schluss möchte ich mich noch bei allen bedanken, die zum Gelingen dieser Arbeit beigetragen haben. Insbesondere hervorheben möchte ich:

Prof. Roberto Ragazzoni, der mir die Möglichkeit zu dieser Dissertation gegeben hat. Sein reichhaltiger Erfahrungsschatz und Ideenreichtum waren die Basis für das Sensorkonzept sowie Garant für die positiven Resultate im Labor und am Teleskop. Durch seine unvergleichliche Art erzeugte er ein einmaliges Ambiente, das die ersten 1 1/2 Jahre zu einem echten Erlebnis machten und mir unvergessen bleiben werden. Darüberhinaus danke ich ihm für die Möglichkeit, meine Arbeiten an vielen internationalen Konferenzen präsentieren zu dürfen.

Wolfgang Brandner, dem ich ganz grossen Dank für die beispielhafte Betreuung des astronomischen Teils der Arbeit schulde. Insbesondere für die Vielzahl interessanter Diskussionen, die Bereitschaft, sein immenses astronomisches Wissen weiterzugeben und seine Geduld das ein oder andere auch zweimal zu erklären. Danke für die Unterstützung in den letzten Tagen vor Abgabe der Arbeit und das wiederholte Korrekturlesen. Unvergessen bleiben mir auch die vielen schönen Koch-, Schach- und Spieleabende.

Wolfgang Gässler und die ausgezeichnete Zusammenarbeit mit ihm in den letzten drei Jahren. Dabei denke ich nicht nur an die große Zahl der fruchtbaren wissenschaftlichen Diskussionen, die uns beide im Verständnis von PIGS vorangebracht haben, sondern vor allem an sein offenes Ohr für alle meine kleinen und grossen Sorgen.

Die Alexander von Humbold Stiftung durch die, im Rahmen des Paulspreis, diese Studie erst möglich wurde.

Prof. Dr. Reinhard Mundt und Prof. Dr. Immo Appenzeller und ihre Bereitschaft als Gutachter der Dissertation zu fungieren.

Emiliano Diolaiti für die hilf- und lehrreichen Diskussionen über (Adaptive) Optik, Digitale Bildverarbeitung und IDL, die mich im Verständnis für AO und PIGS weit vorangebracht haben.

Sebsatian Egner für die grosse Zahl ausgiebiger Diskussionen über AO, MCAO, GLAO, Turbulenz und ELTs und noch über viele weitere Themen..... :).

Elena Mascriadri für ihre Unterstützung bei der Entwicklung der Datenreduktionspipeline und die vielen netten Abende im "Vater Rhein".

Jacopo Farinato sowie Carmelo Arcidiacono für die Unterstützung bei IDL- und Alignmentfragen während des Labor- und Teleskopexperiments. Vor allem aber denke ich gerne zurück an die vielen spassigen Momente in den letzten 3 Jahren, wo ich gelernt habe, dass sich der bayerische und italenische Humor sehr sehr ähnlich sind.

Tim Morris, Richard Myers, Chris Saunter und das restliche ING Team für die wunderbare Zeit am WHT sowie deren Engagement, die zum Erfolg des Teleskopexperiments entscheidend mitbeigetragen haben.

Die Kollegen in der Feinmechanik- und Elektronikwerkstatt und die hervorragende Kooperation. Besonderer Dank gilt vor allem Herrn Böhm und "Sam" Wagner für deren immense Hilfsbereitschaft.

Meine bayerischen Zimmergenossen Sebastian und Sigi, die für das gewisse "Etwas" in der bajuwarischen Exklave Zimmer 114 gesorgt haben, sowie an Fulvio, Micaela und Eva.

Andrea Stolte und ihre Unterstützung in den Tagen vor der Abgabe. Danke für das Korrekturlesen der Arbeit und die grosse Anzahl der hilfreichen Tipps und Kommentare.

Beth Biller und unseren regen Austausch bezüglich der SDI-pipeline.

Die Kaffeerunde für unvergessliche Augenblicke.....

Meine Mutter und meinen Bruder Florian, die mich während der vergangenen Jahre mit allen Möglichkeiten unterstützt haben und sicherlich einen Grossteil zum Gelingen dieser Arbeit beigetragen haben.

Meine Familie hier insbesondere meine Grossmutter sowie Onkel Franz, Onkel Luscho, Tante Heidi, Onkel Hans, Onkel Karl-Heinz.

Und ganz am Schluss meine Freunde Christine, Klaus, Lothar und Maria, die zu Hause für die nötige Abwechslung gesorgt haben :).